Accurate structural health monitoring in composites

With fibre Bragg grating sensors

Rajabzadeh, Aydin

DOI
10.4233/uuid:3c85713e-7158-4d67-b93b-54f02e213c12

Publication date
2020

Document Version
Final published version

Citation (APA)
Rajabzadeh, A. (2020). *Accurate structural health monitoring in composites: With fibre Bragg grating sensors*. [Dissertation (TU Delft), Delft University of Technology]. https://doi.org/10.4233/uuid:3c85713e-7158-4d67-b93b-54f02e213c12

ACCURATE STRUCTURAL HEALTH MONITORING IN COMPOSITES

WITH FIBRE BRAGG GRATING SENSORS

ACCURATE STRUCTURAL HEALTH MONITORING IN COMPOSITES

WITH FIBRE BRAGG GRATING SENSORS

Proefschrift

ter verkrijging van de graad van doctor
aan de Technische Universiteit Delft,
op gezag van de Rector Magnificus, prof. dr. ir. T.H.J.J. van der Hagen,
voorzitter van het College voor Promoties,
in het openbaar te verdedigen op dinsdag 20 Oktober 2020 om 10:00 uur

door

Aydin RAJABZADEH

Master of Science in Biomedical Engineering,
University of Tehran, Tehran, Iran,
geboren te Tehran, Iran.

Dit proefschrift is goedgekeurd door de promotoren.

Samenstelling promotiecommissie bestaat uit:

Rector Magnificus,	voorzitter
Prof. dr. ir. R. Heusdens,	Technische Universiteit Delft, promotor
Dr. R. M. Groves,	Technische Universiteit Delft, promotor
Dr. ir. R. C. Hendriks,	Technische Universiteit Delft, promotor
Onafhankelijke leden:	
Prof. dr. S. James,	Cranfield University
Prof. dr. D. Iannuzzi,	Vrije Universiteit Amsterdam
Prof. dr. ir. A. J. van der Veen,	Technische Universiteit Delft
Prof. dr. C. Bisagni,	Technische Universiteit Delft

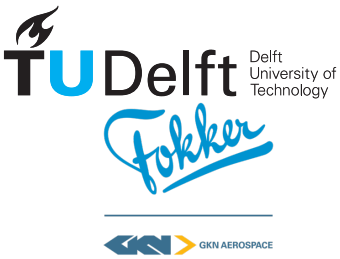

Keywords: Fiber optic sensing, fiber Bragg gratings, damage detection, aerospace composites, strain, smart structures, structural health monitoring, optimization, algorithms.

ISBN 978-94-6384-155-9

An electronic version of this dissertation is available at
http://repository.tudelft.nl/.

To my lovely wife Bahareh, and to my parents.

CONTENTS

SUMMARY

Compared to metals, composite materials offer higher stiffness, more resilience to corrosion, have lighter weights, and their mechanical properties can be tailored by their layup configuration. Despite these features, composite materials are susceptible to a diversity of damages, including matrix cracks, delamination, and fibre breakage. If these damages are not detected and mended, they can spread and result in the failure of the whole structure. In particular, when the structure is under fatigue and vibrations during flight, this process can expedite. Moreover, if such damages occur in the internal layers of the composite material, they will be difficult to detect and to characterise. There is thus a huge demand for reliable and accurate structural health monitoring methods to identify these defects. Such methods either try to monitor the structural integrity of the composite during service, or they are used for studying a desired configuration of a composite material during fatigue and tensile tests. This thesis provides structural health monitoring solutions that can potentially be used for both these categories. The structural health monitoring applications developed in this thesis range from accurate strain and displacement measurement, to detection of cracks and the identification of damages in composites.

In this thesis, fibre Bragg grating (FBG) sensors were chosen for this purpose. The miniature size and small diameter of these sensors makes them an ideal candidate for embedding them between composite layers, without severely altering the mechanical properties of the host composite material. They can thus provide us with direct information about the current state of the laminated composite, potentially at any depth. This is especially useful for acquiring information about the internal layers of the composite material, as barely visible impact damages and micro-cracks often form beneath the surface of the material without being visible on its exterior.

In spite of their interesting physical characteristics, applications of FBG sensors are typically limited to point strain or temperature sensors. Further, it is often assumed that the strain field along the sensor length is uniform. For this reason, there is currently a gap in the field of structural health monitoring in retrieving meaningful information about the non-uniform strain field to which the FBG sensor is subjected in damaged structures. The focus of this thesis is on analysing the response of FBG sensors to highly non-uniform strain fields, which are a characteristic of the existence of damage in composites.

To tackle this problem, first a new model for the analysis of FBG responses to non-uniform strain fields will be presented. Using this model, two algorithms are presented to accurately estimate the average of such non-uniform axial strain fields, which conventional strain estimation algorithms fail to deliver. In fact, it is shown that the state-of-the-art strain estimation methods using FBG sensors can lead to errors of up to a few thousand microstrains, and the presented algorithms in this thesis can compensate for such errors. It was also shown that these methods are robust against spectral noise from the interrogation system, which can pave the way for more affordable FBG based strain estimation solutions.

Another contribution of this thesis is the demonstration of two new algorithms for the

detection of matrix cracks, and for accurate monitoring of the delamination growth in composites, using conventional FBG sensors. These algorithms are in particular useful for studying the mechanical behaviour of laminated composites in laboratory setups. For instance, the matrix crack detection algorithm is capable of characterising internal transverse cracks along the FBG length during tensile tests. Along the same lines, the delamination growth monitoring algorithm can accurately localise the delamination crack tip along the FBG length in mode-I tensile and fatigue tests. These algorithms can perform in real-time, which makes them ideal for dynamic measurement of crack propagation under fatigue, and their spatial resolution and accuracy is superior to the other state-of-the-art damage detection techniques.

Finally, to enhance the precision of the damage detection schemes presented in this thesis, two different methods are proposed to accurately determine the active gauge length of the FBG sensor, and its position along the optical fibre. This information is generally not provided for commercial FBG sensors with such accuracy, which can adversely affect the precision of crack tip localisation algorithms. Following the algorithms provided in this thesis, the sensor position can be marked on the optical fibre with micrometer accuracy.

SAMENVATTING

Composietmaterialen bieden, vergeleken met metalen, een hogere stijfheid, betere weerstand tegen corrosie, zijn lichter van gewicht, en de mechanische eigenschappen kunnen worden aangepast door verschillende gelaagde configuraties. Ondanks deze eigenschappen zijn compositiematerialen vatbaar voor verschillende beschadigingen: matrix scheuren, delaminatie en vezelbreuken. Als deze beschadigingen niet worden gedetecteerd en hersteld, kunnen ze zich verspreiden en de gehele structuur beschadigen. Dit proces versnelt met name wanneer vermoeiing optreedt in de structuur en vibraties aanwezig zijn zoals tijdens een vlucht. Bovendien zijn dit soort beschadigingen in de interne lagen van compositiematerialen moeilijk te detecteren en karakteriseren. Hierdoor is er een grote vraag naar betrouwbare en nauwkeurige structural health monitoring methodes om deze defecten te identificeren. Zulke methodes proberen de structurele integriteit van het compositiemateriaal tijdens het gebruik te meten, of ze worden gebruikt in onderzoek naar gewenste configuraties van compositiematerialen tijdens een vermoeidheidstest en een trekproef. In dit proefschrift worden oplossingen beschreven die potentieel voor beide van de genoemde categorieën gebruikt kunnen worden. De toepassingen in de structural health monitoring die in dit proefschrift worden beschreven variëren van nauwkeurige rek- en verplaatsingsmetingen tot de detectie van scheuren en de identificatie van schade in composiiten.

Voor deze metingen is gekozen voor Fiber Bragg grating (FBG) sensoren. Het miniatuur formaat en kleine diameter van deze sensoren maakt ze de ideale kandidaat om ze tussen de lagen in te sluiten zonder dat de mechanische eigenschappen van het compositiemateriaal daardoor ernstig veranderingen. Hierdoor kunnen deze sensoren direct informatie bieden over de huidige conditie van de gelamineerde compositie, mogelijk op elke diepte. Dit is met name nuttig voor het verkrijgen van informatie over de interne lagen van het compositiemateriaal, aangezien nauwelijks zichtbare impact schade en microscheuren vaak onder het oppervlak van het materiaal vormen zonder dat het zichtbaar is aan de buitenkant.

Ondanks de interessante fysieke eigenschappen, worden FBG sensoren vaak slechts toegepast als puntsensoren of temperatuursensoren. Verder wordt vaak aangenomen dat de rek uniform is langs de vezel van de sensor. Om deze reden is er momenteel een gebrek aan kennis in de structural health monitoring op het gebied van bruikbare metingen van de niet-uniforme rek langs een FBG sensor. De nadruk van dit proefschrift ligt op het analyseren van de respons van FBG sensoren in sterk niet-uniforme spanningsvelden, welke typisch verantwoordelijk zijn voor schade aan composieten.

Om dit te bereiken wordt eerst een nieuw model gepresenteerd voor de FBG respons analyse in niet-uniforme spanningsvelden. Met dit model worden twee algoritmes gepresenteerd om nauwkeurig het gemiddelde van de niet-uniforme axiale spanningsvelden te schatten, die conventionele algoritmes niet kunnen leveren. Het is aangetoond dat de nieuwste rek schattingsalgoritmes die gebaseerd zijn op FBG sensoren fouten maken die op kunnen lopen tot een paar duizend microstrains. Het door dit proefschrift voorgestelde algoritme kan voor deze fouten corrigeren. Ook werd aangetoond dat deze methodes be-

stand zijn tegen spectrale ruis van het uitleessysteem, wat kan leiden tot goedkopere FBG gebaseerde schattingsmethodes.

Een andere bijdrage van dit proefschrift is de demonstratie van twee nieuwe algoritmes voor de detectie van matrix scheuren en nauwkeurige monitoring van de groeiende delaminatie in composiiten met gebruik van conventionele FBG sensoren. Deze algoritmes zijn met name bruikbaar in onderzoek naar het mechanische gedrag van gelamineerde composiiten in laboratorium opstellingen. Het matrix scheur detectiealgoritmen is bijvoorbeeld in staat om interne transversale scheuren langs een FBG sensor te karakteriseren tijdens een trekproef. Op dezelfde manier kan het monitoring algoritme voor groeiende delaminatie nauwkeurig het kraakpunt bepalen van de delaminatiescheur langs de FBG sensor tijdens een mode-I vermoeidheidstest en een trekproef. Deze algoritmes kunnen real-time uitgevoerd worden, waardoor het ideale kandidaten zijn voor dynamische metingen van scheurpropagatie onder vermoeiing. En de ruimtelijke resolutie en nauwkeurigheid is superieur ten opzichte van de nieuwste schade detectietechnieken.

Tot slot worden, om de nauwkeurigheid van de schade detectiealgoritmen te verbeteren, twee verschillende methodes voorgesteld om nauwkeurig de lengte van de FBG sensor te bepalen en zijn positie in de optische glasvezel. Deze informatie wordt meestal niet nauwkeurig verstrekt voor commerciële FBG sensoren. Dit kan ongunstig invloed hebben op de nauwkeurigheid van het kraakpunt lokalisatie-algoritme. Met de algoritmes uit dit proefschrift kan de positie van de FBG sensoren in de optische glasvezel bepaald worden met micrometer nauwkeurigheid.

1

INTRODUCTION

... and a fact is the most stubborn thing in the world.

Mikhail Bulgakov, The Master and Margarita

In the past few decades, fibre Bragg grating (FBG) sensors have developed significantly in structural health monitoring applications. Their light weight and small size, along with their immunity to electromagnetic interferences and long distance interrogation capability, has made them an ideal candidate for embedded and remote sensing applications [1]. In these applications, FBG sensors are typically used for point stress measurements, where the stress fields along the sensors' lengths are assumed to be uniform [1, 2]. In such conditions, the amount of strain applied over the length of the sensor can be estimated in a straightforward way. However, uniformity of the strain field is not a valid assumption in most applications of FBG sensors, especially not when the FBG length is bare and is not encompassed in a casing [3, 4]. For instance, in embedded applications, the sensor is already under transverse loads, which results in birefringence effects [5], and in surface mounting applications, the adhesive material creates a non-uniform residual stress field over the length of the sensor [2, 6].

The research underlying this thesis is part of the "Smart Sensing for Aviation" project at Delft University of Technology, which aims to improve the safety, security and efficiency over the life cycle of aircrafts, with a focus on the safety of composite structures in aircrafts. This thesis, provides fundamental contributions to the interpretation of the FBG sensor output under non-uniform strain fields, with a focus on their application in aerospace composite structures. The analyses presented in this work are meant to give a better understanding of the strain field to which the sensor is subjected, which can be further developed into damage detection schemes. In this chapter, the reader will be first provided with some basic information about aerospace composite materials. Then, an introduction to structural health monitoring (SHM) and the application of FBG sensors in SHM will be given. In Section 1.6 the scope and the outline of this thesis will be discussed, and finally, the main contributions of this thesis are detailed.

1

1.1. AEROSPACE COMPOSITE MATERIALS

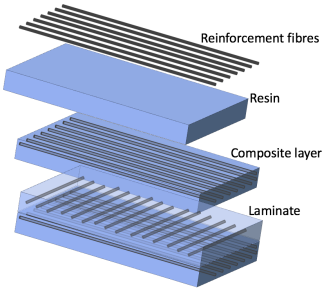

(a)

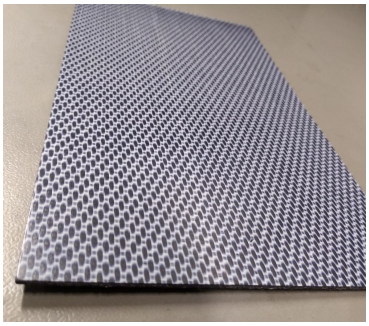

(b)

Figure 1.1: (a): A schematic representation of different layers of a unidirectional fibre reinforced composite material (b): An actual piece of a woven carbon fibre composite material.

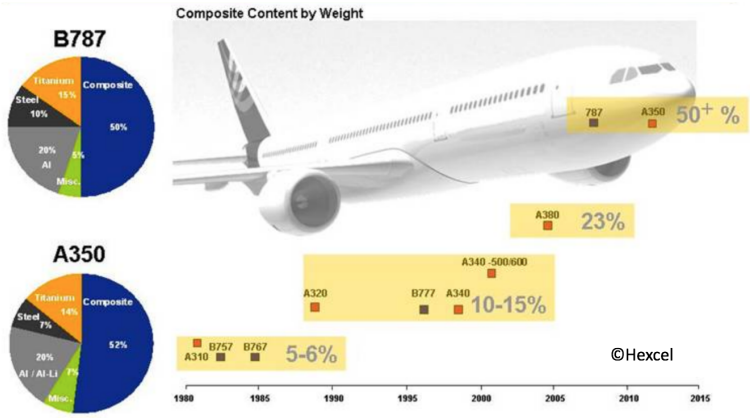

Figure 1.2: The amount of composite content in aircrafts has increased significantly in the past few decades [10].

A composite material, based on definition, is a material that consists of two or more composing materials, which, when combined, produces a material with physical and chemical characteristics significantly different than its individual components [7]. In continuous fibre reinforced composite materials, which have dominated the aerospace field [8], the composite material consists of long reinforcement fibres and a matrix material. These reinforcement fibres can be oriented in desired directions or be in woven form to improve the strength and stiffness of the material, and the matrix material, which is usually in form of a liquid or gel resin mixture which has been cured to fill the volume between the reinforcement fibres. Fig. 1.1 presents a schematic and a real example of a composite material.

The resulting composite material has several advantages over metals. They are lighter in weight, have higher stiffness, are more resilient to temperature changes, and are becoming

more and more affordable for aerospace applications [8]. Before composites, aluminium alloys were the most commonly used material in aerospace structures. Although they have many suitable physical properties, they are prone to ageing, corrosion, fatigue and mechanical damage due to surface contact, which makes them expensive to maintain and repair. Composite materials, and in particular fibre reinforced composites have shown to be a good substitute for aluminium alloys, with much less maintenance costs and a better performance [8]. Fig. 1.2 is a good demonstration of the increasing popularity of composites in commercial aircrafts.

1.2. STRUCTURAL HEALTH MONITORING IN COMPOSITES

One of the main concerns regarding the use of composite materials in aerospace applications is the formation and growth of damages in them, and in particular, barely visible damages [8, 9]. Such barely visible damages can be induced during the operational lifetime of an aircraft due to low velocity impacts, and they cannot be detected by routine visual inspections, especially if they occur in the internal layers of composites [2, 8]. These damages are usually in the form of matrix micro-cracks, or delamination of the composite layers. Under fatigue and stress, if left unattended, these damages can grow and result in catastrophic incidents [8]. Fig. 1.3 shows an example of such micro-cracks in the internal layers of a unidirectional carbon fibre composite specimen under two different stress levels.

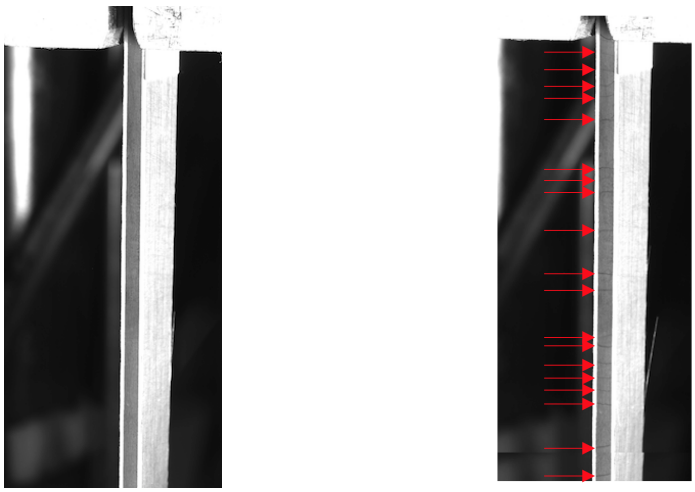

(a) (b)

Figure 1.3: (a): A side-view of a healthy composite specimen before applying any load. (b): Applying tensile load on the specimen and the formation of transverse micro-cracks (indicated by the red arrows) in the middle layers of the composite specimen.

Structural health monitoring is the process of detection and characterisation of damage and stress in engineering structures [8]. This process is performed by incorporating an array of sensors to collect data about the mechanical behaviour of the structure, and analysing the changes in the sensors' outputs. In general, structural health monitoring techniques are used

for

1. studying the behaviour of composites under various load scenarios,

2. detecting barely visible damages at early stages.

In the first group of the above categorisation, the stress analysis of the composite specimens are first carried out in computer simulations by using engineering models [11]. The data collected from these simulations (usually using finite element methods) are then compared to experimental measurements from the actual specimens [11]. It is therefore essential to have accurate and precise measurements from the physical experiments. The sensors used in the research underlying this thesis are a specific kind of fibre optic based sensors, called fibre Bragg gratings (FBG). This thesis will try to answer a few fundamental questions in both categories mentioned above. In the next section, the properties and advantages of FBG sensors will be discussed in details.

1.3. FIBRE BRAGG GRATINGS (FBGS)

Fibre Bragg grating sensors are manufactured by inducing a refractive index modulation in the core of an optical fibre. This modulated length, called the grating, is typically around 1 cm in length, and is created by exposing the optical fibre to ultraviolet (UV) light with a specific pattern [4]. In uniform FBG sensors, which is the focus of this thesis, the aforementioned refractive index modulation has a constant period throughout the length of the sensor [4, 12]. The active length of the sensor partially reflects certain wavelengths of the input light, and the peak wavelength of the amplitude of the reflected spectrum (which is theoretically symmetrical), depends linearly on the period of the grating. This means that if the FBG sensor undergoes a uniform axial strain, the period of the grating will be mechanically altered (increased under tension and decreased under compression), and hence, the peak wavelength of the reflected spectrum will shift towards higher or lower wavelengths, respectively. This simple relationship between the strain value and the peak wavelength of the reflection spectrum has made FBGs an attractive choice for stress analyses in mechanical structures, and in particular in point strain and temperature measurements [12, 13]. Fig. 1.4 demonstrates this property schematically.

Apart from the simple relationship between the Bragg wavelength and the strain value, FBG sensors have several advantages over other sensor types, including their extremely low sensitivity to electromagnetic interferences, their resistance to corrosion and long working lifetime, the low loss of fibre optics in long distances, and their remote sensing capabilities [2]. However, the two features that makes them an ideal option for aerospace applications is their light weight and the small diameter of the optical fibre. This small diameter (ranging from around 40 μm [14] to around 125 μm for standard FBG sensors [15]), allows them to be embedded between the layers of composite materials, without severely altering their mechanical properties [14, 16]. By doing so, one can have direct information about the internal layers of composites, which can possibly help them to interpret the applied load or the damage state within the internal layers.

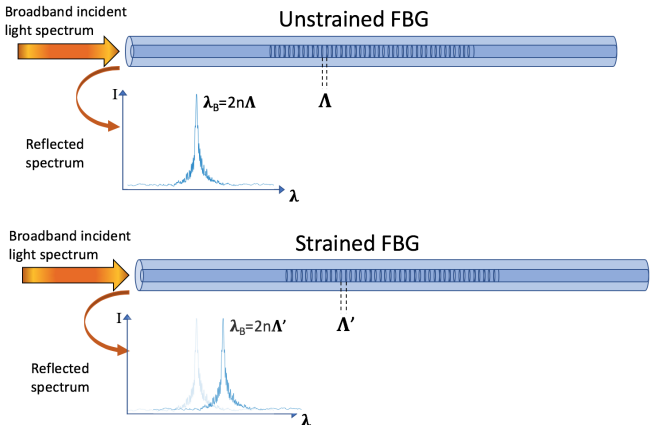

Figure 1.4: The principle of operation of uniform FBG sensors under uniform strain fields. I is the intensity of the reflected light, λ is the wavelength domain, λ_B is the peak wavelength of the reflected light, n is the effective refractive index of the core, and Λ and Λ' are the grating periods of the unstrained and strained FBG respectively.

1.3.1. INTERROGATION OF FBG SENSORS

There are several methods for the interrogation of FBG sensors, and they all have their limitations and advantages. Here, only the most basic interrogation types will be discussed. The simplest approach is to use conventional spectrometers in combination with a light-source such as a superluminescent diode or a tunable laser [17]. This is an affordable and simple approach for recording the amplitude of the reflection spectrum, but its wavelength resolution is low and it is not suitable for full spectrum analysis of the FBG output.

Another approach is to incorporate a tunable Fabry-Perot filter in the design of the interrogator, along with a broadband source and a photodetector for recording the amplitude of the reflection spectrum [18]. This approach offers a high wavelength resolution and accuracy, and a high dynamic range. However, its scanning frequency is relatively low (typically less than 1 kHz), and high speed and dynamic interrogation is challenging with such systems [19]. Despite these drawback, this system will be used throughout this thesis, as it offers multiplexing capabilities and full reflection spectra recordings with a high wavelength resolution. Such detailed reflection spectra with a high wavelength resolution contains essential information about the non-uniform strain field around the FBG sensor, and since the focus of this thesis is on static measurements, the low speed of Fabry-Perot based interrogation systems is not an issue.

So far, only the interrogation types that recorded the amplitude of the FBG reflection spectrum were discussed. There is another class of interrogators, based on the optical low-coherence reflectometry (OLCR), that record the complex reflection spectrum of the FBG sensor [20]. The principles of operation of such systems will be discussed in the next chapter in detail. Using such systems, it is possible to retrieve the local coupling coefficients along the FBG length, and consequently to reconstruct the continuous (so-called distributed) axial strain field along the FBG length [21]. With this method it is possible to retrieve a significant amount of information about the non-uniform strain field, and to use that information for damage characterisation in different engineering structures. However,

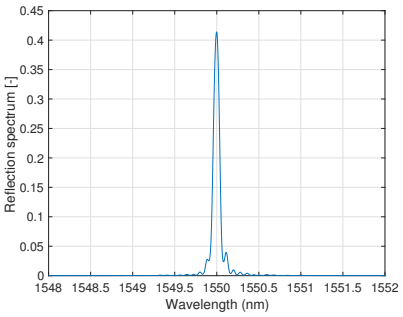

(a)

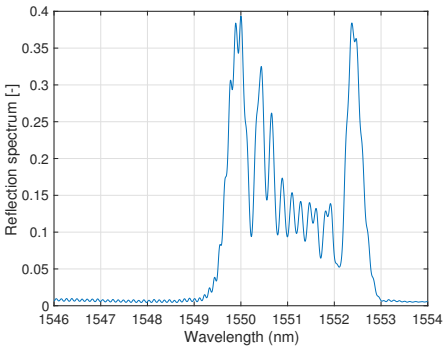

(b)

Figure 1.5: FBG reflection spectrum under (a) no external stress, and (b) a non-uniform strain field. The reflection spectrum in (b) is from an experiment where embedded FBG sensors were in contact with delaminated composite layers.

the setup of the OLCR system limits its multiplexing capabilities, is sensitive to transverse loads and polarisation effects, and due to the existence of moving arms in the interrogation system, its speed is relatively low [22]. Further, strain distribution reconstruction algorithms take several seconds to converge [23], which limits its application. For these reasons, the application of the OLCR system for damage identification will not be further discussed in this thesis, as here the focus is on reducing the computational complexity of structural health monitoring methods and increasing their speed and reliability.

1.3.2. FBG SENSORS FOR STRAIN MEASUREMENT

Despite the simplicity of interpreting the FBG reflection spectrum under uniform strain fields under non-uniform strain fields, the reflection spectrum becomes complicated containing multiple peaks. An example is shown in Fig. 1.5b where an FBG sensor is in contact with a non-uniform strain field from delaminated composite layers.

Even though in embedded applications and composite materials the strain field is usually non-uniform, and to our knowledge there has not been many studies to interpret the FBG reflection spectra for strain estimation under such conditions. Therefore, the first research question can be posed as:

Q1: With only the magnitude of the FBG reflection spectra available, is it possible to provide a meaningful measure of non-uniform strain fields?

We first present a model for the analysis of FBG sensors under non-uniform strain fields in Chapter 3, which will be used in Chapters 3 and 4 to answer this question.

1.4. IMPROVING THE PERFORMANCE OF FBG SENSORS IN DAMAGE CHARACTERISATION

In damage detection and localisation applications, it is essential to know the precise position of the FBG sensor along the optical fibre. The reason is that, for instance, the precision of the delamination tip localisation is directly determined by our precise knowledge of the position of the FBG sensor. Upon ordering FBG sensors from manufacturing companies, there is usually ambiguity on the precise location of the FBG sensor along the length of the optical fibre, as the markings on the fibre only indicate the approximate position of the FBG sensor. Therefore, the second question that will be addressed in this thesis is:

Q2: Can we extract knowledge on the precise position of the FBG sensor?

In Chapters 5 and 6, this question will be answered.

1.5. FBG SENSORS AND DAMAGE CHARACTERISATION

The strain field around the damaged area in composites is highly non-uniform. For instance, the strain distribution in the direction transverse to matrix cracks will have high amplitude peaks at the crack locations [24], and the strain distribution along the delamination area will have a sudden strain change at the delamination tip [25] (see Fig. 1.5). As mentioned in the previous sections, when FBG sensors get in contact with non-uniform strain fields, their reflection spectra lose their symmetry and usually become wider (similar to Fig. 1.5b).

In the past decades, a lot of research has been conducted to exploit these phenomena and to design a reliable damage detector using FBG sensors [23–27]. However, due to the complications associated with the analysis of FBG reflection spectra under non-uniform strain fields, most of this research was only limited to a qualitative assessment of the changes in the FBG reflection spectra. In Chapters 7 and 8 of this thesis, the following two related subquestions will be answered.

Q3.1: Having access to only the magnitude of the FBG reflection spectra available, is it possible to quantifiably characterise matrix cracks in composites?

Q3.2: Is it possible to monitor the delamination growth direction and extent in composites, both accurately and dynamically?

1.6. THESIS OUTLINE AND CONTRIBUTIONS

In general, the direct application of FBG sensors in SHM can be classified into two categories. The first category, which is also the most prevalent application in the industry, is to use FBG sensors for point strain (or temperature) measurement. The second category is concerned with damage identification and detection in engineering structures. This thesis makes contributions to certain applications within both categories, and is particularly focused on the case of the effects of non-uniform strain fields on FBG reflection spectra. It should be noted that each of these categories consists of several different classes of methods and algorithms, each of which is most suited for a particular set of structural health monitoring problems. Fig. 1.7 presents a diagram of the typical applications of FBG sensors in

SHM, and highlights the main contributions of this thesis. In the next chapter, a selection of these methods will be explained in further detail.

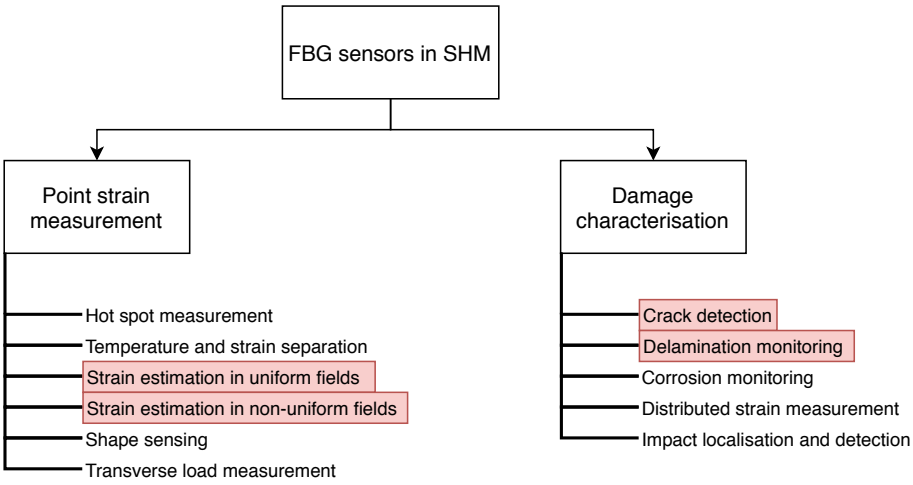

Figure 1.7: Typical applications of FBG sensors in SHM, classified into two categories. The contributions of this thesis lie within the highlighted areas.

The remainder of this chapter, provides a brief description of the thesis contributions summarised per chapter.

Chapter 2 - Literature review. This chapter covers the required background in order to read this thesis, along with a selection of the existing methods of structural health monitoring using FBG sensors. The chapter contains the presentation of the transfer matrix model, which is a method for modelling the FBG reflection spectra under non-uniform strain or grating distributions, and will form the backbone of this thesis. The existing strain estimation algorithms and damage assessment methods in composite structures using FBG sensors in the literature will be discussed as well. Furthermore, there are also several practical considerations that need to be taken into account for using FBG sensors in structural health monitoring applications, especially in embedded applications. This chapter will briefly discuss some of these challenges and some solutions to overcome them as well.

Chapter 3 - FBG model and average strain estimation. In this chapter, a new model for the analysis of FBG reflection spectra under non-uniform strain or grating distributions will be proposed. This model is an approximation of the transfer matrix model and is the basis of all the analyses in this thesis. Using this model, we are able to express the reflection spectra under non-uniform strain fields with a closed-form approximation. This closed-form expression will help us to develop several new applications for FBG sensors in areas such as accurate strain estimation and damage detection. As an example an algorithm will be presented for estimating the average of non-uniform strain distributions that uses the aforementioned closed-form approximation. The chapter concludes with some computer simulations and experimental measurements to validate our claims.

Chapter 4 - Average strain estimation with uniform FBGs. One of the methods of strain estimation using FBG sensors is to replace the peak wavelength tracking approach by tracking the centre of mass of the reflection spectrum. This method is called the centroid method, and a mathematical proof for the superior performance of this method over the other commonly used existing average strain estimation methods will be given. The centroid method is also one of the steps of the algorithm that will be presented in Chapter 3. Chapter 4 thus complements Chapter 3. The performance of the centroid method under spectral noise will be investigated as well. This chapter will be concluded with some computer simulation results.

Chapter 5 and 6 - Accurate FBG length and position determination. In these two chapters, a new method will be presented to determine the exact length of the FBG sensor (Chapter 5) and its exact position along the optical fibre (Chapter 6). This information will become useful in the next chapters of this thesis, as the precision of the damage identification methods directly depends on our precise knowledge of the position of the sensor. However, manufacturing companies only offer the approximate position of the sensor along the optical fibre, whose accuracy is at best around 1 mm. In these chapters, a method will be presented that will improve this accuracy by a factor of around 100.

Chapter 7 - Matrix crack detection with FBG sensors. In this chapter, the information presented in Chapters 3 and 5 and 6 will be exploited to devise a new method for the characterisation of transverse matrix cracks in composite materials. First, McCartney's theory will be presented which analyses the strain field around transverse cracks in composites. This theory suggests that when subject to transverse cracks, the strain distribution along the FBG length will have sudden changes at the crack locations. Using the aforementioned closed-form expression of the reflection spectrum, it will be shown that such sudden strain changes along the FBG length translate into the addition of new harmonics in the Fourier transform of its reflection spectrum side-lobes. Using this novel method, high resolution information about the formation of matrix cracks in the internal layers of uni-directional composites can be provided. Experimental results from carbon fibre and glass fibre composite specimens will be presented to confirm these claims.

Chapter 8 - Delamination tip monitoring with FBG sensors. This chapter will investigate the possibility of delamination growth monitoring in mode-I fracture tests. The damage type that will be investigated in this chapter is delamination of the composite layers. It will be argued that under delamination, there is also a sudden strain change at the delamination tip. By increasing the amount of the tensile load on the specimen (and progression of the delaminated area), that delamination tip moves along the FBG length. Such conditions result in a moving harmonic in the Fourier transform of the reflection spectrum side-lobes, which can be monitored to determine the exact position of the delamination tip. This is a novel and useful application for FBG sensors, as it can potentially provide a real-time, precise and distributed evaluation of the delamination tip growth in composites, within their internal layers, and independent of the type of composite material. Computer simulations and experimental results also confirm these claims.

1

Chapter 9 - Conclusions. This thesis is concluded in this chapter by summarising our main contributions. The possible directions for future work based on our contributions will be discussed afterwards, as well as the limitations and challenges that might be in the way.

1.7. LIST OF PAPERS

In this section, all the papers that were submitted and published during the course of this PhD project are listed.

JOURNALS

1. **A. Rajabzadeh**, R. Heusdens, R. C. Hendriks, R. M. Groves, *Calculation of the mean strain of smooth non-uniform strain fields using conventional FBG sensors,* Journal of Lightwave Technology (2018).

2. **A. Rajabzadeh**, R. Heusdens, R. C. Hendriks, and R. M. Groves, *A Method for Determining the Length of FBG Sensors Accurately*, IEEE Photonics Technology Letters (2019).

3. **A. Rajabzadeh**, R. Heusdens, R. C. Hendriks, and R. M. Groves, *Characterisation of Transverse Matrix Cracks in Composite Materials Using Fibre Bragg Grating Sensors*, Journal of Lightwave Technology (2019).

4. I. G. Tapeinos, **A. Rajabzadeh**, D. S. Zarouchas, M. Stief, R. M. Groves, S. Koussios, R. Benedictus, *Evaluation of the mechanical performance of a composite multi-cell tank for cryogenic storage: Part -II Experimental assessment*, International Journal of Hydrogen Energy (2019).

5. **A. Rajabzadeh**, R. Heusdens, R. C. Hendriks, and R. M. Groves, *On the Centroid Method for Average Strain Estimation in Uniform FBG Sensors*, Submitted to Journal of Strain.

6. **A. Rajabzadeh**, R. C. Hendriks, R. Heusdens, and R. M. Groves, *Accurate Delamination Tip Monitoring of Laminated Composites in Mode-I Fatigue Tests Using FBG Sensors*, Submitted to Journal of Experimental Mechanics.

MAGAZINES

1. **A. Rajabzadeh**, N. Nazeer, L. Fazzi, R. M. Groves, *Fiber optic sensing for aerospace structures*, Photonics Magazine Netherlands (PhotonicsNL magazine) (2018).

CONFERENCES

1. **A. Rajabzadeh**, R. C. Hendriks, R. Heusdens, R. M. Groves, *Classification of composite damage from FBG load monitoring signals*, SPIE Smart Structures and Materials + Nondestructive Evaluation and Health Monitoring (2017).

2. **A. Rajabzadeh**, R. M. Groves, R. C. Hendriks, R. Heusdens, *Modelling non-uniform strain distributions in aerospace composites using fibre Bragg gratings*, 25th Optical Fiber Sensors Conference (OFS) (2017).

3. **A. Rajabzadeh**, R. C. Hendriks, R. Heusdens, R. M. Groves, *Analysis of FBG reflection spectra under anti-symmetrical strain distributions using the approximated transfer matrix model*, SPIE Photonics Europe (2018) [**Best student paper award**].

4. **A. Rajabzadeh**, R. Heusdens, R. C. Hendriks, R. M. Groves, *Analysis of the Sidelobes of FBG Reflection Spectra From Matrix Cracks in Composites*, 26th Optical Fiber Sensors Conference (OFS) (2018).

5. I. Tapeinos, **A. Rajabzadeh**, D. Zarouchas, R. M. Groves, S. Koussios, R. Benedictus, *Design and Experimental Assessment of a Multi-spherical Composite-Overwrapped Pressure Vessel for Cryogenic Storage*, ECCM18: 18th European Conference on Composite Materials (2018).

6. L. Fazzi, **A. Rajabzadeh**, A. Milazzo, R. M. Groves, *Analysis of FBG reflection spectra under uniform and non-uniform transverse loads*, SPIE Smart Structures + Nondestructive Evaluation (2019).

7. **A. Rajabzadeh**, R. C. Hendriks, R. Heusdens, R. M. Groves, *A method for determining the position of FBG sensors accuratel*, Seventh European Workshop on Optical Fibre Sensors (EWOFS) (2019).

SYMPOSIA

1. **A. Rajabzadeh**, R. Heusdens, R. C. Hendriks, R. M. Groves, *Calculating the Mean Strain Under Non-uniform Strain Distributions in Conventional FBG Sensors*, WIC/IEEE SP Symposium on Information Theory and Signal Processing in the Benelux (2018).

2. **A. Rajabzadeh**, R. M. Groves, R. Heusdens, R. C. Hendriks, *On the Centroid Method as the Optimal Average Strain Estimator in FBG Sensors*, WIC/IEEE SP Symposium on Information Theory and Signal Processing in the Benelux (2019).

3. **A. Rajabzadeh**, R. C. Hendriks, R. Heusdens, R. M. Groves, *Apodized FBG sensors in Structural Health Monitoring Applications*, Measuring by Light (MBL) meets OPTIMESS (2019).

REFERENCES

[1] R. Kashyap, “Fiber Bragg Gratings,” Academic Press, 2009.

[2] E. Udd, W. B. Spillman Jr, “Fiber Optic Sensors: An Introduction for Engineers and Scientists,” John Wiley & Sons, 2011.

[3] A. D. Kersey, M. A. Davis, H. J. Patrick, M. LeBlanc, K. Koo, C. Askins, M. Putnam, and E. J. Friebele, “Fiber grating sensors,” *Journal of Lightwave Technology*, vol. 15, no. 8, pp. 1442-1463, 1997.

[4] Y. J. Rao, “Recent progress in applications of in-fibre Bragg grating sensors,” *Optics and Lasers in Engineering*, vol. 31, no. 4, pp. 297-324, 1999.

[5] Y. Wang, B. Yun, N. Chen, Y. Cui, "Characterization of a high birefringence fibre Bragg grating sensor subjected to non-homogeneous transverse strain fields," *Measurement Science and Technology*, vol. 17, no. 4, pp 939, 2006.

[6] R. Gafsi, M. A. El-Sherif, "Analysis of induced-birefringence effects on fiber Bragg gratings," *Optical Fiber Technology*, vol. 6, no. 3, pp. 299-323, 2000.

[7] D. Gay, S. V. Hoa, "Composite materials: design and applications," CRC Press, 2007.

[8] V. Giurgiutiu, "Structural health monitoring of aerospace composites," Academic Press, 2015.

[9] U. Polimeno, M. Meo, "Detecting barely visible impact damage detection on aircraft composites structures," *Composite Structures*, vol. 91, no. 4, pp. 398-402, 2009.

[10] Anon. "Composites Penetration-Step Change Underway with Intermediate Modulus Carbon Fiber as the Standard", Hexcel Corporation, http://www.sec.gov/Archives/edgar/data/717605/000110465908021748/g97851bci012.jpg, Accessed April 2019.

[11] R. D. Cook, "Finite element modeling for stress analysis," *Wiley*, 1994.

[12] T. Erdogan, "Fiber grating spectra," *Journal of Lightwave Technology*, vol. 15, no. 8, pp. 1277-1294, 1997.

[13] D. Kinet, P. Mégret, K. W. Goossen, L. Qiu, D. Heider, and C. Caucheteur, "Fiber Bragg grating sensors toward structural health monitoring in composite materials: Challenges and solutions," *Sensors*, vol. 14, no. 4, pp. 7394-7419, 2014.

[14] K. Satori, K. Fukuchi, Y. Kurosawa, A. Hongo, N. Takeda, "Polyimide-coated small-diameter optical fiber sensors for embedding in composite laminate structures," *Smart Structures and Materials 2001: Sensory Phenomena and Measurement Instrumentation for Smart Structures and Materials*, vol. 4328, pp. 285-295, 2001.

[15] A. Mendez, "Fiber Bragg grating sensors: a market overview," *Third European Workshop on Optical Fibre Sensors*, vol. 6619, pp. 661905, 2007.

[16] K.Kuang, R. Kenny, M.P. Whelan, W.J. Cantwell, WJ and P.R. Chalker, "Embedded fibre Bragg grating sensors in advanced composite materials," *Composites Science and Technology*, vol. 61, no. 10, pp. 1379-1387, 2001.

[17] L. A. Parkinson, P. R. Cook, A. Ruiz-Vargas, J. W. Arkwright, "Correction of peak tracking ripple in solid state spectrometers," *Journal of Lightwave Technology*, vol. 36, no. 18, pp. 3912–3918, 2018.

[18] A. D. Kersey, T. A. Berkoff, W. W. Morey, "Multiplexed fiber Bragg grating strain-sensor system with a fiber Fabry–Perot wavelength filter," *Optics Letters*, vol. 18, no. 16, pp. 1370–1372, 1993.

[19] A. Hongo, S. Kojima, S. Komatsuzaki, "Applications of fiber Bragg grating sensors and high-speed interrogation techniques," *Structural Control and Health Monitoring*, vol. 12, no. 3, pp. 269-282, 2005.

[20] J. Botsis, L. Humbert, F. Colpo, P. Giaccari, "Embedded fiber Bragg grating sensor for internal strain measurements in polymeric materials," *Optics and Lasers in Engineering*, vol. 43, no. 3, pp. 491-510, 2005.

[21] J. Skaar, L. Wang, T. Erdogan, "On the synthesis of fiber Bragg gratings by layer peeling," *IEEE Journal of Quantum Electronics*, vol. 37, no. 2, pp. 165-173, 2001.

[22] L. Sorensen, "The response of embedded FBG sensors to non-uniform strains in CFRP composites during processing and delamination," *Doctoral dissertation*, EPFL, 2007.

[23] L. Sorensen, J. Botsis, T. Gmür, J. Cugnoni, "Delamination detection and characterisation of bridging tractions using long FBG optical sensors," *Composites Part A: Applied Science and Manufacturing*, vol. 38, no. 10, pp. 2087-2096, 2007.

[24] Y. Okabe, T. Mizutani, S. Yashiro, N. Takeda, "Detection of microscopic damages in composite laminates," *Composites Science and Technology*, vol. 62, no. 7, pp. 951-958, 2002.

[25] S. Takeda, Y. Okabe, N. Takeda, "Monitoring of delamination growth in CFRP laminates using chirped FBG sensors," *Journal of Intelligent Material Systems and Structures*, vol. 19, no. 4, pp. 437-444, 2008.

[26] C. K. Coelho, S. Das, A. Chattopadhyay, "A hierarchical classification scheme for computationally efficient damage classification," *Proceedings of the Institution of Mechanical Engineers, Part G: Journal of Aerospace Engineering*, vol. 223, no. 5, pp. 497-505, 2009.

[27] A. R. Chambers, M. C. Mowlem, and L. Dokos, "Evaluating impact damage in CFRP using fibre optic sensors," *Composites Science and Technology*, vol. 67, no. 6, pp. 1235-1242, 2007.

2

Structural Health Monitoring with FBG Sensors

A man trusts another man when
he sees enough of himself in him.

Gregory David Roberts, Shantaram

In this chapter, the focus will be on reviewing the background knowledge on fibre Bragg grating (FBG) sensors in structural health monitoring (SHM) that is required to read this thesis. Since the introduction of fibre Bragg gratings as strain and temperature sensors [1], their performance and accuracy has improved significantly [2], their mechanical strength has increased [3], and their applications in structural health monitoring have become much more diverse [4–7]. These applications range from the conventional point axial strain estimation applications under different adverse conditions to non-uniform strain estimation, damage identification in smart structures, and distributed strain measurements. In this chapter, a selection of the most significant contributions in the field of structural health monitoring using FBG sensors will be discussed.

This chapter starts with the case of uniform axial strain or temperature fields, which is the simplest case of using fibre Bragg gratings as sensor elements in structural health monitoring. However, even within this framework, there can be complications in retrieving the strain or temperature values. For instance, if the wavelength resolution of the interrogation unit is low but a high strain resolution is desired, or if the recorded FBG output from the interrogator has a low signal-to-noise ratio. In Section 2.1.1, a number of different methods will be presented that try to increase the strain accuracy and resolution of the interrogation by using signal processing techniques, without altering the hardware of the signal interrogation unit.

The second part of this chapter (Section 2.2) addresses the analysis of the FBG output under non-uniform axial strain fields. Section 2.2 is an essential part of this thesis, as all

damage types in engineering structures lead to non-uniform strain fields at the affected area. This phenomenon is the foundation for the remaining chapters of this thesis, where the extent and the size of different damage types in composites will be characterised. This subsection will start with a mathematical model for the analysis of the FBG output under non-uniform grating structures or stress fields. Then, several studies will be mentioned and discussed that have tried to interpret the FBG output from a damaged composite structure in order to detect the mere existence of the damage, its type, its location, or the direction of its progression.

In the last part of this chapter, the use of FBG sensors as distributed sensors will be investigated. For such applications, the interrogation system needs to record the complex reflection spectrum of the sensor, which requires adjustments to the interrogation method and its setup. This part is beyond the scope of the current thesis, however, exploring the benefits of these methods, as well as understanding the complications associated with them and their limitations, will help the reader to better understand the contributions of this thesis. This chapter concludes with some remarks about the embedding process of fibre optic sensors between composite laminates.

2.1. FBG SENSOR UNDER UNIFORM STRAIN

The basic principle of operation of FBG sensors under uniform strain fields is to track the wavelength shift of the reflected light from the grating region. In its simplest form, the peak wavelength of the FBG reflection spectrum (also called the Bragg wavelength) is given by [8]

$$\lambda_B = 2 n_{\text{eff}} \Lambda, \tag{2.1}$$

where n_{eff} is the effective index of the core and Λ is the grating period of the sensor. As evident from Eq. (2.1), the Bragg wavelength of the sensor linearly depends on the grating period and on the effective index of the core. Therefore, under the application of physical stresses such as temperature changes or mechanical strains, the Bragg wavelength will shift toward higher (under tension) or lower (under compression) wavelengths. It is noteworthy that this linear response is most valid for small temperature and strain changes. For larger temperature variations and at cryogenic temperatures, the thermo-optic coefficient of the silica fibre also becomes a dominant factor and changes the FBG response from linear dependence to temperature to quadratic dependence or sometimes higher-order polynomials [9].

Based on this linearity property, the amount of uniform axial strain or temperature change applied over the sensor length can be determined by tracking the shift of this peak wavelength under stress with respect to that of the unstressed sensor. This property was depicted in Fig. 1.4, where the shift of the reflection spectrum of the FBG sensor (throughout this thesis the reflection spectrum is denoted by $R(\lambda)$) was depicted to linearly depend on the amount of uniform strain applied over the sensor length. Another parameter in Eq. (2.1) that is affected by these physical stresses is changes in the effective refraction index or Δn_{eff}. This index can have components in both x and y axes (transverse directions), which will be denoted as $\Delta n_{\text{eff},x}$ and $\Delta n_{\text{eff},y}$ respectively. The shift of the effective refraction index is given by [10]

$$\Delta n_{\text{eff},x} = -\frac{n_{\text{eff}}^3}{2}\Big[p_{11}\varepsilon_x + p_{12}(\varepsilon_y + \varepsilon_z)\Big] + \frac{dn_{\text{eff}}}{dT}\Delta T, \tag{2.2}$$

$$\Delta n_{\text{eff},y} = -\frac{n_{\text{eff}}^3}{2}\Big[p_{11}\varepsilon_y + p_{12}(\varepsilon_x + \varepsilon_z)\Big] + \frac{dn_{\text{eff}}}{dT}\Delta T. \tag{2.3}$$

In the above equations, the ε_i's are the strain components along different axes, p_{11} and p_{12} are the strain-optic coefficients, and $\frac{dn_{\text{eff}}}{dT}$ represents the thermal-optic effect [11]. It can be seen from Eq. (2.2) that if the transverse load has unequal components along the x and y directions, the shift of Bragg wavelength will also have different changes due to each component [12]. This phenomenon results in birefringence or the split of the reflection spectrum into two or more peaks, as shown in Fig. 2.1.

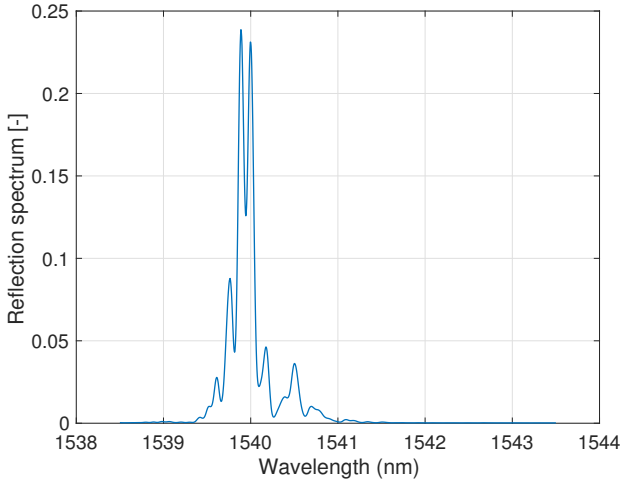

Figure 2.1: Experimental results, showing the birefringence effect of the FBG reflection spectrum under a uniform transverse load of 5 N.

Nonetheless, assuming almost equal transverse strains along both the x and y directions is a valid assumption for several applications of FBG sensors in structural health monitoring, especially when appropriate coatings are used for the optical fibre [13]. With this simplification, the shift of the Bragg wavelength with respect to both temperature change and axial strain is determined as $\Delta\lambda_B = \Delta\lambda_{B_\epsilon} + \Delta\lambda_{B_T}$, where

$$\Delta\lambda_{B_\epsilon} = k_s s \quad \text{and} \quad \Delta\lambda_{B_T} = k_T \Delta T. \tag{2.4}$$

In Eq. (2.4), $s = \varepsilon_z$ is the axial strain, and both k_s and k_T are constants and are determined by the composition of the optical fibre. For instance, in silica based optical fibres operating at $\lambda_B = 1550$ nm, $k_s \approx 1.209 \times 10^{-3}\,\text{nm}/\mu\epsilon$ and $k_T \approx 10.075 \times 10^{-3}\,\text{nm}/^\circ C$ [8].

As it is evident from Eq. (2.4), the shift of the Bragg wavelength is sensitive to both strain and temperature changes. Therefore, in the case that the sensor is subjected to a

mixed environment with both effects present, separating the amount of mechanical strain from the change in temperature based on a single FBG measurement will become a problem as the system of equations in underdetermined. To solve this problem, the most straightforward solution is to incorporate two FBG sensors in the object under test, one as a reference for measuring the temperature changes and not undergoing strain, and another FBG sensor that undergoes both effects [14]. Then, solving a linear system of two equations and two unknowns (temperature and strain), both parameters can be obtained. Another solution is to use individual Bragg grating sensors with two or multiple peaks, including FBG sensors inscribed in PANDA fibres [15], birefringence-induced FBG sensors [16], or π-phase shifted FBG sensors [17]. The demodulation method is again based on solving a linear system of equations, and retrieving both the temperature and the strain values.

Nevertheless, in well-controlled laboratory conditions one can assume the temperature field to be constant. This is also the case within the scope of this thesis, and from here onwards the effect of temperature fields will be neglected. That being said, the methods presented for damage detection in composites, both in this chapter and in the future chapters, are insensitive to uniform temperature changes.

2.1.1. STRAIN ESTIMATION UNDER UNIFORM AXIAL STRAIN FIELDS

As mentioned in the previous section, under uniform strain distributions, the most common demodulation technique for retrieving the strain value using FBG sensors is peak detection. Within this framework, there have been several methods proposed in the literature, each of which takes a different analysis approach of the reflection spectrum to track and estimate the strain value. In this section we will discuss the most common methods of strain estimation under such uniform strain fields. The most common method of FBG interrogation was already discussed in the previous section, which entails tracking the wavelength at which the FBG reflection spectrum is at its maximum amplitude [8]. Another approach is to track the shift of the centre of mass of the reflection spectrum [18], given by

$$\lambda_{B_c} = \frac{\int_{\boldsymbol{\lambda}} \lambda R(\lambda) d\lambda}{\int_{\boldsymbol{\lambda}} R(\lambda) d\lambda}, \tag{2.5}$$

in which $\boldsymbol{\lambda}$ is the wavelength region that covers the reflection spectrum under investigation. The advantage of this approach (also called the centroid method in the literature) compared to the maximum peak tracking method, is the higher accuracy of strain estimation as the retrieved shift of the centre of mass is not limited to the sample locations [18]. In particular, when the wavelength resolution of the FBG interrogation system is not high enough (for example the case with optical spectrometers), the quality of the centroid method becomes more beneficial. The centroid method will be discussed in much more detail in Chapter 4, where it will be argued that when used with non-apodized FBG sensors, this method can accurately retrieve the average of non-uniform strain fields.

The above-mentioned methods take into account the information in the FBG reflection spectrum directly. There exist several other methods that rely on curve fitting on the reflection spectrum. These include, but are not limited to Gaussian [19], polynomial [20], and spline fitting [21], in which the shift of the peak wavelength of the fitted curve is taken into account. Such methods are more suitable for reflection spectra with high spectral noise levels and they provide a better accuracy compared to the classic maximum peak track-

ing method. However, their computational complexity is higher than the direct methods of demodulation.

Other demodulation techniques include calculating the cross correlation between the reference and the shifted reflection spectrum [22], upsampling and interpolating the reflection spectrum [23], or demodulation techniques that are based on tracking the shift of certain features from the transformed reflection spectrum in other domains. For instance, transformations such as the Fourier transform [24], the discrete wavelet transform [25], and the Karhunen-Loeve transform [26] have been used in such studies. In [20] and [27], the performance of these methods have been benchmarked under different load scenarios, different interrogator resolutions, and different spectral noise levels.

In many of the above-mentioned methods the basic assumption is that the morphology of the reflection spectrum does not change under stress. Although this is also the underlying assumption for uniform strain distributions there are several cases in structural health monitoring where the strain distribution becomes non-uniform along the FBG length. In the next section, we will investigate the case with non-uniform strain distributions.

2.2. FBG SENSOR UNDER NON-UNIFORM STRAIN

The application of FBG sensors in structural health monitoring could include numerous cases where the strain field (in case of having damages in contact with the FBG), or the grating distribution (the case with chirped FBGs, phase shifted FBGs, or apodized sensors) along the sensor length is not uniform. In such cases the overall reflection spectrum of the FBG can be calculated by dividing the length of the sensor into several smaller reflective elements and taking into account the interaction of the electric waves between them. With such basis, there are several approaches in the literature that successfully determine the FBG reflection spectrum under non-uniform strain or grating distributions, including the Rouard's method [28], the lattice filter model [29] and the transfer matrix method [30]. This thesis focuses on the transfer matrix model, as within the context of this thesis it can adequately reconstruct the reflection spectrum [31], and it provides a mathematical basis that can be further developed for new applications. The transfer matrix model assumes a piece-wise uniform approximation of the strain (or grating) distribution along the FBG length where the length L of the sensor is divided into M virtual segments of length $\Delta z = L/M$. The transfer matrix model characterises the interaction of the forward and backward electric waves at each segment i (denoted by A_i and B_i respectively) with their previous segment $i-1$ through the following relations

$$\begin{pmatrix} A_{i-1} \\ B_{i-1} \end{pmatrix} = F_i \begin{pmatrix} A_i \\ B_i \end{pmatrix}, \tag{2.6}$$

where

$$F_i = \begin{pmatrix} \cosh(\gamma_i \Delta z) - j\frac{\Delta\beta_i}{\gamma_i}\sinh(\gamma_i \Delta z) & -j\frac{\kappa_i}{\gamma_i}\sinh(\gamma_i \Delta z) \\ j\frac{\kappa_i}{\gamma_i}\sinh(\gamma_i \Delta z) & \cosh(\gamma_i \Delta z) + j\frac{\Delta\beta_i}{\gamma_i}\sinh(\gamma_i \Delta z) \end{pmatrix}, \tag{2.7}$$

$\Delta\beta = 2\pi n_{\text{eff}}(\frac{1}{\lambda} - \frac{1}{\lambda_B}) + \frac{\pi}{\lambda}\delta n_{\text{eff}}$, δn_{eff} is the ac amplitude of the effective index modulation, λ is a given wavelength in the interrogation range of the sensor output, and $\gamma_i = \sqrt{\kappa_i^2 - \Delta\beta_i^2}$.

In Eq. (2.7), κ_i (the local coupling coefficient) and λ_{B_i} depend on the local Bragg wavelength shift and local effective refractive index, or equivalently on the local strain value and local refractive index at segment i along the FBG length. Looking back at Eq. (2.6) it is evident that the electric waves at the start of the first segment of the FBG model can be linked to the last segment through

$$\begin{pmatrix} A_0 \\ B_0 \end{pmatrix} = F \begin{pmatrix} A_M \\ B_M \end{pmatrix}, \quad \text{where } F = \prod_{i=1}^{M} F_i. \tag{2.8}$$

Taking into account the boundary conditions of full transmission and no reflection in the last segment (or $A_M = 1$ and $B_M = 0$) we can calculate A_0 and B_0 in the first segment. The reflected spectrum, $R(\lambda)$, is then determined as

$$R(\lambda) = \left| \frac{B_0}{A_0} \right|^2 = \left| \frac{F_{21}}{F_{11}} \right|^2, \tag{2.9}$$

where F_{21} and F_{11} are entries of the composite matrix F given in Eq. (2.8). Using the relations given in Eq. (2.7) through Eq. (2.9) we can reconstruct the FBG reflection spectrum under any arbitrary axial strain or grating distribution, with examples given in Fig. 2.2. In Fig. 2.2a, the reflection spectrum of a chirped Bragg grating is shown where the grating period is increased linearly along the grating length of length $L = 1$ cm, and Fig. 2.2b shows the reflection spectrum of a Gaussian apodized FBG sensor in which the induced index change (or subsequently the κ_i values) along the FBG length follow a Gaussian function with its highest index change at the centre of the sensor.

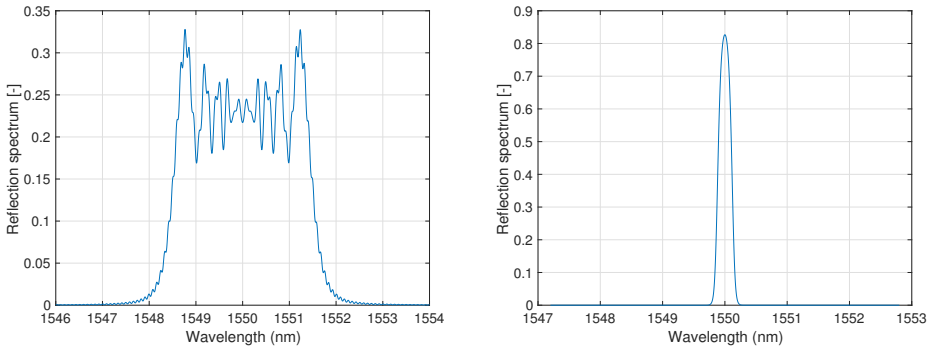

(a) (b)

Figure 2.2: (a): The calculated reflection spectrum from a chirped Bragg grating with a chirp rate of $d\lambda_B/dz = 3.34$ nm/cm. (b): The calculated reflection spectrum of a Gaussian apodized FBG sensor with fully suppressed side-lobes.

2.3. NON-UNIFORM STRAIN ESTIMATION WITH FBG SENSORS

In most applications of fibre Bragg grating sensors only the magnitude of the reflection spectrum (given in Eq. (2.9)) is recorded. In the literature there has only been a few stud-

ies to address the case of non-uniform strain estimation using only the amplitude of the FBG reflection spectrum. Such studies either try to reconstruct the whole strain distribution along the FBG length, or to retrieve certain statistics from the strain field. As examples of the studies from the latter category, Ling et al. tried to incorporate finite element modelling results into the transfer matrix model of the FBG sensor in order to estimate the average strain along the FBG length in a three point bending test setup [32]. In [33] the maximum value of the axial strain field was estimated using an iterative minimisation approach including results from the finite element modelling and the transfer matrix model for the FBG sensor. In Chapters 3 and 4 alternative analytical methods will be presented, using which the average of the non-uniform axial strain fields can be calculated.

In the studies of the first category there has been some research focusing on the reconstruction of the whole strain field based on the amplitude of the FBG reflection spectrum without having the phase information. Most of such studies try to reconstruct the strain field by considering a limited number of segments for the transfer matrix model and applying optimisation algorithms such as genetic algorithms to minimise the amplitude difference between the calculated and the measured reflection spectrum [34, 35]. Within this framework, it is claimed these reconstructed strain distributions yield in normalised reflection spectra with root mean squares of less than 0.04 within a few hundreds of a second [35]. However, the biggest problem with such methods is their unreliability and ambiguousness. Firstly, these methods are highly sensitive to non-axial strain components and imperfections in the FBG production and interrogation, which can easily alter the reconstructed strain field results. Secondly, by ignoring the phase information the reconstructed strain field will have a reflection line of symmetry ambiguity. Because of these reasons, studies of this kind will not be further discussed in this thesis.

2.4. DAMAGE DETECTION USING FBG SENSORS

As presented in the block diagram of Fig. 1.7, one of the research areas related to damage detection in composites is related to impact localisation and detection where the dynamic response of FBG sensors to impact damages are taken into account. In such studies, usually a few number of FBG sensors are incorporated into the structure under investigation at certain orientations and distances from each other. At the moment of impact their peak wavelength is recorded, using which the location of the impact and its severity is assessed. In [36], Coelho et al. showed that by recording the dynamic strain values of several equidistant FBG sensors (cases of two and five sensors were investigated in the paper) and by comparing the transient maximum strain value at each FBG sensor the location of the impact can be determined. Shrestha et al. [37] followed a similar approach based on multiple equidistant FBG sensors and some reference FBG recordings from prior known impacts. Then, the test impact responses of the FBG sensors were compared with the reference signals, and from the differences between the two signals the location of the impact was inferred. In [38] and [39], the dynamic response of FBG sensors (their peak wavelength) was recorded with a high temporal resolution (with microsecond resolution), using several FBG sensors surface mounted on a composite plate. Taking into account the time of arrival of the vibrations resulted from the impact and the difference in the velocity of the propagating waves along different directions in the composite material the localisation of the impacts was carried out. These are only a few examples of such studies, and other different approaches of this kind

can also be found in the literature, including, the use of machine learning and regression methods in impact localisation [39], and Lamb wave sensing with FBG sensors [40].

In another group of studies the static response of FBG sensors to damage is analysed and the type and the extent of the damage is investigated. In this group of studies the main advantage is the possibility of damage assessment after its occurrence and high frequency dynamic measurements are not required. However, since FBG sensors are only locally sensitive to static defects, the damaged area and the resulting non-uniform strain field has to reach the length of the sensor in order to be recognised. Considering the small size of FBG sensors and their high cost, this limitation makes static damage identification in large composites almost impractical. However, due to the high spatial resolution of these methods and their accuracy, FBG sensors can be suitable candidates for the study of composite structures and the assessment of the propagation of defects in them. As examples of such studies, Okabe et al. showed that there is a relationship between the density of matrix cracks in the internal layers of composites and the full width at quarter maximum (FWQM) of the embedded FBG reflection spectra in contact with the cracks [41]. In [42] the extent and the direction of delamination type damages in laminated composites were assessed using chirped FBG sensors. In [42] delamination type damages resulting from low-velocity impacts were assessed under different energy release levels. As a final example, Riccio et al. used FBG sensors for the monitoring of skin buckling in stiffened composite panels [43]. Most of the studies of this category focus on analysing the morphology of the full FBG reflection spectrum, and the fact that under the non-uniform strain field of the damaged composite the reflection spectrum broadens. An example of this phenomenon is shown in Fig. 2.3. While these changes in the morphology of the FBG reflection spectra take place during sharp non-uniform strain fields of the damaged area they are not necessarily an indication of damage. Later, in Chapter 7, it will be shown that the broadening of the reflection spectrum can be attributed to other effects and it is not always the result of a damaged composite. In this thesis, the focus will be on using FBG sensors for damage detection under static conditions, and offering reliable assessments of the damage state in composites.

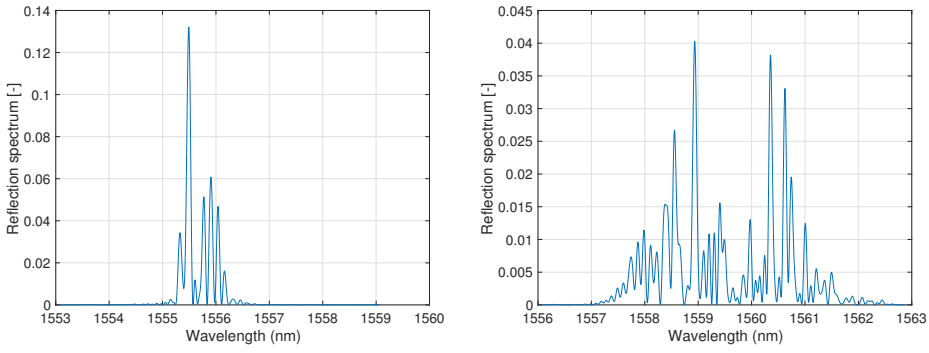

(a) (b)

Figure 2.3: (a): The reflection spectrum from an embedded FBG sensor in contact with 2 transverse matrix cracks. (b): The reflection spectrum from an embedded FBG sensor in contact with 6 transverse cracks.

2.5. CONTINUOUS STRAIN FIELD RECONSTRUCTION AND DAMAGE DETECTION WITH FBG SENSORS

Until now, in all the applications given in this chapter, it was assumed that only the amplitude of the FBG reflection spectrum was available, and as mentioned in the previous chapters, the reconstruction of the continuous (or also called distributed) strain field using only the amplitude of the FBG reflection spectrum does not offer reliable results. However, there are some interrogation techniques that can be used to measure the complex reflection spectrum. One of the most robust measurement techniques capable of recording the complex reflection spectrum is called optical low-coherence reflectometry or OLCR. In this technique, a low coherence length light source (for example an LED with a coherence length of around 10 μm) is used, along with a moving mirror (reference arm) and an FBG (test arm) in a Michelson interferometer setup [44]. Due to the low coherence length of the LED light source, the input light to the FBG will interfere with the light in the reference arm that has travelled the same distance (adjusted by moving the mirror), thus, resulting in a position dependent interrogation of the FBG [45]. Fig. 2.4 depicts a simplified schematic of the OLCR setup.

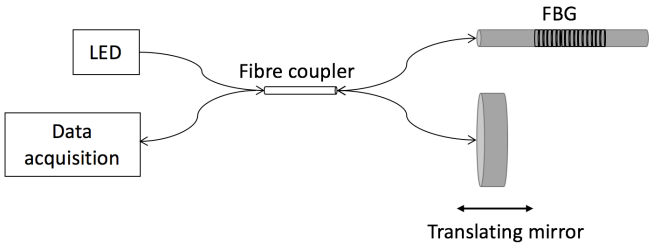

Figure 2.4: The OLCR setup, where by moving the translating mirror and using a low-coherence optical source spatially modulated coupling coefficients along the FBG length can be retrieved.

The resulting signal, which is the convolution of the complex impulse response of the optical source and the sensor, is then input to an inverse-scattering algorithm that retrieves both the amplitude and the phase of the local coupling coefficients along the FBG length [46]. The local Bragg wavelengths and consequently the local strain values are thus calculated (using methods such as the discrete layer peeling method described in [47]).

Using this technique, there have been some studies in which the axial strain field along the FBG sensor in contact with damages in composites have been characterised. In [48] and [49] the application of distributed non-uniform estimation in delamination growth monitoring in composites was investigated. It was shown that the delamination tip (which was considered to be the inflection point of the strain distribution along the FBG length) can be accurately estimated. With that, an online monitoring scheme for monitoring of the delamination growth in composites was presented. The upper limit of for the spatial resolution of these methods is the translation step size of the moving mirror, which could range from a few micrometers to a few millimetres. In another work, the non-uniform strain field along the FBG length embedded between composite layers was estimated [50], and in [51], the residual stresses in cured composites were estimated.

Although the above mentioned techniques have a good potential for the study of composites and the non-uniform strain fields within them they have some shortcomings. Firstly, the strain reconstruction algorithms are sensitive to birefringence effects and transverse loads. To overcome this, some methods have been proposed to adapt the OLCR system for polarisation sensitive measurements by incorporating a polarisation controller into the setup and manually adjusting its alignment with the input light [52]. However, this approach, as well as the standard OLCR technique itself, suffer from high computational complexity and a relatively slow interrogation speed. The other problem with the current OLCR setup is the multiplexing limitation and the time-consuming process of the initial adjustment of the setup to make the reference and the test arms equal in length.

Due to these practical issues, this thesis will focus on developing algorithms for damage identification using only the amplitude of the reflection spectrum and real-time evaluation of the damage state in composites. This real-time monitoring of the damage state also creates a platform for the analysis of the transient response of the composite material to different load scenarios and damage types. In the coming chapters, these approaches and applications will be discussed in more detail.

2.6. EMBEDDING FBG SENSORS INSIDE COMPOSITES

Embedding optical fibres between the layers of composite laminates raises some concerns regarding the structural integrity of the host material. For this reason there has been several papers in the literature that studied the behaviour of the composite with embedded optical fibres both experimentally and theoretically. In one of the earliest works on this subject, Eaton et al. used finite element modelling to show that at the interface of the optical fibre and the host material there will be a high stress concentration that might affect the structural integrity of the composite [53]. In another study published in the same year, Lee et al. used finite element modelling and experimental measurements to show that under static loads, embedding optical fibres between composite layers has a small effect on the stiffness and the strength of the composite. However, the fatigue life of the composite material is adversely affected by the embedded optical fibre [54]. In [55], Surgeon et al. reported that the embedding of the optical fibre between the composite layers has an insignificant effect on the fatigue life and the performance of the host unidirectional composite material. As seen from these examples, some of the results are rather contradictory. However, the general tendency is that when the embedded optical fibre ares in the same direction as the reinforcement fibres in the host material the degradation of the composite is insignificant [56]. Further, there has been some studies with the use of small diameter optical fibres, such as 40 μm diameter [57] to minimise this degradation.

Another factor that should be taken into account is the health of the optical fibre sensor itself, especially at the ingress and egress points of the composite material. In [58] Kinet et al. reviewed some methods to protect the optical fibre at the ingress points including a method with the use of teflon tubes [59], and another method with especially designed embedded connectors [60]. This topic is beyond the scope of this thesis, and will not be further discussed here.

2.7. CONCLUDING REMARKS

From the previous sections, it is evident that FBG sensors have diverse applications in structural health monitoring, ranging from point strain estimation to damage detection and identification. However, there are some practical limitations associated with them that itself has given rise to several studies. The embedding process, the interrogation system, the non-axial strain components and birefringence effects, and the cross sensitivity of the sensor to different physical parameters are a few examples of such issues. In this chapter, some examples from literature were mentioned and some solutions to these issues were discussed along with the potential and the limitations of each study. Due to the extent of these subjects this thesis will only focus on improving the accuracy and the spatial resolution of structural health monitoring methods using FBG sensors, with a focus on simplicity of the implementation of the test setup and algorithms that can run in real-time for online monitoring of the damage state with high frequencies. Considering the discussions of this chapter, this thesis will therefore focus on extracting information on the damage state and retrieving statistics from the strain field along the FBG length, given only the magnitude of the reflection spectrum. In the coming chapters, these applications and algorithms will be discussed in detail and their results and potentials will be compared with the state-of-the-art methods.

REFERENCES

[1] W. W. Morey, G. Meltz, W. H. Glenn, "Fiber optic Bragg grating sensors," *Fiber Optic and Laser Sensors VII*, vol. 1169, pp. 98-107, 1990.

[2] C. E. Campanella, A. Cuccovillo, C. Campanella, A. Yurt, V. Passaro, "Fibre Bragg grating based strain sensors: review of technology and applications," *Sensors*, vol. 18, no. 9, pp. 3115, 2018.

[3] L. Dong, J. L. Archambault, L. Reekie, P. J. Russell, D. N. Payne, "Single pulse Bragg gratings written during fibre drawing," *Electronics Letters*, vol. 29, no. 17, pp. 1577-1578, 1993.

[4] G. C. Kahandawa, J. Epaarachchi, H. Wang, K. T. Lau, "Use of FBG sensors for SHM in aerospace structures," *Photonic Sensors*, vol. 2, no. 3, pp. 203-214, 2012.

[5] D. C. Betz, W. J. Staszewski, G. Thursby, B. Culshaw, "Multi-functional fibre Bragg grating sensors for fatigue crack detection in metallic structures," *Proceedings of the Institution of Mechanical Engineers, Part G: Journal of Aerospace Engineering*, vol. 220, no. 5, pp. 453-461, 2006.

[6] M. Ussorio, H. Wang, S. L. Ogin, A. M. Thorne, G. T. Reed, S. C. Tjin, R. Suresh, "Modifications to FBG sensor spectra due to matrix cracking in a GFRP composite," *Construction and Building Materials*, vol. 20, no. 1, pp. 111-118, 2006.

[7] J. Mao, J. Chen, L. Cui, W. Jin, C. Xu, Y. He, "Monitoring the corrosion process of reinforced concrete using BOTDA and FBG sensors," *Sensors*, vol. 15, no. 4, pp. 8866-8883, 2015.

[8] A. D. Kersey, M. A. Davis, H. J. Patrick, M. LeBlanc, K. Koo, C. Askins, M. Putnam, and E. J. Friebele, "Fiber grating sensors," *Journal of Lightwave Technology*, vol. 15, no. 8, pp. 1442-1463, 1997.

[9] G. M. H. Flockhart, R. R. J. Maier, J. S Barton, W. N. MacPherson, J. D. C. Jones, K. E. Chisholm, L. Zhang, I. Bennion, I. Read, P. D. Foote, "Quadratic behavior of fiber Bragg grating temperature coefficients," *Applied optics*, vol. 43, no. 13, pp. 2744-2751, 2004.

[10] J. S. Sirkis, "Unified approach to phase-strain-temperature models for smart structure interferometric optical fiber sensors: part 1, development," *Optical Engineering*, vol. 32, no. 4, 1993.

[11] Z. Zhang, C. Tian, M. R. Mokhtar, P. Petropoulos, D. J. Richardson, M. Ibsen, "Rapidly reconfigurable optical phase encoder-decoders based on fiber Bragg gratings," *IEEE Photonics Technology Letters*, vol. 18, no. 11, pp. 1216-1218, 2006.

[12] Y. Wang, B. Yun, N. Chen, Y. Cui, "Characterization of a high birefringence fibre Bragg grating sensor subjected to non-homogeneous transverse strain fields," *Measurement Science and Technology*, vol. 17, no. 4, pp. 939, 2006.

[13] R. Gafsi, M. A. El-Sherif, "Analysis of induced-birefringence effects on fiber Bragg gratings," *Optical Fiber Technology*, vol. 6, no. 3, pp. 299-323, 2000.

[14] R. Montanini, L. d'Acquisto, "Simultaneous measurement of temperature and strain in glass fiber/epoxy composites by embedded fiber optic sensors: I. Cure monitoring," *Smart Materials and Structures*, vol. 16, no. 5, pp. 1718, 2007.

[15] M. Sudo, M. Nakai, K. Himeno, S. Suzaki, A. Wada, R. Yamauchi, "Simultaneous measurement of temperature and strain using PANDA fiber grating," *Optical Fiber Technology*, vol. 6, no. 3, 1997.

[16] S. T. Oh, W. T. Han, U. C. Paek, Y. Chung, "Discrimination of temperature and strain with a single FBG based on the birefringence effect," *Optics Express*, vol. 12, no. 4, pp. 724-729, 2004.

[17] J. Chen, Q. Liu, Z. He, "High-Resolution Simultaneous Measurement of Strain and Temperature Using π-Phase-Shifted FBG in Polarization Maintaining Fiber," *Journal of Lightwave Technology*, vol. 35, no. 22, pp. 4838-4844, 2017.

[18] C. G. Askins, M. A. Putnam, E. J. Friebele, "Instrumentation for interrogating many-element fiber Bragg grating arrays," *Smart Structures and Materials 1995: Smart Sensing, Processing, and Instrumentation*, vol. 2444, pp. 257-266, 1995.

[19] H. W. Lee, H. J. Park, J. H. Lee, M. Song, "Accuracy improvement in peak positioning of spectrally distorted fiber Bragg grating sensors by Gaussian curve fitting," *Applied Optics*, vol. 46, no. 12, pp. 2205-2208, 2007.

[20] L. Negri, A. Nied, H. Kalinowski, A. Paterno, "Benchmark for peak detection algorithms in fiber Bragg grating interrogation and a new neural network for its performance improvement," *Sensors*, vol. 11, no. 4, pp. 3466-3482, 2011.

[21] M. De Sousa, J. Costa, R. De Souza, R. Pantoja, "FBG optimization using spline encoded evolution strategy," *Journal of Microwaves, Optoelectronics and Electromagnetic Applications*, vol. 10, no. 1, pp. 165-178, 2011.

[22] J. Gong, J. MacAlpine, C. Chan, W. Jin, M. Zhang, Y. Liao, "A novel wavelength detection technique for fiber Bragg grating sensors," *IEEE Photonics Technology Letters*, vol. 14, no. 5, pp. 678-680, 2002.

[23] D. Tosi, M. Olivero, G. Perrone, "Performance analysis of peak tracking techniques for fiber Bragg grating interrogation systems," *Journal of Microwaves, Optoelectronics and Electromagnetic Applications*, vol. 11, no. 2, pp. 252-262, 2012.

[24] A. Lamberti, S. Vanlanduit, B. De Pauw, F. Berghmans, "Peak detection in fiber Bragg grating using a fast phase correlation algorithm," *Optical Sensing and Detection III*, pp. 9141, 2014.

[25] W. Zhaoxia, Y. Haili, "Fiber Bragg grating peak wavelength detection technique based on wavelet analysis," *International Conference on Internet Computing and Information Services*, pp. 462-464, 2011.

[26] D. Tosi, "KLT-based algorithm for sub-picometer accurate FBG tracking with coarse wavelength sampling," *IEEE Photonics Technology Letters*, vol. 27, no. 20, pp. 2134-2137, 2015.

[27] D. Tosi, "Review and analysis of peak tracking techniques for fiber Bragg grating sensors," *Sensors*, vol. 17, no. 10, pp. 2368, 2017.

[28] C. W. Smelser, S. J. Mihailov, D. Grobnic, "Rouard's method modeling of type I-IR fiber Bragg gratings made using an ultrafast IR laser and a phase mask," *JOSA B*, vol. 23, no. 10, pp. 2011-2017, 2006.

[29] J. Bae, J. Chun, S. B. Lee, "Analysis of the fiber Bragg gratings using the lattice filter model," *Japanese Journal of Applied Physics*, vol. 39, no. 4R, pp. 1752, 2000.

[30] T. Erdogan, "Fiber grating spectra," *Journal of Lightwave Technology*, vol. 15, no. 8, pp. 1277-1294, 1997.

[31] R. Kashyap, "Fiber bragg gratings," *Academic Press*, 2009.

[32] H. Ling, K. Lau, L. Cheng, K. Chow, "Embedded fibre Bragg grating sensors for non-uniform strain sensing in composite structures," *Measurement Science and Technology*, vol. 16, no. 12, pp. 2415, 2005.

[33] P. Kisała, "Measurement of the maximum value of non-uniform strain using a temperature-insensitive fibre Bragg grating method," *Opto-electronics Review*, vol. 21, no. 3, pp. 293-302, 2013.

[34] R. Zhang, S. Zheng, Y. Xia, "Strain profile reconstruction of fiber Bragg grating with gradient using chaos genetic algorithm and modified transfer matrix formulation," *Optics Communications*, vol. 281, no. 13, pp. 3476-3485, 2008.

[35] H. Cheng, C. Yen, Y. Xiao, "Measurement of Arbitrary Strain Profiles of Fiber Bragg Gratings in Fabry-Perot-like Transmission Spectra Using a Real-Coded Genetic Algorithm," *Sensors and Materials*, vol. 26, no. 5, pp. 299-306, 2014.

[36] C. Coelho, Clyde C. Hiche, A. Chattopadhyay, "Impact localization and force estimation on a composite wing using fiber bragg gratings sensors," *51st AIAA/ASME/ASCE/AHS/ASC Structures, Structural Dynamics, and Materials Conference 18th AIAA/ASME/AHS Adaptive Structures Conference 12th*, pp. 2905, 2010.

[37] P. Shrestha, J. Kim, Y. Park, C. Kim, "Impact localization on composite structure using FBG sensors and novel impact localization technique based on error outliers," *Composite Structures*, vol. 142, pp. 263-271, 2016.

[38] J. Frieden, J. Cugnoni, J. Botsis, T. Gmür, "Low energy impact damage monitoring of composites using dynamic strain signals from FBG sensors–Part I: Impact detection and localization," *Composite Structures*, vol. 94, no. 2, pp. 438-445, 2012.

[39] E. Kirkby, R. De Oliveira, V. Michaud, J. A. Månson, "Impact localisation with FBG for a self-healing carbon fibre composite structure," *Composite Structures*, vol. 94, no. 1, pp. 8-14, 2011.

[40] Z. Tian, L. Yu, X. Sun, B. Lin, "Damage localization with fiber Bragg grating Lamb wave sensing through adaptive phased array imaging," *Structural Health Monitoring*, vol. 18, no. 1, pp. 334-344, 2019.

[41] Y. Okabe, T. Mizutani, S. Yashiro, N. Takeda, "Detection of microscopic damages in composite laminates," *Composites Science and Technology*, vol. 62, no. 7, pp. 951-958, 2002.

[42] S. Takeda, Y. Okabe, N. Takeda, "Monitoring of delamination growth in CFRP laminates using chirped FBG sensors," *Journal of Intelligent Material Systems and Structures*, vol. 19, no. 4, pp. 437-444, 2008.

[43] A. Riccio, F. Di Caprio, F. Camerlingo, F. Scaramuzzino, B. Gambino, "Positioning of embedded optical fibres sensors for the monitoring of buckling in stiffened composite panels," *Applied Composite Materials*, vol. 20, no. 1, pp. 73-86, 2013.

[44] P. Giaccari, P. Dunkel, R. Gabriel, L. Humbert, J. Botsis, H. G. Limberger, R. P. Salathé, "On a direct determination of non-uniform internal strain fields using fibre Bragg gratings," *Smart Materials and Structures*, vol. 14, no. 1, pp. 127, 2004.

[45] P. Giaccari, "Fiber Bragg grating characterization by optical low coherence reflectometry and sensing applications," *Doctoral dissertation*, EPFL, 2003.

[46] J. Skaar, O. H. Waagaard, "Design and characterization of finite-length fiber gratings," *IEEE Journal of Quantum Electronics*, vol. 39, no. 10, pp. 1238-1245, 2003.

[47] J. Skaar, L. Wang, T. Erdogan, "On the synthesis of fiber Bragg gratings by layer peeling," *IEEE Journal of Quantum Electronics*, vol. 37, no. 2, pp. 165-173, 2001.

[48] L. Sorensen, J. Botsis, T. Gmür, J. Cugnoni, "Delamination detection and characterisation of bridging tractions using long FBG optical sensors," *Composites Part A: Applied Science and Manufacturing*, vol. 38, no. 10, pp. 2087-2096, 2007.

[49] D. Sans, S. Stutz, J. Renart, J. A. Mayugo, J. Botsis, "Crack tip identification with long FBG sensors in mixed-mode delamination," *Composites Structures*, vol. 94, no. 9, pp. 2879-2887, 2012.

[50] J. Botsis, L. Humbert, F. Colpo, P. Giaccari, "Embedded fiber Bragg grating sensor for internal strain measurements in polymeric materials," *Optics and Lasers in Engineering*, vol. 43, no. 3, pp. 491-510, 2005.

[51] F. Colpo, L. Humbert, J. Botsis, "Characterisation of residual stresses in a single fibre composite with FBG sensor," *Composites Science and Technology*, vol. 67, no. 9, pp. 1830-1841, 2007.

[52] L. Sorensen, "The response of embedded FBG sensors to non-uniform strains in CFRP composites during processing and delamination," *Doctoral dissertation*, EPFL, 2007.

[53] N. C. Eaton, R. C. Drew, H. Geiger, "Finite element stress and strain analysis in composites with embedded optical fiber sensors," *Smart Materials and Structures*, vol. 4, no. 2, pp. 113, 1995.

[54] D. C. Lee, J. J. Lee, S. J. Yun, "The mechanical characteristics of smart composite structures with embedded optical fiber sensors," *Composite Structures*, vol. 32, no. 1, pp. 39-50, 1995.

[55] M. Surgeon, M. Wevers, "Static and dynamic testing of a quasi-isotropic composite with embedded optical fibres," *Composites Part A: Applied Science and Manufacturing*, vol. 30, no. 3, pp. 317-324, 1999.

[56] D. W. Jensen, J. Pascual, J. A. August, "Performance of graphite/bismaleimide laminates with embedded optical fibers. I. Uniaxial tension," *Smart Materials and Structures*, vol. 1, no. 1, pp. 24, 1992.

[57] S. Takeda, S. Minakuchi, Y. Okabe, N. Takeda, "Delamination monitoring of laminated composites subjected to low-velocity impact using small-diameter FBG sensors," *Composites Part A: Applied Science and Manufacturing*, vol. 36, no. 7, pp. 903-908, 2005.

[58] D. Kinet, P. Mégret, K. W. Goossen, L. Qiu, D. Heider, C. Caucheteur, "Fiber Bragg grating sensors toward structural health monitoring in composite materials: Challenges and solutions," *Sensors*, vol. 14, no. 4, pp. 7394-7419, 2014.

[59] G. Luyckx, D. Kinet, N. Lammens, K. Chah, C. Caucheteur, P. Mégret, J. Degrieck, "Temperature insensitive cure cycle monitoring of cross-ply composite laminates using the polarization dependent loss property of FBG," *15th European Conference on Composite Materials*, 2012.

[60] D. Kinet, B. Guerra, D. Garray, C. Caucheteur, P. Mégret, “Weakly intrusive optical fibre connector for composite materials applications: vibration and temperature validation tests,” *Fifth European Workshop on Optical Fibre Sensors*, pp. 8794, 2013.

3

Calculation of the Mean Strain of Smooth Non-uniform Strain Fields Using Conventional FBG Sensors

Being alone never felt right.
Sometimes it felt good, but it never felt right.

Charles Bukowski, Women

In the past few decades, fibre Bragg grating (FBG) sensors have gained a lot of attention in the field of distributed point strain measurement. One of the most interesting properties of these sensors is the presumed linear relationship between the strain and the peak wavelength shift of the FBG reflected spectra. However, subjecting sensors to a non-uniform stress field will in general result in a strain estimation error when using this linear relationship. In this chapter a new strain estimation algorithm will be proposed that accurately estimates the mean strain value in the case of smooth non-uniform strain distributions. To do so, first an approximation of the classical transfer matrix model will be presented, which will be referred to as the approximated transfer matrix model (ATMM). This model facilitates the analysis of FBG reflected spectra under arbitrary strain distributions, particularly by providing a closed-form approximation of the side-lobes of the reflected spectra. Based on this new formulation, a maximum likelihood estimator of the mean strain value will

This chapter is published as "Calculation of the mean strain of smooth non-uniform strain fields using conventional FBG sensors", by A. Rajabzadeh, R. Heusdens, R. C. Hendriks, and R. M. Groves, in IEEE/OSA Journal of Lightwave Technology, vol. 36, no. 17, pp. 3716-3725, 2018.

be derived. The algorithm is validated using both computer simulations and experimental FBG measurements. Compared to state-of-the-art methods, which typically introduce errors of tens of microstrains, the proposed method is able to compensate for this error. In the typical examples that were analysed in this study, mean strain errors of around 60$\mu\varepsilon$ were compensated.

3.1. INTRODUCTION

Fibre Bragg grating (FBG) sensors have been shown to be one of the most robust and versatile sensors in strain sensing applications. With the possibility of multiplexing several sensors on a single optical fibre and their immunity to electromagnetic interferences, FBG sensors are an ideal candidate for applications in adverse environments such as the oil and gas industries or aviation [1]. Because of their small diameter, they can be embedded inside composite structures to acquire internal strain measurements [2, 3] and can also be used for damage detection purposes including delamination and matrix cracks [4–7]. In addition, strain (or temperature) changes along the length of the sensor are directly related to the peak wavelength shift of the reflected spectra of FBG sensors (the intensity of the reflected light), making strain measurements straightforward. This relationship was described in detail in Section 2.1. However, FBG sensors have several complications which need to be addressed properly. The first problem is that the strain and temperature jointly contribute to the peak wavelength shift. This problem was discussed in detail in Chapter 2.

The second problem with FBG strain measurements is the sensor response under non-uniform strain distributions. Under uniform strain distributions, the relationship between the strain and the peak wavelength shift of the FBG reflection spectrum is linear. However, this does not necessarily hold under non-uniform strain distributions. Such non-uniformities could be the result of embedding the sensor in or surface mounting on a structure, when a non-uniform stress is applied. For instance, an embedded FBG sensor in a composite structure in the vicinity of a crack or delamination defect experiences different non-uniform strain distributions and, therefore, responds with rather distinguishable reflected spectra [5–9]. The resulting non-uniform strain distributions under these circumstances could most possibly complicate strain measurements using FBG sensors.

Despite the fact that in many practical situations the strain distribution is non-uniform, existing algorithms for estimating the mean strain value are still based on the shift of the peak wavelength. When the sensor is subject to non-uniform strain fields, however, each segment of the sensor will experience a different strain, resulting in different peak wavelength shifts along the length of the sensor. As a consequence, looking to the (global) shift of the peak wavelength will in general lead to an estimation error in the mean strain value. In this chapter, a new algorithm will be proposed that accurately estimates the mean strain value when the strain distribution is non-uniform. It will be shown that the mean strain value is related to the average shift of the peak wavelength along the length of the sensor and that this information can be found in the side lobes of the reflected spectra. In order to analyse the reflected spectra a model will be presented that describes the interaction of the forward and backward electric wave propagation between consecutive segments, which is an approximation of the widely used transfer matrix model (TMM). This approximated transfer matrix model (ATMM) enables us to accurately find the average wavelength shift. The codes for the approximated transfer matrix model and the mean strain estimation algo-

rithm can be accessed online[1].

3.2. BACKGROUND

FBG sensors are spatially modulated patterns of refractive index changes in the core of optical fibres that act as a mirror for certain wavelengths. The linear relationship between the peak wavelength of the reflected spectra, usually referred to as the Bragg wavelength and denoted by λ_B, and the grating period Λ of the FBG is given by [10, 11]

$$\lambda_B = 2n_{\text{eff}}\Lambda,$$

where n_{eff} is the effective refractive index of the core. Under uniform strain (or temperature) fields, say s, the change in the grating period is constant along the length of the sensor, resulting in a shift $\Delta\lambda_B$ of the Bragg wavelength. That is,

$$\Delta\lambda_B = k_s s, \tag{3.1}$$

where the constant k_s depends on the physical properties of the sensor[2]. In theory, this is without any change in the morphology of the reflected spectra, and the peaks will either be shifted towards shorter wavelengths (under compression) or longer wavelengths (under tension). Therefore, under a uniform strain field, Eq. (3.1) results in an accurate measurement of the mean strain value over the length of the sensor. However, perfect uniform strain distributions are unlikely in practice. The more common strain fields are non-uniform and result in nontrivial overall reflected spectra, possibly asymmetric and having multiple peaks, leading to an error in the mean strain estimation. In order to compensate for this error, the full spectrum of the signal should be analysed, for which the transfer matrix method has been shown to be a proper tool.

3.2.1. TRANSFER MATRIX MODEL

Consider the case of a non-uniform strain distribution over the length of the FBG sensor. The length of the sensor will be divided into a series of small virtual segments of length Δz, where Δz is taken sufficiently small such that each of these segments has approximately a uniform strain distribution. As a consequence, the strain distribution will affect each segment's grating period differently. To be more precise, let s_i denote the strain field of segment i. The Bragg wavelength shift $\Delta\lambda_{B_i}$ of segment i is then given by

$$\Delta\lambda_{B_i} = \lambda_{B_i} - \lambda_B = k_s s_i,$$

where λ_{B_i} is the Bragg wavelength of segment i. As a consequence, the mean strain distribution, denoted by $\bar{s}$, satisfies

$$k_s \bar{s} = \bar{\lambda}_B - \lambda_B, \tag{3.2}$$

where $\bar{\lambda}_B = \frac{1}{M}\sum_i \lambda_{B_i}$ is the mean Bragg wavelength of the sensor. Hence, when the sensor is subject to non-uniform strain fields, each segment of the model experiences a different Bragg wavelength shift and $\bar{\lambda}_B$ does not necessarily correspond to the peak wavelength anymore.

[1] http://cas.tudelft.nl/Repository/

[2] For the sensors used in this study, based on the datasheet, $k_s = 1.209 \times 10^{-3}\text{nm}/\mu\varepsilon$.

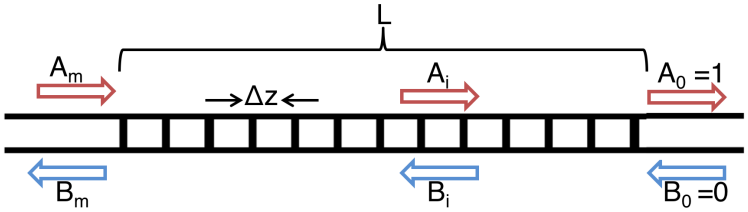

Figure 3.1: Schematic view of the FBG structure.

In order to analyse the FBG reflected spectra under an arbitrary grating distribution, the transfer matrix model (TMM) will be used [12]. The TMM models the interaction of the forward and backward electric wave propagation between consecutive segments, where it is assumed that the length of the individual segments Δz satisfies $\Delta z \gg \Lambda$. Let A_i and B_i denote the forward and backward propagating waves in segment i, respectively (see Fig. 3.1). In this model, it is assumed that at the end of the final segment, there will be a full transmission of the incident wave ($A_0 = 1$) and no reflection from further along the optical fibre ($B_0 = 0$).

In Section 2.2 the relation between the forward and the backward propagating waves between each two segments of this model was described in detail, and the transfer matrices that described this relation were presented as

$$F_i = \begin{pmatrix} \cosh(\gamma_i \Delta z) - j\frac{\Delta\beta_i}{\gamma_i}\sinh(\gamma_i \Delta z) & -j\frac{\kappa_i}{\gamma_i}\sinh(\gamma_i \Delta z) \\ j\frac{\kappa_i}{\gamma_i}\sinh(\gamma_i \Delta z) & \cosh(\gamma_i \Delta z) + j\frac{\Delta\beta_i}{\gamma_i}\sinh(\gamma_i \Delta z) \end{pmatrix}. \tag{3.3}$$

In Eq. (3.3), κ_i is the coupling coefficient between forward and backward waves, $\Delta\beta_i = 2\pi n_{\text{eff}}(\frac{1}{\lambda} - \frac{1}{\lambda_{\text{B}_i}})$ is the difference between the propagation constants in the longitudinal (or z) direction, $\gamma_i = \sqrt{\kappa_i^2 - \Delta\beta_i^2}$, and λ is a given wavelength under investigation. Here, it is assumed that the total number of segments considered in the model is M. In the next section, an approximation of the transfer matrix model will be introduced which significantly simplifies the analysis of FBG reflected spectra.

3.3. APPROXIMATED TRANSFER MATRIX MODEL

In this section it will be shown that, for sufficiently small Δz, the TMM can be accurately approximated, resulting in a model that facilitates the analysis of non-uniform strain fields. This approximated model will be referred to as the approximated transfer matrix model (ATMM). Note that the length Δz can be chosen to be arbitrarily small (as long as $\Delta z \gg \Lambda$) and that this choice has no effect on the physical properties of the sensor.

Suppose that Δz is sufficiently small. We will show that in this case the matrix F_i can be approximated as

$$F_i \approx \begin{pmatrix} e^{-j\Delta\beta_i \Delta z} & -j\kappa_i \Delta z \,\text{sinc}(\Delta\beta_i \Delta z) \\ j\kappa_i \Delta z \,\text{sinc}(\Delta\beta_i \Delta z) & e^{j\Delta\beta_i \Delta z} \end{pmatrix}, \tag{3.4}$$

where $\text{sinc}(\cdot) = \frac{\sin(\cdot)}{(\cdot)}$.

To show under what conditions the approximations hold, an element-wise comparison will be made between the formulations in Eq. (3.3) and Eq. (3.4). Recall that $\Delta\beta_i = 2\pi n_{\text{eff}}(\frac{1}{\lambda} - \frac{1}{\lambda_{B_i}})$ and $\gamma_i = \sqrt{\kappa_i^2 - \Delta\beta_i^2}$, where λ_{B_i} is the Bragg wavelength of segment i. In the near infrared wavelength range, which is the region of interest for almost all FBG sensors, we have ${\Delta\beta_i}^2 \gg {\kappa_i}^2$, and thus $\gamma_i \approx j|\Delta\beta_i|$, except for a small wavelength range centred around λ_{B_i} (a few tens of picometres which depends on the production and reflectivity levels of the FBG sensor) where the values of κ_i and $\Delta\beta_i$ are of the same order of magnitude. In order to make the analysis of the formulation easier, the wavelength range will be divided into the two above mentioned regions, as different strategies are needed to verify the correctness of the approximation for these regions.

Region 1: In this region $|\Delta\beta_i| \gg \kappa_i$. As already mentioned, for this region $\gamma_i \approx j|\Delta\beta_i|$, and therefore, the first term of $F_{i_{11}}$ in Eq. (3.3), i.e., $\cosh(\gamma_i \Delta z)$, can be approximated as

$$\cosh(\gamma_i \Delta z) \approx \cosh(j|\Delta\beta_i|\Delta z) = \cos(\Delta\beta_i \Delta z),$$

where the absolute value is omitted since cos is an even-symmetric function. The second term of $F_{i_{11}}$ in Eq. (3.3) can in this wavelength region be approximated as

$$-j\frac{\Delta\beta_i}{\gamma_i}\sinh(\gamma_i \Delta z) \approx -\text{sign}(\Delta\beta_i)\sinh(j|\Delta\beta_i|\Delta z) = -j\sin(\Delta\beta_i \Delta z),$$

where the absolute value is omitted since sin is an odd-symmetric function. Combining these relations gives the required result for $F_{i_{11}}$ in Eq. (3.4). The remaining term ($F_{i_{21}}$) can in this wavelength region be approximated as

$$j\frac{\kappa_i}{\gamma_i}\sinh(\gamma_i \Delta z) \approx j\frac{\kappa_i}{|\Delta\beta_i|}\sin(|\Delta\beta_i|\Delta z) = j\kappa_i \Delta z\,\text{sinc}(\Delta\beta_i \Delta z).$$

Region 2: In this wavelength range, the values of κ_i and $\Delta\beta_i$ are of the same order of magnitude so that $|\gamma_i \Delta z| \ll 1$. Hence, the Taylor series expansion for the first term of $F_{i_{11}}$ in Eq. (3.3) will be

$$\cosh(\gamma_i \Delta z) = 1 + \frac{1}{2}|\gamma_i \Delta z|^2 + \frac{1}{4!}|\gamma_i \Delta z|^4 + \cdots.$$

In order to keep the representation of the F_i matrices consistent in both regions, $\cosh(\gamma_i \Delta z)$ is replaced by $\cos(\Delta\beta_i \Delta z)$, which leads in Region 2 to an absolute error of

$$\begin{aligned} &|\cosh(\gamma_i \Delta z) - \cos(\Delta\beta_i \Delta z)| \\ &= \frac{1}{2}\Delta z^2\left(|\Delta\beta_i|^2 + |\gamma_i|^2\right) + \frac{1}{6!}\Delta z^6\left(|\Delta\beta_i|^6 + |\gamma_i|^6\right) + \cdots, \end{aligned} \tag{3.5}$$

which is negligible when Δz is sufficiently small[3]. Along the same lines and using the Taylor series expansion of sin and sinh, the second term of $F_{i_{11}}$ is approximated as

$$j\frac{\Delta\beta_i}{\gamma_i}\sinh(\gamma_i \Delta z) \approx j\frac{\Delta\beta_i}{\gamma_i}(\gamma_i \Delta z) \approx j\sin(\Delta\beta_i \Delta z).$$

[3] In this study, using computer simulations, it was seen that for $\Delta z \leq 0.001$ m (corresponding to $M \geq 10$ for a sensor of length 1 cm), the relative error of the amplitude of the reflected spectra was less than 0.05%.

From this it is seen that the approximation of $F_{i_{11}}$ from Eq. (3.3) to Eq. (3.4) can be argued to be also accurate in region 2. With respect to $F_{i_{21}}$ in Eq. (3.3), this can in a similar way be approximated by

$$j\frac{\kappa_i}{\gamma_i}\sinh(\gamma_i\Delta z) \approx j\kappa_i\Delta z \approx j\kappa_i\Delta z\,\mathrm{sinc}(\Delta\beta_i\Delta z),$$

which shows that the approximation of Eq. (3.3) by Eq. (3.4) can be argued to be accurate also in region 2. Finally, Eq. (3.4) is rewritten in a slightly more convenient form by a variable substitution. As stated in Section 3.2.1, the difference between the propagation constants is $\Delta\beta_i = 2\pi n_{\text{eff}}(\frac{1}{\lambda} - \frac{1}{\lambda_{B_i}})$. Therefore, the argument $\Delta\beta_i\Delta z$ in Eq. (3.4) can be expressed as $\Delta\beta_i\Delta z = \alpha - \alpha_i$, where

$$\alpha = \frac{2\pi n_{\text{eff}}\Delta z}{\lambda} \text{ and } \alpha_i = \frac{2\pi n_{\text{eff}}\Delta z}{\lambda_{B_i}}. \tag{3.6}$$

With this, Eq. (3.4) can be rewritten as

$$F_i = \begin{pmatrix} e^{-j(\alpha-\alpha_i)} & -j\kappa_i\Delta z\,\mathrm{sinc}(\alpha-\alpha_i) \\ j\kappa_i\Delta z\,\mathrm{sinc}(\alpha-\alpha_i) & e^{j(\alpha-\alpha_i)} \end{pmatrix}, \tag{3.7}$$

which will be the basis of the analyses in this chapter.

3.4. MEAN STRAIN ESTIMATION

To get a better understanding of the problem with the inaccuracy of Eq. (3.1) under non-uniform strain distributions, this section will start with an example in which the simulation results of an FBG sensor under non-uniform strain distributions are presented. Suppose the strain distribution of Fig. 3.2a, with an average strain of $253.5\mu\varepsilon$, is applied over the length of the FBG sensor. The resulting calculated FBG reflected spectrum will have a non-symmetrical shape and is depicted in Fig. 3.2b. According to Fig. 3.2b, the distance

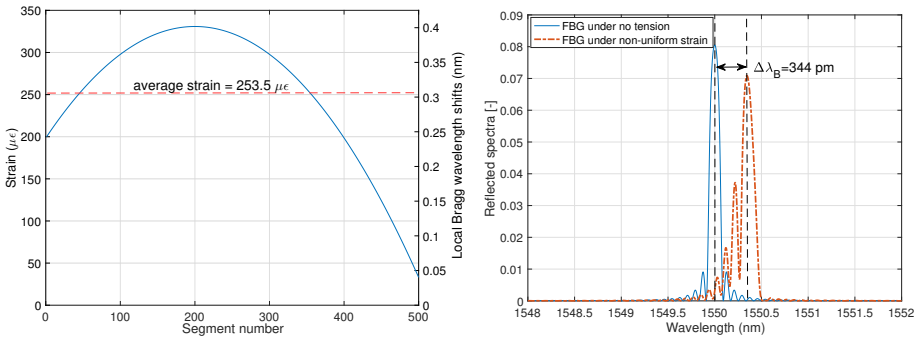

(a) (b)

Figure 3.2: (a): A non-uniform strain distribution (b): The resulting calculated FBG reflected spectra.

between the peak wavelength of the reflected spectra of the undisturbed and strained FBG

sensor is 344 pm, which corresponds to a (mean) strain of $344/k_s = 284.5\,\mu\varepsilon$. Hence, in this example, an error of approximately $31\,\mu\varepsilon$ is introduced which needs to be compensated.

By inspection of (3.2) it is concluded that when subject to a non-uniform strain distribution, instead of finding the peak wavelength of the reflected spectrum of the sensor, the average Bragg wavelength $\bar{\lambda}_B$ of the sensor needs to be found. In the next subsection, it will be seen that $\bar{\lambda}_B$ can be found by inspection of the side lobes of the FBG reflected spectra and does not necessarily correspond to the peak wavelength. To do so, the ATMM will be used to derive a closed-form approximation for the side lobes.

3.4.1. CLOSED-FORM APPROXIMATION OF THE SIDE LOBES

In what follows, we assume the coupling coefficient (κ_i) to be constant and equal to κ throughout the length of the sensor. The reason for this assumption is that first, the coupling coefficient does not affect the oscillation frequency of the FBG reflected spectra in neither the main nor side peaks, and second, due to the fact that it often has only a small variation along the length of the sensor, its effect on the amplitude is negligible.

Suppose there is an arbitrary non-uniform strain distribution over the length of the FBG sensor. Each segment i of the FBG sensor undergoes a local strain s_i, resulting in an asymmetric overall reflected spectrum. Multiplying all M approximated transfer matrices F_i defined in Eq. (3.7), resulting in the composite matrix F, entry F_{11} will have the form

$$F_{11} = e^{-j(M\alpha - \sum_{i=1}^{M}\alpha_i)} + \sum_{n=1}^{\lfloor \frac{M}{2} \rfloor} \sum_{l=1}^{\binom{M}{2n}} \{ \prod_{i \in x_l} (-1)^n \kappa \Delta z \,\mathrm{sinc}(\alpha - \alpha_i) \prod_{i \in x_l^C} e^{(-1)^v j(\alpha - \alpha_i)} \}, \tag{3.8}$$

where $x_l \in X_{2n}$ with X_{2n} being the set of all possible combinations of $2n$ numbers taken from the set $\Omega = \{1, 2, ..., M\}$. As an example, assuming $n = 1$, we will have $X_2 = \{\{1,2\},\{1,3\},...\{M-1, M\}\}$. Also, $x_l^C = \Omega \setminus x_l$ is the complement of the set x_l in Ω, and $v \in \{0, 1\}$ which depends on the set x_l. Similarly, we find that

$$\begin{aligned} F_{21} = &\sum_{i=1}^{M} \kappa \Delta z \,\mathrm{sinc}(\alpha - \alpha_i) e^{-j\left((M-2i+1)\alpha + \sum_{k<i}\alpha_k - \sum_{k>i}\alpha_k\right)} \\ &+ \sum_{n=1}^{\lfloor \frac{M}{2} \rfloor} \sum_{l=1}^{\binom{M}{2n+1}} \{ \prod_{i \in y_l} (-1)^n \kappa \Delta z \,\mathrm{sinc}(\alpha - \alpha_i) \prod_{i \in y_l^C} e^{(-1)^v j(\alpha - \alpha_i)} \}, \end{aligned} \tag{3.9}$$

where $y_l \in Y_{2n+1}$ with Y_{2n+1} being the set of all possible combinations of $2n+1$ numbers taken from Ω. By inspection of Eq. (3.8), it can be seen that when the sinc terms are sufficiently damped, the dominant term will be the first exponential, which has magnitude 1. As a consequence

$$R(\lambda) \approx |F_{21}|^2, \quad \text{for } \forall i \in \Omega,\ |\lambda - \lambda_{B_i}| > \lambda_{\text{th}}, \tag{3.10}$$

where $\lambda_{\text{th}} > 0$ is a threshold wavelength for which (3.10) holds. Note that the condition $|\lambda - \lambda_{B_i}| > \lambda_{\text{th}}$ is approximately the same as $|\alpha - \alpha_i| > \alpha_{\text{th}}$. Using similar arguments, it can be shown that the dominant terms in Eq. (3.9) are given by those in the first summation,

as the second summation contains products of sinc functions whose amplitudes are small when $|\lambda - \lambda_B| > \lambda_{\text{th}}$. For notational convenience, let $\xi_i = \frac{\kappa_i \Delta z}{2j(\alpha-\alpha_i)}$. With this, we have

$$\begin{aligned} F_{21} &\approx \sum_{i=1}^{M} \kappa \Delta z \,\text{sinc}(\alpha - \alpha_i) e^{-j\left((M-2i+1)\alpha + \sum\limits_{k<i}\alpha_k - \sum\limits_{k>i}\alpha_k\right)} \\ &\overset{(a)}{=} \sum_{i=1}^{M} \xi_i \left(e^{-j\left((M-2i)\alpha + \sum\limits_{k\leq i}\alpha_k - \sum\limits_{k>i}\alpha_k\right)} - e^{-j\left((M-2(i-1))\alpha + \sum\limits_{k<i}\alpha_k - \sum\limits_{k\geq i}\alpha_k\right)} \right) \\ &\overset{(b)}{=} \sum_{i=1}^{M-1} (\xi_i - \xi_{i+1})\, e^{-j\left((M-2i)\alpha + \sum\limits_{k\leq i}\alpha_k - \sum\limits_{k>i}\alpha_k\right)} + \xi_M e^{jM(\alpha-\bar{\alpha})} - \xi_1 e^{-jM(\alpha-\bar{\alpha})}, \end{aligned} \tag{3.11}$$

where (a) follows by applying Euler's equation and (b) is obtained by re-arranging terms. The following results are obtained.

Lemma 1. *Let $\lambda_{B_i} = \bar{\lambda}_B + \Delta_i$ and $\overline{\Delta^2} = \frac{1}{M}\sum_i \Delta_i^2$. If $|\Delta_i| \ll \bar{\lambda}_B$ for all i, then*

$$1) \qquad \bar{\alpha} = \frac{2\pi n_{\text{eff}} \Delta z}{\bar{\lambda}_B} + \mathcal{O}\left(\frac{\overline{\Delta^2}}{\bar{\lambda}_B^3}\right). \tag{3.12}$$

If, in addition, $|\lambda - \bar{\lambda}_B| > \lambda_{\text{th}}$ and $|\lambda_{B_i} - \lambda_{B_{i+1}}| \ll \lambda_{\text{th}}$ for all i, then

$$2) \qquad |\xi_i - \xi_{i+1}| \ll |\xi_1|, |\xi_M|.$$

Proof. See Appendix A.1. □

Assuming that the conditions of Lemma 1 are satisfied, it is concluded that

$$F_{21} \approx \xi_M e^{jM(\alpha-\bar{\alpha})} - \xi_1 e^{-jM(\alpha-\bar{\alpha})}, \tag{3.13}$$

so that

$$\begin{aligned} R(\lambda) &\overset{(a)}{\approx} 4\text{Re}(\xi_1 \xi_M^*) \sin^2\left(M(\alpha-\bar{\alpha})\right) + (\xi_M - \xi_1)^2 \\ &= \frac{(\kappa\Delta z)^2}{(\alpha-\alpha_1)(\alpha-\alpha_M)} \sin^2\left(M(\alpha-\bar{\alpha})\right) + (\xi_M - \xi_1)^2 \\ &\overset{(b)}{\approx} (\kappa L)^2 \,\text{sinc}^2\left(M(\alpha-\bar{\alpha})\right) + (\xi_M - \xi_1)^2, \end{aligned} \tag{3.14}$$

where (a) follows from (3.13) using elementary trigonometric identities and (b) follows from the presumption that small variations in the amplitude of the sin function in Eq. (3.14), caused by replacing the α_1 and α_M terms by $\bar{\alpha}$ are negligible. Also note that $M\Delta z = L$, the length of the sensor.

Some remarks are in place here. The assumptions for which the results of Lemma 1 hold are met in most practical scenarios. Indeed, in practice the deviations from the mean Bragg wavelength is less than a few nanometers. As an example, the strain distribution as depicted

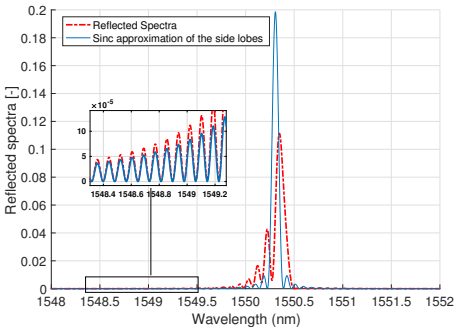

Figure 3.3: FBG reflected spectra under an arbitrary non-uniform strain field (in blue) and the approximation for the side lobes in red.

in Fig. 3.2a gives rise to a maximum deviation of about 250 pm, which is, compared to the average Bragg wavelength ($\bar{\lambda}_B \approx 1550$ nm), three to four orders of magnitude smaller. Larger deviations are unrealistic in the sense that too large Δ_i will result in breaking the FBG sensor or require unrealistically long sensors. In addition, if Δz are chosen sufficiently small and it is assumed that the strain distribution cannot change arbitrarily fast along the length of the sensor, we will have $|\lambda_{B_i} - \lambda_{B_{i+1}}| \ll \lambda_{\text{th}}$, where λ_{th} is in the order of 1-2 nm. By inspection of Fig. 3.2a, if the number of segments is chosen to be $M = 100$, the maximum difference between successive Bragg wavelengths λ_{B_i} is approximately 5 pm, which is three orders of magnitude smaller than λ_{th}.

Coming back to the approximation (3.14), it is seen that the reflected spectrum can be approximated by a scaled (squared) sinc function having a possible offset. This approximation only holds in the wavelength range $|\lambda - \lambda_B| > \lambda_{\text{th}}$. To illustrate this approximation, Fig. 3.3 compares the reflected spectrum of a simulated FBG sensor under the non-uniform strain field depicted in Fig. 3.2a, along with its approximation given by (3.14). It can be seen that this approximation does not hold for the main lobe, but does hold for the wavelength region for which $|\lambda - \lambda_B| > \lambda_{\text{th}}$, where λ_{th} is in the order of 1-2 nm which can be identified by setting a threshold level on the amplitude of the reflected spectra[4].

As was shown in Section 3.2.1, it is $\bar{\lambda}_B$ that needs to estimated in order to compute the mean strain distribution $\bar{s}$ using (3.2). However, the result of Lemma 1, which gives the relation between $\bar{\lambda}_B$ and $\bar{\alpha}$, shows that this can be accomplished by estimating $\bar{\alpha}$, which is the phase shift of the sinc approximation of the reflected spectrum. A maximum likelihood estimator of $\bar{\alpha}$ is therefore given by the phase-shift value that maximises the cross-correlation between the observed reflected spectrum and $\text{sinc}^2\left(M(\alpha - \bar{\alpha})\right)$ [13, p. 192], where the correlation in this case is only taken over the range $|\lambda - \lambda_B| > \lambda_{\text{th}}$. Note that since the cross-correlation is shift and scale invariant, neither any discrepancy between the magnitude of the reflected spectrum and its sinc approximation, as is present in the example shown in Fig. 3.3, nor a possible offset in the spectrum will affect the estimation of $\bar{\alpha}$. In addition, even when the first $M-1$ exponential terms in (3.11) cannot be completely neglected, making the approximation (3.13) less accurate, this will not have a significant impact on the

[4]Here the threshold level was set at 1 percent of the peak amplitude ($20\,dB$ difference in the amplitude).

estimation of $\bar{\alpha}$ since the exponentials give low correlation with the sinc function (they have different oscillating frequencies), making the proposed method robust against inaccuracies in (3.14). Also, this method is not subject to any additional spectral noise or errors compared with conventional FBG interrogation methods, and due to the filtering properties of the correlation function, it is robust against amplitude noise as well. It is worth mentioning that the proposed mean strain estimation method uses the information in the side-lobes of the reflected spectra, therefore, FBG sensors whose side-lobes are suppressed and have really small amplitudes (such as Gaussian or raised-cosine apodized FBG sensors) will not perform well with our methods.

3.4.2. Practical considerations

In practical scenarios the output of the FBG sensor is obtained using an interrogator. As a consequence, the data available for processing are samples of the reflected spectra, uniformly spaced in the λ-domain. Instead of performing the processing in the α-domain, which would require a non-uniform re-sampling of the data, we could equally well perform the correlation in the wavelength domain directly. To see this, let $\lambda = \bar{\lambda}_B + \Delta\lambda > \lambda_{\text{th}}$, and assume that $|\Delta\lambda| \ll \bar{\lambda}_B$. This assumption is generally met in practice since $|\Delta\lambda|$ is in the order of a few nanometers, which is three orders of magnitude smaller than $\bar{\lambda}_B$. Moreover, let $\rho = 2\pi n_{\text{eff}}\Delta z$. As a consequence, the α as defined in Eq. (3.6), can be rewritten as

$$\alpha = \frac{\rho}{\bar{\lambda}_B + \Delta\lambda} \overset{(a)}{\approx} \frac{\rho}{\bar{\lambda}_B}\left(1 - \frac{\Delta\lambda}{\bar{\lambda}_B}\right) \overset{(b)}{\approx} \bar{\alpha} - \frac{\rho}{\bar{\lambda}_B^2}\Delta\lambda,$$

where (a) is a first-order Taylor series approximation of α and (b) follows from (3.12). Hence, a linear change of the wavelength manifests itself as a linear change in α, and as a consequence, uniform sampling of λ will result in uniform sampling of α and vice versa, assuming $|\Delta\lambda| \ll \bar{\lambda}_B$.

Although the above introduced method for retrieving $\bar{\lambda}$ will work for computer simulations, due to the presence of birefringence effects and other unwanted artefacts on real FBG measurements like non-longitudinal strains, the algorithm might lead to unwanted maxima in the cross-correlation function and therefore to incorrect phase retrieval. To overcome this problem in practical scenarios, a slight modification is introduced to the above proposed algorithm. Instead of computing the cross-correlation between the reflected spectrum and the sinc function directly, first the two reflected spectra are aligned (recorded before and after applying the strain) based on their centre of mass [14]

$$\lambda_{B_c} = \frac{\int_{\boldsymbol{\lambda}} \lambda R(\lambda) d\lambda}{\int_{\boldsymbol{\lambda}} R(\lambda) d\lambda} \tag{3.15}$$

where $\boldsymbol{\lambda}$ is the wavelength region that covers the reflection spectrum. This shift, $\Delta\lambda_{B_c}$, can be used to find a rough estimate of $\bar{\lambda}$, say $\tilde{\lambda} = \lambda_B + \Delta\lambda_{B_c}$. After this, the final phase shift is calculated by maximising the cross-correlation of the side lobes of both observations over a small interval around $\tilde{\lambda}$, resulting in an additional phase shift $\delta\lambda_B$. Experiments have shown that this modification results in more robust mean strain estimates and is illustrated in Fig. 3.4a and 3.4b. The modified algorithm is summarised in Algorithm 1. Note that, as mentioned in the introduction, existing algorithms for estimating the mean strain value are

Algorithm 1 Mean strain estimation

1: Align the centre of mass of the reflected spectra of the FBG sensor measured with and without applying a (non-uniform) strain, thereby defining $\Delta\lambda_{B_c}$.

2: Maximise the cross-correlation of the side lobes of both measurements over a small interval with a typical value of 1 nm around $\tilde{\lambda} = \lambda_B + \Delta\lambda_{B_c}$, resulting in an additional phase shift $\delta\lambda_B$.

3: Calulate the required phase shift $\bar{\lambda}_B - \lambda_B = \Delta\lambda_{B_c} + \delta\lambda_B$.

4: Calculate the mean strain using Eq. (3.2).

based on the shift of the peak wavelength. That is, they estimate the mean strain value based on $\Delta\lambda_B$. In that sense, $\delta\lambda_B$ can be interpreted as an error compensating term for methods based on peak wavelength alignment.

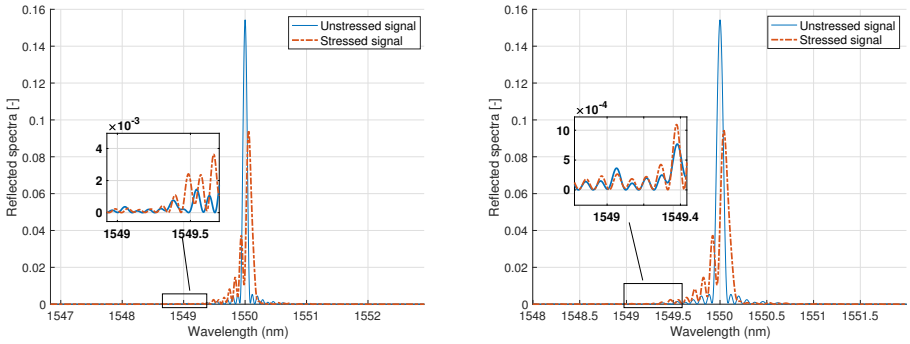

(a) (b)

Figure 3.4: The FBG reflected spectra of the unstrained sensor (blue) and the strained sensor (red) where (a) shows both spectra aligned with respect to their centre of mass and (b) with respect to maximising the cross-correlation of the side peaks.

3.5. EXPERIMENTAL RESULTS

In this section, experimental results for non-uniform strain distributions on FBG sensors will be presented, obtained by both computer simulations and experimental FBG measurements.

In the first experiment, which is a computer simulation, the strain distribution of Fig. 3.2a is applied over the length of the sensor, resulting in the FBG reflected spectrum of Fig. 3.2b, where $M = 500$. In order to create a more realistic experiment, the sensor was assumed to have random fluctuations on the magnitude of the refractive index change, which results in random variations of the coupling coefficient along the length of the sensor, and eventually, in the emergence of unwanted lower frequency harmonics on the side-lobes of the FBG

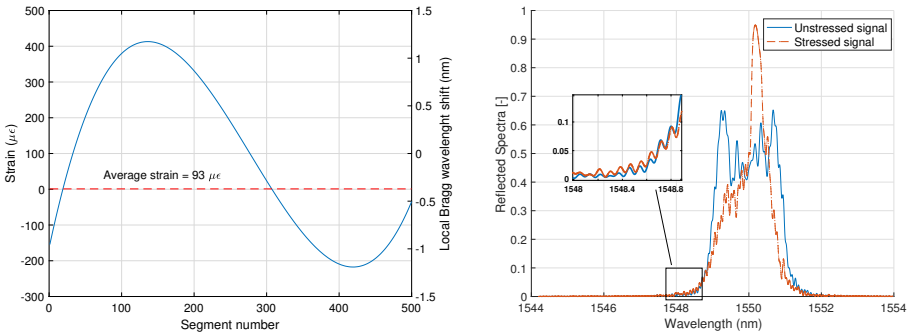

(a) (b)

Figure 3.5: (a): A polynomial type strain distribution, applied over the length of the LCFBG sensor. (b): The unstressed and stressed LCFBG reflected spectra are aligned with respect to maximising the correlation of their side peaks.

reflection spectra. Following the steps outlined in Algorithm 1, first the reflected spectra with respect to their centre of mass are aligned, as shown in Fig. 3.4a, and the shift $\Delta\lambda_{B_c}$ is measured. In the example at hand, this shift is given by $\Delta\lambda_{B_c} = 296\,\text{pm}$. The next step is then to shift the reflected spectrum such that the cross-correlation of the side lobes is maximised, as shown in Fig. 3.4b, resulting in an additional phase shift of $\delta\lambda_B = +12\,\text{pm}$. After computing the final phase shift as $\Delta\lambda_{B_c} + \delta\lambda_B = 308\,\text{pm}$ (step 3 of Algorithm 1), the mean strain is computed using (3.2), resulting in $\bar{s} = 254.7\,\mu\varepsilon$. It can be seen that the resulting estimation for the mean strain over the length of the sensor is quite close to the actual mean strain ($253.5\,\mu\varepsilon$), where the proposed algorithm compensates for an error of around $30\,\mu\varepsilon$ as compared to traditional strain measurement algorithms, see Section 3.4.

In the second experiment, which is another computer simulation, the performance of the algorithm when a non-uniform strain distribution is applied on a linearly chirped fibre Bragg grating (LCFBG) sensor is investigated. The designed sensor, again containing refractive index fluctuations, has a grating distribution with $\frac{d\lambda_B}{dz} = 2.5\,\text{nm/cm}$, and a length of 1 cm. The strain distribution applied over the length of the sensor is shown in Fig. 3.5a. The mean strain value in this experiment is $93\,\mu\varepsilon$, but the traditional strain estimation algorithm in LCFBGs which is solely based on the shift of the centre of mass of the stressed and unstressed signals, show a wavelength shift of around 42.6 pm or a strain estimation of $35\,\mu\varepsilon$. Using our algorithm, the compensating shift that results from maximising the cross correlation of the side-lobes was $\delta\lambda_B = +72\,\text{pm}$, which accounts for a mean strain error of $59.5\,\mu\varepsilon$. The final mean strain estimation based on our algorithm is therefore, $94.5\,\mu\varepsilon$. Fig. 3.5b shows the reflected spectra of the stressed and unstressed LCFBG after the compensating shift. Note the synchronised side-lobes of the two reflected spectra.

In the third experiment, the proposed method will be evaluated using experimental FBG measurements in a controlled laboratory environment. The FBG sensors used in this study are the LBL-1550-125 draw tower grating (DTG) type sensors (FBGS International NV). The length of the sensors are 10 mm, with a nominal Bragg wavelength of 1550.08 nm and maximum reflectivity level of about 10%. Although the algorithm would work at its best in

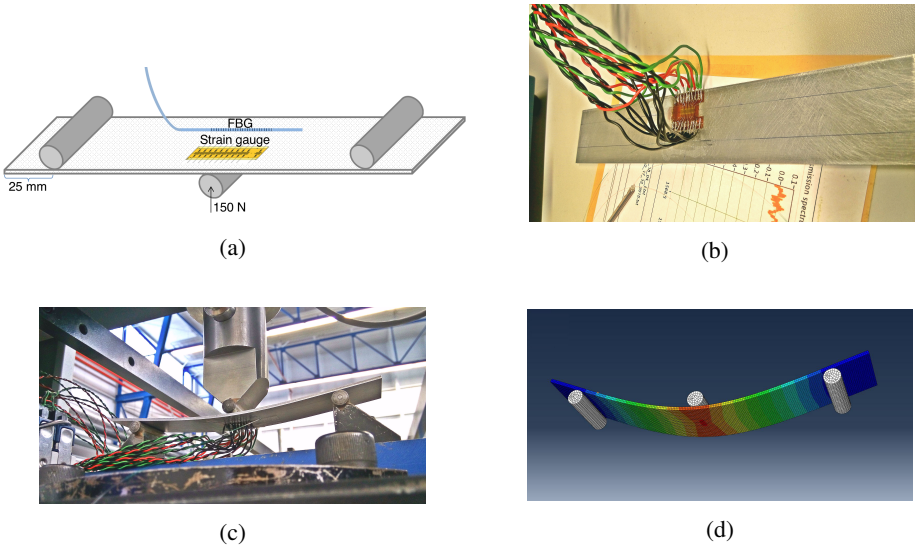

Figure 3.6: (a): A schematic design of the specimen and the location of the sensors. (b): The test specimen (bottom view) with the surface mounted strain gauge and the FBG. (c): The test specimen under load, while the signals were being recorded. (d): Finite element modelling of the specimen under a similar load.

sensors with higher reflectivity levels, we have two reasons for choosing DTG sensors with such low reflectivity levels in our experiments. The first reason is that DTG sensors have a much higher tensile strength compared to FBG sensors that are produced using traditional strip and recoating methods. They can easily endure static strains of more than 10000 $\mu\varepsilon$ which can commonly occur in practical applications. The second reason is to show that our algorithm can equally well perform, even at such low reflectivity levels, provided that the sensor is interrogated with a high dynamic range interrogator.

Since the information in the side lobes of the reflected spectra plays a significant role in this study, a high dynamic range interrogator was used to record the output of the sensors. The PXIe-4844 FBG interrogator from National Instruments, which has a dynamic range of 40 dB and a wavelength accuracy of 4 pm, was used to interrogate the sensors. The wavelength range for this device ranges from 1510 nm to 1590 nm.

In order to validate the results, both electrical strain gauge measurements and results obtained by finite element modelling (FEM) were used as reference strain measurements. For the strain gauge measurements, an array of 10 miniature strain gauges with a pitch of 1 mm (HBM 1-KY11-1/120), spatial resolution of 1 mm, and nominal strain accuracy of less than 5 $\mu\varepsilon$ was used. The data acquisition of the analogue output of the strain gauges was performed using the NI-9219 universal analogue input modules from National Instruments. The data acquisition was carried out using the National Instruments LabVIEW software, and the signal processing and conditioning was performed in MATLAB R2016b. To avoid unwanted artefacts and complications associated with finite element modelling, the test setup was designed as simply as possible by using specimens with isotropic properties and subjecting them to a static three point flexural test. The FBG sensor was surface mounted

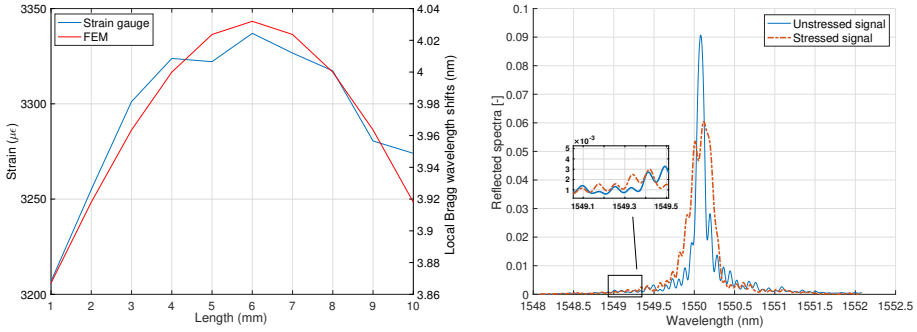

(a) (b)

Figure 3.7: (a): The strain distributions recorded from the strain gauges (in blue) and calculated with FEM (in red). (b): The primary and secondary FBG reflected spectra are aligned with respect to maximising the correlation of their side peaks.

to a piece of 6082 aluminium alloy with dimensions 200 mm × 35 mm × 2 mm, and the strain gauge array was pasted on the specimen in a symmetrical position with respect to the FBG. Fig. 3.6a and 3.6b depict the configuration of this setup. To induce the desired strain field, the specimen was placed in a 10 kN tensile machine, with a force of 150 N applied on the loading pin (see Fig. 3.6c). The finite element modelling of the specimen under such force is shown in Fig. 3.6d in which the element size was set to 1 mm, equal to the spatial resolution of the strain gauges. Note that both sensors are adhered to the specimen on the opposite to the contact surface of the loading pin. To align the two sensors, we referred to the markings on the FBG sensor which had a spatial accuracy of less than 1 mm, and we also used a rolling pin to determine the position of the FBG sensor more accurately. Based on the FEM analysis and the recordings of the strain gauges, the strain distributions shown in Fig. 3.7a were obtained. The mean strain value of the FEM was 3291 $\mu\varepsilon$, whereas the recordings of the electrical strain gauges showed a mean strain value of 3294 $\mu\varepsilon$. In order to estimate the mean strain with the proposed method, the steps outlined in Algorithm 1 were followed again. That is, first the centre of masses of the reflected spectra of the unstrained and strained sensor were aligned, resulting in a wavelength shift of $\Delta\lambda_{B_c} = 3.932$ nm, after which the cross-correlation of the side lobes were maximised, as shown in Fig. 3.7b, resulting in an additional wavelength shift of $\delta\lambda_B = +56$ pm. With this, the resulting mean strain estimate becomes $\bar{s} = (3932 + 56)/k_s = 3298\,\mu\varepsilon$. Note that classical methods would estimate the mean strain value from (3.1) resulting in $\bar{s} = \Delta\lambda_B/k_s = 3328\,\mu\varepsilon$. Furthermore, different force loads were applied on the loading pin of the same experimental setup, in which we started from 10 N and then linearly increased the force to 150 N with increments of 10 N. The results of the compensated mean strain estimation using our algorithm, and the mean strain values based on the shift of the Bragg wavelength are presented in Fig. 3.8, and the compensated mean strain values are in accordance with the data from the electrical strain gauges. It is noteworthy that as the applied force increases, the error associated with the traditional strain estimation method increases too, which is due to further deviating from a uniform strain field.

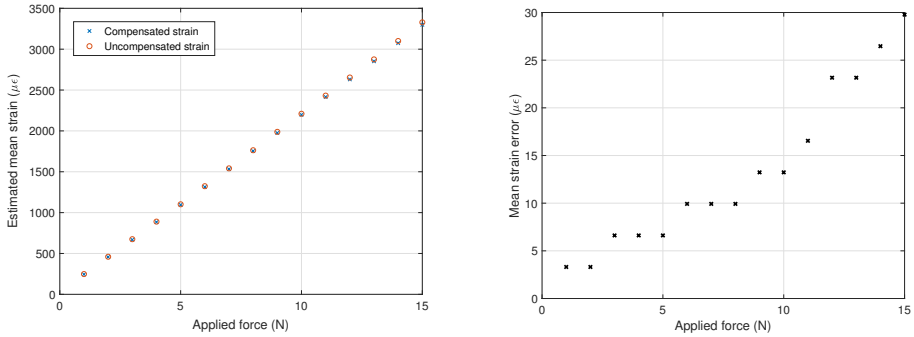

(a) (b)

Figure 3.8: (a): Strain estimation using the traditional strain measurement method (red), and the compensated mean strain values based on our algorithm (blue). (b): The mean strain error associated with uncompensated mean strain estimations.

3.6. CONCLUSIONS

In this chapter, the focus was on estimating the mean strain value in the case of smoothly varying non-uniform strain distributions. A new algorithm was proposed that accurately estimates the mean strain value and showed that this shift is related to the average shift of the peak wavelength along the length of the sensor. In order to find this average shift, an approximation of the well known transfer matrix model was presented, and it was shown that the information needed can be found by inspection of the side lobes of the reflected spectra. That is, the maximum likelihood estimator of the mean strain is obtained by cross-correlating the side lobes of the reflected spectra of the strained and unstrained sensor. In order to overcome possible estimation problems in practical scenarios, an alternative two step algorithm was proposed, where first the centre of mass of the reflection spectra from a strained and an unstrained sensor are aligned, and then the estimate is refined by cross-correlating the side lobes of both spectra over a small range around the shifted Bragg wavelength. The algorithm was validated using both computer simulations and experimental FBG measurements and showed that the newly proposed algorithm clearly outperforms state-of-the-art strain estimation algorithms by compensating for mean strain errors of around $60\mu\varepsilon$. However, in case of non-smooth strain distributions with high variations, and also under extreme birefringence effects, the cross correlation function could lead to local maxima and an incorrect mean Bragg wavelength retrieval. Developing a more robust technique for retrieving the mean Bragg wavelength should be the focus of future studies.

REFERENCES

[1] B. A. Childers, M. E. Froggatt, S. G. Allison, T. C. Moore Sr., D. A. Hare, C. F. Batten, and D. C. Jegley, “Use of 3000 Bragg grating strain sensors distributed on four 8-m optical fibers during static load tests of a composite structure,” 2001.

[2] B. Torres, I. Payá-Zaforteza, P. A. Calderón, and J. M. Adam, “Analysis of the strain

transfer in a new FBG sensor for structural health monitoring," *Engineering Structures*, vol. 33, no. 2, pp. 539–548, 2011.

[3] K. Kuang, R. Kenny, M. Whelan, W. Cantwell, and P. Chalker, "Embedded fibre Bragg grating sensors in advanced composite materials," *Composites Science and Technology*, vol. 61, no. 10, pp. 1379–1387, 2001.

[4] R. De Oliveira, C. Ramos, and A. Marques, "Health monitoring of composite structures by embedded FBG and interferometric Fabry–Pérot sensors," *Computers & Structures*, vol. 86, no. 3, pp. 340–346, 2008.

[5] Y. Okabe, S. Yashiro, T. Kosaka, and N. Takeda, "Detection of transverse cracks in CFRP composites using embedded fiber Bragg grating sensors," *Smart Materials and Structures*, vol. 9, no. 6, p. 832, 2000.

[6] N. Takeda, Y. Okabe, and T. Mizutani, "Damage detection in composites using optical fibre sensors," *Proceedings of the Institution of Mechanical Engineers, Part G: Journal of Aerospace Engineering*, vol. 221, no. 4, pp. 497–508, 2007.

[7] S. Takeda, S. Minakuchi, Y. Okabe, and N. Takeda, "Delamination monitoring of laminated composites subjected to low-velocity impact using small-diameter FBG sensors," *Composites Part A: Applied Science and Manufacturing*, vol. 36, no. 7, pp. 903–908, 2005.

[8] A. Rajabzadeh, R. C. Hendriks, R. Heusdens, and R. M. Groves, "Classification of composite damage from FBG load monitoring signals," in *SPIE Proceedings*, pp. 1016831–1016831, 2017.

[9] Y. Mizutani and R. M. Groves, "Multi-functional measurement using a single FBG sensor," *Experimental Mechanics*, vol. 51, no. 9, pp. 1489–1498, 2011.

[10] K. O. Hill and G. Meltz, "Fiber Bragg grating technology fundamentals and overview," *Journal of Lightwave Technology*, vol. 15, no. 8, pp. 1263–1276, 1997.

[11] S. M. Melle, K. Liu, and R. Measures, "A passive wavelength demodulation system for guided-wave Bragg grating sensors," *IEEE Photonics Technology Letters*, vol. 4, no. 5, pp. 516–518, 1992.

[12] M. Yamada and K. Sakuda, "Analysis of almost-periodic distributed feedback slab waveguides via a fundamental matrix approach," *Applied Optics*, vol. 26, no. 16, pp. 3474–3478, 1987.

[13] S. Kay, *Fundamentals of Statistical Signal Processing; Estimation Theory*, vol. I. Prentice Hall, 1993.

[14] C. G. Askins, M. A. Putnam, and E. J. Friebele, "Instrumentation for interrogating many-element fiber bragg grating arrays," in *Smart Structures and Materials 1995: Smart Sensing, Processing, and Instrumentation*, vol. 2444, pp. 257–267, International Society for Optics and Photonics, 1995.

4

On the Centroid Method for Average Strain Estimation in Uniform FBG Sensors

No one dies of fatal truths nowadays: there are too many antidotes.

Friedrich Nietzsche, Human, All Too Human

One of the most interesting properties of fibre Bragg grating sensors is the linear relationship between the amount of uniform strain over the length of the sensor and the shift of the peak wavelength of the sensor's reflection spectrum. In previous works, it has been shown that this measure does not offer reliable results under non-uniform strain fields and in noisy setups. In this paper, we will show that for uniform FBG sensors under any arbitrary axial strain field, the centre of mass of the reflection spectrum corresponds to the average strain value. We will also analyse the effect of spectral noise and noise on the grating period on the overall performance of the centre of mass method. Using computer simulated and laboratory experiments, we will show that substituting the existing peak tracking based approaches with the centre of mass approach could eliminate average strain estimation errors of nearly $1000\,\mu\varepsilon$.

4.1. Introduction

In the literature, several methods for demodulation of FBG sensors have been described. Zhang et al. studied the accuracy of several demodulation techniques from an experimental point of view in [1]. In [2], Negri et al. created benchmarks for different demodulation

*This chapter is submitted to the Journal of Strain, as "On the Centroid Method for Average Strain Estimation in Uniform FBG Sensors", by A. Rajabzadeh, R. Heusdens, R. C. Hendriks, and R. M. Groves, 2020.

methods, including maximum peak tracking, the centroid method [3], polynomial fitting or Gaussian fitting [4], and neural networks [2]. Using experimental and simulated measurements under uniform strain fields, they argued that for uniform FBG sensors, the centroid method has a high accuracy. However, they claimed that when using the centroid algorithm for apodized FBG sensors (either Gaussian or raised-cosine apodization) [5], the accuracy declines. Among other things, these claims will be investigated in this chapter.

In recent years, there have also been several studies in which new methods have been proposed for low sample spectral resolution conditions. The most recent of these methods are based on the principle of fast phase correlation [6], and based on the Karhunen-Loeve Transform [7]. Although these methods have a reported enhanced accuracy under uniform strain fields and under coarse interrogation, they do not perform well under non-uniform strain fields, and can result in significant average strain errors. This claim will be discussed in more detail in section 4.6.

In this study, we will focus on the already presented centroid method [3], which tracks the shift of the centre of mass of the reflection spectrum as a measure for average strain estimation. This method was first introduced by Askins et al. as an approach towards interrogation of FBG sensors using low spectral resolution and noise sensitive interrogation systems [3]. However, to our knowledge, there has not yet been any study to analytically investigate its performance in non-uniform strain fields, and its robustness against different sources of noise in the system. In this study we will analytically show that in theory, the centre of mass of the reflection spectrum corresponds to the average of the arbitrary axial strain field applied over the active length of the uniform FBG sensor. Such non-uniform strain fields are mostly common when an FBG sensor gets in contact with damaged areas in engineering structures. For instance, in the application of embedded FBG sensors between composite laminates, such strain fields can result from having micro-cracks in the matrix material along the FBG length [8, 9], or from the delamination of the composite layers [10]. To obtain the average of the axial strain field, we first need a closed form approximation of the FBG reflection spectrum, which can be achieved using the recently proposed approximated transfer matrix model (ATMM) (see Chapter 3 or [11]). The ATMM has been used before in a diversity of applications. For example, in [12] we used this formulation to prove that under anti-symmetrical strain fields or grating structures, the FBG reflection spectrum will be symmetrical. Furthermore, in this chapter we analyse the performance of the centroid method when subject to noise in the different stages of the measurement process, and also investigate its use for apodized FBG sensors. Using simulated experiments and experimental measurements, we will validate the presented theory.

4.2. Closed Form Approximation of the FBG reflection spectrum

In this section we summarise some of the main results derived in [11], which we use later on in Section 4.3 to show that the centre of mass of the reflection spectrum corresponds to the average of the axial strain field applied over the active length of the uniform FBG sensor. Suppose an arbitrary axial stress field is applied to the length of the sensor. The effect of applying a non-uniform strain field on an FBG sensor is that each point along the length of the sensor experiences a different amount of strain. One way to analyse the FBG sensor

response to such strain fields is to discretise the length of the FBG sensor, and assume a piece-wise uniform strain field over the length of the sensor. In the ATMM, which is an approximation of the transfer matrix model [13] as shown in Chapter 3, the length L of the sensor is assumed to be divided into M segments of equal length Δz. In Section 3.4.1 we showed that under such conditions, the reflection spectrum can be approximated as

$$R(\alpha) \approx \left| \sum_{i=1}^{M} \kappa_i \Delta z \, \mathrm{sinc}(\alpha - \alpha_i) e^{-j\left((M-2i+1)\alpha + \sum_{k<i} \alpha_k - \sum_{k>i} \alpha_k\right)} \right|^2, \tag{4.1}$$

where the κ_i's are the coupling coefficients between the forward and backward waves,

$$\alpha = \frac{2\pi n_{\text{eff}} \Delta z}{\lambda} \quad \text{and} \quad \alpha_i = \frac{2\pi n_{\text{eff}} \Delta z}{\lambda_i}. \tag{4.2}$$

In Eq. (4.2) λ is the wavelength range under analysis, λ_i is the local Bragg wavelength of the i'th segment, and n_{eff} is the effective refractive index of the core. Therefore, α can be considered as a representation of the frequency samples under analysis, and the α_i's as scaled local Bragg frequencies. In the next section, we will use this closed-form expression to calculate the centre of mass of the reflection spectrum.

As an example, we applied an arbitrary axial strain distribution over the length of a simulated FBG sensor. Fig. 4.1 shows the original reflection spectrum from the TMM [13], and the approximated reflection spectrum given in Eq. (4.1).

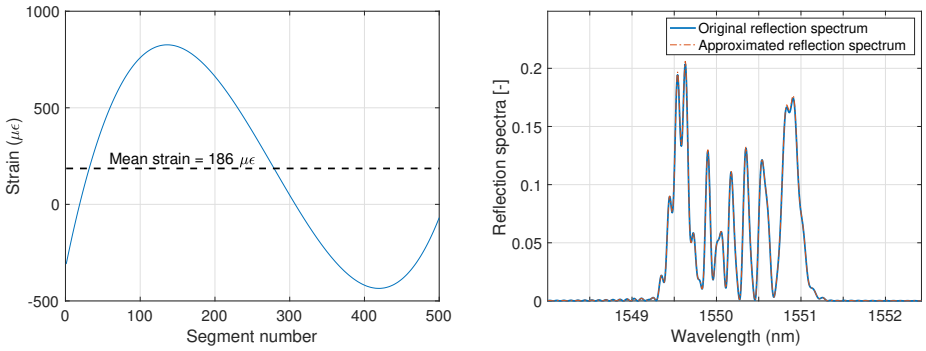

(a) (b)

Figure 4.1: (a): A non-uniform strain field applied on the length of a simulated FBG (b): Comparison between the FBG reflection spectrum from the TMM [13] and the approximated FBG reflection spectra from Eq. (4.1), the ATMM [11].

In Chapter 3 it was shown that the impact of the approximation in Eq. (4.1) in the region of interest is insignificant, while it leads to simple analytic expressions of the reflection spectrum. However, a few remarks are in order. It can be seen that this approximation is most accurate when the amplitude of the refractive index modulation is relatively small (and consequently for smaller κ_i values), and the reflectivity levels are below around ninety percent. As it can be seen from Fig. 4.1, in this case, the difference between the approximated and the original reflection spectra is negligible and can be ignored for the current study.

It is noteworthy that for sensors with high reflectively levels where the difference between the approximated and the original reflection spectrum are significant, the accuracy of the centroid method will decline as well.

4.3. Centre of Mass as a Measure for Average Strain Estimation

The linear relationship between the local Bragg wavelengths and the uniform strain s_i applied over the length of the piece-wise uniform segments of the sensor is given by [14]

$$k_s s_i = (\lambda_{B_i} - \lambda_N). \tag{4.3}$$

In this equation, k_s is a constant characterised by the mechanical and physical properties of the sensor, λ_N is the nominal Bragg wavelength of the unstressed sensor, and λ_{B_i} is the local Bragg wavelength of the segment i. Therefore, by taking the mean over the segments i on both sides of Eq. (4.3) we get

$$k_s \bar{s} = (\bar{\lambda}_B - \lambda_N), \tag{4.4}$$

where $\bar{\lambda}_B$ is the average of the local Bragg wavelengths. On the other hand, in Section 3.4.2 we showed that

$$\bar{\alpha} = \frac{2\pi n_{\text{eff}} \Delta z}{\bar{\lambda}_B} + \mathcal{O}\left(\frac{\overline{\Delta^2}}{\bar{\lambda}_B^3}\right). \tag{4.5}$$

In this equation, $\bar{\alpha} = \frac{1}{M}\sum_i \alpha_i$ is the average of the local Bragg frequencies over the segments i, $\overline{\Delta^2} = \frac{1}{M}\sum_i \Delta_i^2$ where Δ_i is the local deviation from the Bragg wavelength $\bar{\lambda}_B$ for segment i. The second term of Eq. (4.5) can be neglected, since $\bar{\lambda}_B$ is orders of magnitude larger than $\overline{\Delta^2}$. Therefore, by calculating $\bar{\alpha}$, we know $\bar{\lambda}_B$, and the average strain of the non-uniform axial strain field follows from Eq. (4.4).

In this section, we will evaluate the performance of the centroid method in uniform FBG sensors. We show that theoretically, for uniform FBG sensors, the centre of mass of the reflection spectrum corresponds to $\bar{\alpha}$, the average of the local Bragg frequencies of all the segments, or equivalently to the average strain over the length of the sensor. In other words, we will show that

$$\bar{\alpha} = \frac{\int_{-\infty}^{+\infty} \alpha R(\alpha) \mathrm{d}\alpha}{\int_{-\infty}^{+\infty} R(\alpha) \mathrm{d}\alpha}, \tag{4.6}$$

or instead, we can rearrange the terms in Eq. (4.6) and equivalently show that

$$\int_{-\infty}^{+\infty} (\alpha - \bar{\alpha}) R(\alpha) \mathrm{d}\alpha = 0. \tag{4.7}$$

To do so, the reflection spectrum from Eq. (4.1) can be expanded and rewritten as

$$R(\alpha) \approx \Delta z^2 \Big\{ \overbrace{\sum_{i=1}^{M} \kappa_i^2 \operatorname{sinc}(\alpha - \alpha_i)^2}^{S_1} + \overbrace{2 \sum_{\substack{m \\ m>n}} \sum_{n} \kappa_m \kappa_n \operatorname{sinc}(\alpha - \alpha_m) \operatorname{sinc}(\alpha - \alpha_n) \cos\left((2m - 2n)\alpha - \beta_{m,n}\right)}^{S_2} \Big\}, \tag{4.8}$$

where $\beta_{m,n} = (\sum_{k<m} \alpha_k + \sum_{k<n} \alpha_k - \sum_{k>m} \alpha_k - \sum_{k>n} \alpha_k)$. Assuming that for a uniform FBG sensor, the variation of the coupling coefficients along the length of the sensor is negligible ($\kappa_i \approx \kappa$), the reflection spectrum from Eq. (4.1) can be rewritten as

$$R(\alpha) \approx (\kappa \Delta z)^2 \Big\{ \overbrace{\sum_{i=1}^{M} \operatorname{sinc}(\alpha - \alpha_i)^2}^{S_1'} + \overbrace{2 \sum_{\substack{m \\ m>n}} \sum_{n} \operatorname{sinc}(\alpha - \alpha_m) \operatorname{sinc}(\alpha - \alpha_n) \cos\left((2m - 2n)\alpha - \beta_{m,n}\right)}^{S_2'} \Big\}. \tag{4.9}$$

Let us split the summation in Eq. (4.9) into two terms, S_1' and S_2', as indicated in Eq. (4.9). Factoring the $(\kappa \Delta z)^2$ term and working out Eq. (4.7) for the first term S_1' yields

$$\begin{aligned} \int_{-\infty}^{+\infty} (\alpha - \bar{\alpha}) S_1' \mathrm{d}\alpha &= \int_{-\infty}^{+\infty} \sum_{i=1}^{M} (\alpha - \alpha_i + \alpha_i - \bar{\alpha}) \operatorname{sinc}(\alpha - \alpha_i)^2 \mathrm{d}\alpha \\ &= \sum_{i=1}^{M} \int_{-\infty}^{+\infty} (\alpha - \alpha_i) \operatorname{sinc}(\alpha - \alpha_i)^2 \mathrm{d}\alpha + \sum_{i=1}^{M} (\alpha_i - \bar{\alpha}) \left(\int_{-\infty}^{+\infty} \operatorname{sinc}(\alpha - \alpha_i)^2 \mathrm{d}\alpha \right). \end{aligned} \tag{4.10}$$

The first summation term in Eq. (4.10) is zero, since it is the integration of an odd symmetric function. Since $\int_{-\infty}^{+\infty} \operatorname{sinc}(\alpha - \alpha_i)^2 \mathrm{d}\alpha = \pi$, we conclude that

$$\int_{-\infty}^{+\infty} (\alpha - \bar{\alpha}) \left(\sum_{i=1}^{M} \operatorname{sinc}(\alpha - \alpha_i)^2 \right) \mathrm{d}\alpha = \pi \left(\sum_{i=1}^{M} (\alpha_i - \bar{\alpha}) \right) = 0. \tag{4.11}$$

Now we analyse the S_2' term of Eq. (4.9) when substituted in Eq. (4.7), for which we use the following lemma:

Lemma 2.

$$\begin{aligned} &I = \int_{-\infty}^{+\infty} (x - \theta_c) \operatorname{sinc}(x - \theta_1) \operatorname{sinc}(x - \theta_2) \cos(nx - \theta_3) dx = 0, \\ &\forall \theta_c, \theta_1, \theta_2, \theta_3 \in \mathbb{R},\ n \in \mathbb{Z}. \end{aligned} \tag{4.12}$$

Proof. See Appendix A.2. □

Using Lemma 2 and working out Eq. (4.7) for the second term S_2', we have

$$\int_{-\infty}^{+\infty} 2(\alpha-\bar{\alpha})\sum_{\substack{m\\m>n}}\sum_{n}\Big(\operatorname{sinc}(\alpha-\alpha_m)\operatorname{sinc}(\alpha-\alpha_n)\cos\big((2m-2n)\alpha-\beta_{m,n}\big)\Big)\mathrm{d}\alpha = 0. \quad (4.13)$$

Hence, we have

$$\int_{-\infty}^{+\infty} (\alpha-\bar{\alpha})R(\alpha)\mathrm{d}\alpha = 0, \quad (4.14)$$

which completes the proof. To summarise, by following the steps given in the following algorithm, the average of non-uniform axial strain fields can be calculated, while the peak tracking or curve fitting algorithms generally fail to do so.

4

Algorithm 2 Average strain estimation

1. Calculate $\bar{\alpha}$ by taking the centre of mass of the reflection spectrum.
2. Use Eq. (4.5) to retrieve $\bar{\lambda}_B$.
3. Use Eq. (4.4) to calculate the average strain over the FBG length.

4.4. Effect of Noise on the Centroid Algorithm

Real FBG sensors can be affected by various sources of noise and imperfection that could happen either during the production, or during their interrogation. Here, we investigate the effect of two of the main sources of noise, namely noise on the grating period of the FBG sensor, and additive noise on the overall reflection spectrum due to the interrogation system in use. We will analyse each of these cases in the following subsections, and we assume zero-mean stationary noise that is ergodic in the mean in all our analysis.

4.4.1. Noise on the Grating Period of the FBG

Theoretically, the variations of the grating period of the FBG sensor can be considered as variations in the axial strain distribution along the length of the FBG sensor, through the following relation [15]

$$\Lambda_i = \frac{\lambda_{B_i}}{2n_{\text{eff}}} = \frac{k_s s_i + \lambda_{\text{N}}}{2n_{\text{eff}}}, \quad (4.15)$$

where Λ_i is the grating period in the i'th segment. Therefore, zero-mean noise on the grating period can be regarded as additive zero-mean noise on the axial strain distribution. Since this noise is zero-mean and ergodic in the mean along the length of the sensor, it does not change the overall average strain along the length of the FBG sensor. Hence, the centre of mass of the FBG reflection spectrum would still correspond to the average of the strain distribution along the length of the sensor. In fact, the same holds for any kind of zero-mean strain or grating distribution over the length of the sensor (including linearly chirped Bragg gratings).

4.4.2. SPECTRAL NOISE DUE TO THE INTERROGATION SYSTEM AND PRACTICAL CONSIDERATIONS

As mentioned before, we assume the spectral noise to be zero-mean and additive to the overall FBG reflection spectrum, or

$$\hat{R}(\alpha) = R(\alpha) + Z(\alpha), \tag{4.16}$$

where $R(\alpha)$ is the ideal noiseless reflection spectrum, and $Z(\alpha)$ is the additive noise. In this subsection, we will show that the centroid method is a consistent estimator of the average strain, meaning that it is unbiased, and that by increasing the sampling frequency of the interrogation system, the variance of the estimated average strain decreases (and ultimately leads to zero). In contrast to the presentation of the other sections of this chapter, we will carry out our analysis in the discrete domain so that the effect of the sampling frequency becomes clearer. Furthermore, the analyses are performed over a finite window of interrogation in the α domain. With that, Eq. (4.6) becomes

$$\bar{\alpha} = \frac{\sum_{i=i_1}^{i_2} iA_s(R(iA_s))}{\sum_{i=i_1}^{i_2} R(iA_s)}, \tag{4.17}$$

where A_s is the sampling frequency, and i_1 and $i_2 = i_1 + N - 1$ are integers which indicate the bounds of the interrogation window, and N is the number of samples within this window. Let us substitute $a_i = iA_s$, where a_i's are discrete samples of the continuous α domain and should not be confused with the local Bragg frequencies α_i. Consequently, at each frequency instant along the α domain, the noisy reflection spectrum is as follows

$$\hat{R}(a_i) = R(a_i) + Z(a_i). \tag{4.18}$$

Suppose the centre of mass of the noisy reflection spectrum, $\hat{\bar{\alpha}}$, is calculated as

$$\hat{\bar{\alpha}} = \frac{\sum_{i=i_1}^{i_2} a_i(R(a_i) + Z(a_i))}{\sum_{i=i_1}^{i_2} R(a_i) + Z(a_i)}. \tag{4.19}$$

Let us divide both the nominator and the denominator of Eq. (4.19) by N. Considering the ergodicity of the noise, for a large enough N we have $\sum_{i=i_1}^{i_2} Z(a_i)/N \approx 0$. Therefore, Eq. (4.19) becomes

$$\hat{\bar{\alpha}} \approx \bar{\alpha} + \frac{\sum_{i=i_1}^{i_2} a_i Z(a_i)}{\sum_{i=i_1}^{i_2} R(a_i)} = \bar{\alpha} + \epsilon, \tag{4.20}$$

where we introduced ϵ for notational convenience. Based on Eq. (4.4) and Eq. (4.5), the average strain value is inversely related to $\hat{\bar{\alpha}}$ as follows,

$$\hat{\bar{s}} = \frac{C_1}{\hat{\bar{\alpha}}} + C_2 = \frac{C_1}{\bar{\alpha}} \frac{1}{1 + \frac{\epsilon}{\bar{\alpha}}} + C_2 \overset{(a)}{\approx} \frac{C_1}{\bar{\alpha}} \left(1 - \frac{\epsilon}{\bar{\alpha}}\right) + C_2 = \bar{s} - \frac{C_1 \epsilon}{\bar{\alpha}^2}. \tag{4.21}$$

In the above equation, C_1 and C_2 are constants, and (a) is a first-order Taylor series approximation in which we used the fact that in the current problem $\epsilon \ll \bar{\alpha}$. Since $\mathbb{E}[Z(a_i)] = 0$, taking the expected value of both sides of (4.21) leads to

$$\mathbb{E}[\hat{\bar{s}}] \approx \bar{s} - \frac{C_1}{\bar{\alpha}^2} \frac{\sum_{i=i_1}^{i_2} a_i \mathbb{E}[Z(a_i)]}{\sum_{i=i_1}^{i_2} R(a_i)} = \bar{s}, \tag{4.22}$$

which proves our first claim. For our second claim, we take the variance of the two sides of Eq. (4.21), which leads to

$$\mathrm{Var}(\hat{\bar{s}}) = \mathbb{E}[\hat{\bar{s}}^2] - \bar{s}^2 \approx \frac{C_1^2}{\bar{\alpha}^4} \frac{\sum_{i=i_1}^{i_2} a_i^2 \sigma_z^2}{\left(\sum_{i=i_1}^{i_2} R(a_i)\right)^2}, \tag{4.23}$$

where $\sigma_z^2 = \mathbb{E}[Z(a_i)^2]$ is the variance of the noise. Now suppose the sampling frequency is increased by a factor of n. This means that the summations in Eq. (4.23) will be carried out over nN samples. In this case, the variance of the average strain corresponding to the oversampled reflection spectrum, $\mathrm{Var}(\hat{\bar{s}}_2)$, will be given by

$$\mathrm{Var}(\hat{\bar{s}}_2) \approx \frac{C_1^2}{\bar{\alpha}^4} \frac{\sum_{i=i_1}^{i_1+nN} a_{i,2}^2 \sigma_z^2}{\left(\sum_{i=i_1}^{i_1+nN} R(a_{i,2})\right)^2} \approx \frac{C_1^2}{\bar{\alpha}^4} \frac{n\sum_{i=i_1}^{i_2} a_i^2 \sigma_z^2}{\left(n\sum_{i=i_1}^{i_2} R(a_i)\right)^2} = \frac{1}{n}\mathrm{Var}(\hat{\bar{s}}_1), \tag{4.24}$$

where $a_{i,2}$ are the samples of the α domain in the oversampled reflection spectrum. In Eq. (4.24), we approximated the oversampled reflection spectrum with a quasi-linear interpolation of the original reflected spectrum. Furthermore, we used the property that using such interpolation, the average value of the deterministic functions $\sum a_i^2$ and $\sum R(a_i)$ approximately remain unchanged. With this, we showed that by increasing the sampling frequency by a factor of n, the variance of $\hat{\bar{s}}$ decreases by approximately a factor of n, which concludes the proof of our second claim. In Section 4.6, we will illustrate these properties using some computer simulated experiments.

4.5. Apodized FBG sensors

Now, let us consider the case of apodized FBG sensors. For these sensors, the assumption is that $\kappa_i \approx \kappa$ does not hold anymore, since in these sensors the variation of the coupling coefficients along the length of the sensor is rather huge. In this case, we will use Eq. (4.8) to calculate the centre of mass of the FBG reflection spectrum. It can be seen that $\int_\alpha (\alpha - \bar{\alpha}) S_2 \mathrm{d}\alpha \to 0$, since introducing the different κ_i parameters only scales the integral of Lemma 2. However, for the S_1 term we have

$$\begin{aligned} \int_\alpha (\alpha - \bar{\alpha}) S_1 \mathrm{d}\alpha &= \sum_{i=1}^{M} \kappa_i^2 \int_\alpha (\alpha - \alpha_i)(\mathrm{sinc}(\alpha - \alpha_i)^2)\mathrm{d}\alpha \\ &+ \sum_{i=1}^{M} \kappa_i^2 (\alpha_i - \bar{\alpha})\left(\int_\alpha (\mathrm{sinc}(\alpha - \alpha_i)^2 \mathrm{d}\alpha)\right) = \pi \sum_{i=1}^{M} \kappa_i^2 (\alpha_i - \bar{\alpha}), \end{aligned} \tag{4.25}$$

which does not necessarily equal zero. In other words, for apodized FBG sensors, $\bar{\alpha}$ is not necessarily the centre of mass of Eq. (4.8), and therefore, does not correspond to the average of the strain field over the length of the sensor. As a consequence, the centre of

mass approach does not offer reliable measurements for apodized FBG sensors in general, which is in agreement with the benchmarks presented in [2].

4.6. RESULTS

In this section we will present some computer simulated experiments and a laboratory experiment to validate the performance of the average strain estimation algorithm based on the centroid method. In order to visualise the effect of the aforementioned noises on the result of the centroid method, the experiments of this section are organised as follows. In the first two experiments, we include the FBG production noise as an additive Gaussian noise to the refractive index of the core (with signal-to-noise ratio (SNR) of 14 dB), and on the grating period of the FBG sensor (with variations of around 0.02 nm on the grating period), but we do not include the spectral noise from the interrogation unit. In this paper, SNR is defined as

$$\mathrm{SNR} = 10\log_{10}\frac{P_{\text{signal}}}{P_{\text{noise}}}.$$

In the third simulated example, we introduce additive Gaussian spectral noise to the interrogation, and compare the effect of increasing the sampling frequency in reducing the estimation error. In our simulated experiments, we set $\lambda_n = 1550\,\text{nm}$ for the sensor, and the resolution of the interrogation system is assumed to be 1 pm. Finally, the fourth example is a laboratory experiment to validate the claims made in this paper.

1. In the first example, we consider the strain field given in Fig. (4.1a). The average of this non-uniform strain field is $\bar{s} = 186\,\mu\varepsilon$. Using the centroid method, we derive that $\bar{\lambda}_B = 1550.2116\,\text{nm}$ which corresponds to the estimate $\hat{\bar{s}}_c = 175\,\mu\varepsilon$[1]. The error of this method in such an imperfect FBG sensor is around $10\,\mu\varepsilon$, which is due to the presumed high level of noise on the refractive index of the core, whereas using the peak tracking algorithm we obtain a Bragg wavelength of $\lambda_B = 1549.632\,\text{nm}$ which is equivalent to a strain of $\hat{\bar{s}}_p = -304.38\,\mu\varepsilon$, with an error of $e = |\hat{\bar{s}}_p - \bar{s}| = 485.7\,\mu\varepsilon$.

2. In the second example, we consider a strain distribution that is increasing as a function of a second order polynomial. This strain field and the resulting FBG reflection spectrum is depicted in Fig. 4.2. In this example, the average strain value is $\bar{s} = 233.84\,\mu\varepsilon$, and the centre of mass of the reflection spectrum is at $\bar{\lambda}_B = 1550.2843\,\text{nm}$, which corresponds to an estimate of $\hat{\bar{s}}_c = 235.21\,\mu\varepsilon$. It is noteworthy that the peak tracking approach in this example will lead to $\hat{\bar{s}}_p = -532.67\,\mu\varepsilon$, which has an error of $e = |\hat{\bar{s}}_p - \bar{s}| = 766.5\,\mu\varepsilon$.

3. As discussed in Section 4.4.2, in order to get a better estimate of the average strain in higher noise levels, the reflection spectrum could be sampled with a higher sam-

[1] in these experiments we set $k_s = 1.209 \times 10^{-3}\,\text{nm}/\mu\varepsilon$ for the FBG sensors [5].

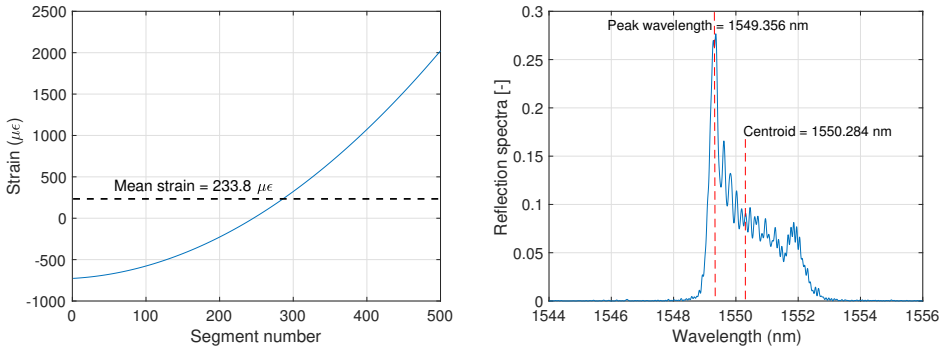

(a) (b)

Figure 4.2: (a): A monotonicly increasing strain field along the length of the FBG (b): The resulting reflection spectrum.

pling frequency. As an example, consider the FBG reflection spectrum from the second example to be affected by additive Gaussian noise, with SNR = 20 dB, given in Fig. (4.3a). For this example, we compare the results of the average strain estimation for two cases. First, having an interrogation system with a resolution of 10 pm, and second, an interrogation system with a resolution of 1 pm. The results of the average strain estimation for 100 different trials are given in Fig. (4.3b). In this example, the variance of the estimator with a resolution of 10 pm is $\mathrm{Var}(\hat{\bar{s}}_1) = 260.5\,\mu\epsilon^2$, and by increasing the resolution to 1 pm, it becomes $\mathrm{Var}(\hat{\bar{s}}_2) = 24.2\,\mu\epsilon^2$, which, as expected from Eq. (4.24), has decreased by a factor of 10. These results are also in agreement with the centroid method performance benchmarks presented in [16]. Also it is important to note that since the centroid method is a consistent estimator, the average of all the estimations from the different trials equals the actual average strain. Therefore, the demodulation of the FBG reflection spectrum under noisy setups can be implemented by averaging several strain estimation measurements from the centroid method and get an accurate strain estimation, even under high spectral noise levels.

4. As a final experimental example, we subjected a uniform FBG sensor, surface mounted on an aluminium plate, to a non-uniform strain field. The sensor was from the company FBGS, with a nominal Bragg wavelength of $\lambda_B = 1535$ nm and length of 8 mm. The FBG sensor was interrogated with a PXIe-4844 interrogator from National Instruments with a wavelength resolution of 4 pm. The non-uniform strain field was created by drilling a slot on the aluminium plate, and the FBG sensor was mounted over this slotted region with a cyanoacrylate solution. Therefore, under an axial tensile test (either under tension or under compression), a non-uniform strain field was created over the FBG length. For reference strain measurements, we painted the surface of the specimen with a speckle pattern by spraying the specimen's surface with contrasting spray paints, and used a 18 MP camera to take images of the specimen. The reference average strain value over the sensor length was calculated by

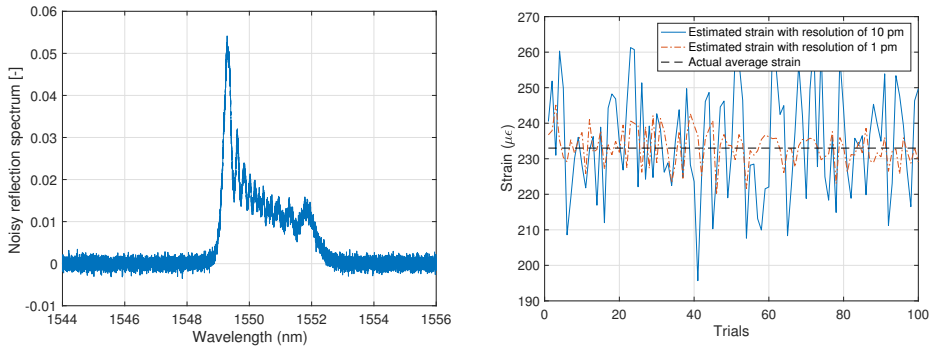

(a) (b)

Figure 4.3: (a): FBG reflection spectrum affected by spectral noise with SNR = 7dB (b): The estimated average strain using the centroid method for 100 different trials of additive Gaussian noise with different interrogation resolutions.

monitoring the shift of the speckled pattern between the ends of the sensor, under no stress and under tension. Fig. 4.4 shows the setup of the experiment in more details. Fig. 4.5a shows the resulting reflection spectra before and after applying the tensile load. As it can be seen from this figure, after applying the non-uniform strain field, the reflection spectrum has split into several peaks, and has widened. Using the peak tracking method, the estimated average strain under tension was calculated to be $\hat{\bar{s}}_p = \Delta\lambda_p / k_s = 1.868/k_s = 1532.4\mu\epsilon$, whereas using the centroid method, we have $\hat{\bar{s}}_c = \Delta\lambda_c / k_s = 1.652/k_s = 1355.2\mu\epsilon$. In the same experiment, the reference average strain was estimated at around $1328\mu\epsilon$. The reasons for the difference between the reference measurement and the estimated average strain using the centroid method are the limitation of the accuracy of the strain estimation with camera images, the non-perfect strain transfer of the cyanoacrylate solution to the FBG sensor, and the calibration error in the FBG demodulation. That being said, having used the peak tracking method instead of the centroid method in this example would have lead to an average strain error of around $e = 200\,\mu\epsilon$.

The experiments presented in this section, clearly demonstrate the superiority of the centre of mass approach over the peak tracking approaches in average strain estimation. It is also noteworthy that for all these experiments, the Gaussian and polynomial fitting algorithm for demodulation do not perform well either. In particular, in the second example, even without the additive spectral noise, the Gaussian fitting approach and polynomial fitting approach will result in $\hat{\bar{s}} = -132\,\mu\varepsilon$, $\hat{\bar{s}} = 101\,\mu\varepsilon$ respectively, which are still far from being accurate. Moreover, methods such as KLT [7] that are reportedly suitable for coarse wavelength interrogation, do not perform well under higher sampling frequencies (such as sampling frequencies below 10 pm). Also, under non-uniform strain fields, they lead to unreliable and inaccurate strain estimations in the presented examples. The reason is that under non-uniform strain fields, the FBG reflection spectra will have several new harmonics frequencies [9]. Therefore, the underlying assumption of the KLT algorithm, which is based

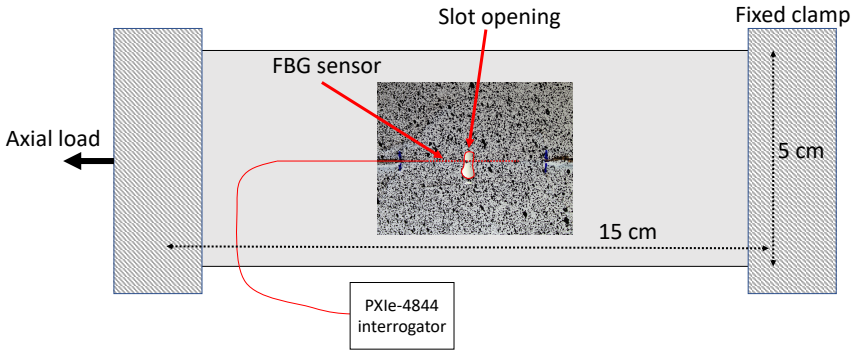

Figure 4.4: The experimental setup used for creating a non-uniform strain field. In order to give an overview of the test setup, the photographed area of the specimen is mounted on a schematic representation of the experiment setup.

on tracking the shift of the dominant eigenvalue of the toeplitz matrix of the Fourier transform of the reflection spectrum [7], is no longer valid. In particular, in the last experiment, the first 30 eigenvalues of the toeplitz matrix of the Fourier transform of the stressed FBG reflection spectrum (the red graph in Fig. 4.5a) had comparable amplitudes, and setting a cut-off threshold was not possible (see Fig. 4.5b).

Finally, it is noteworthy that the application of the centroid method is not limited to uniform FBG sensors, as it is currently the most prevalent demodulation algorithm for load measurement schemes using linearly chirped FBG sensors as well. Based on the discussions in subsection 4.4.1, it can be seen that applying a non-uniform strain field over a chirped FBG sensor is analogous to applying a summation of two simultaneous strain fields over the length of the sensor, one corresponding to the chirped grating structure, and one corresponding to the axial load itself. Therefore, we can conclude that the centroid approach would lead to reliable and meaningful strain estimation in chirped FBG sensors as well, under both uniform and non-uniform strain fields.

4.7. Conclusions

In this paper we analytically proved that for uniform FBG sensors, the centre of mass of the FBG reflection spectrum corresponds to the average of the local Bragg wavelengths along the length of the FBG sensor, which equivalently, corresponds to the average strain value of the strain field to which the sensor is subjected. Furthermore, we showed the robustness of this method against noise on the grating period of the FBG, and the spectral noise from the interrogation system. We also claimed that the results of this chapter can be extended to chirped Bragg grating sensors as well, however, they do not necessarily hold for apodized FBG sensors. Moreover, we argued that for FBG sensors with high reflectivity levels, the accuracy of the centroid method declines. With computer simulated and laboratory

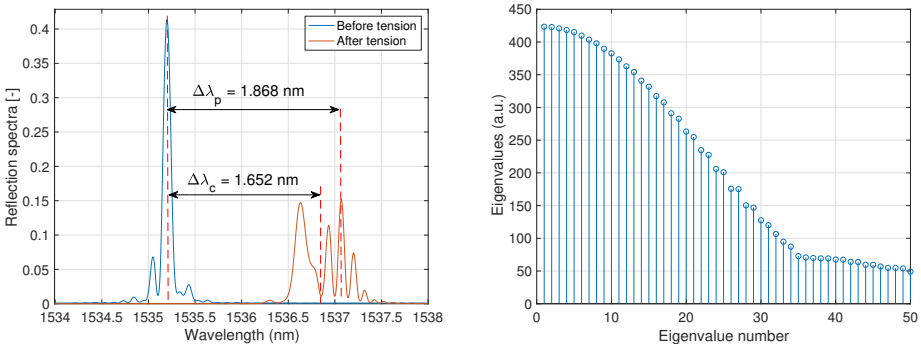

(a) (b)

Figure 4.5: (a): The reflection spectra under no tension (in blue) and under tension (in red). The difference between the shift of the peak wavelength and centres of masses of the two reflection spectra is annotated on the figure. (b): The first 50 eigenvalues of the toeplitz matrix of the Fourier transform of the stressed FBG reflection spectrum after applying tension.

experiments, we demonstrated that using the peak tracking demodulation techniques could possibly lead to significant errors of up to a few thousand microstrains in estimating the average of non-uniform strain fields, whereas the centre of mass approach would lead to close to accurate results. Furthermore, even under high noise values on the grating period and on the ac modulation of the refractive index of the core, or when the reflectivity level of the sensor is high, one can use our side-lobes synchronisation method given in Chapter 3 to compensate for the remaining average strain error accurately.

REFERENCES

[1] W. Zhang, W. Chen, X. Lei, and C. Wang, "Accuracy evaluation of demodulation results of fiber Bragg grating sensors," *Applied Optics*, vol. 56, no. 33, pp. 9212–9220, 2017.

[2] L. Negri, A. Nied, H. Kalinowski, and A. Paterno, "Benchmark for peak detection algorithms in fiber Bragg grating interrogation and a new neural network for its performance improvement," *Sensors*, vol. 11, no. 4, pp. 3466–3482, 2011.

[3] C. G. Askins, M. A. Putnam, and E. J. Friebele, "Instrumentation for interrogating many-element fiber Bragg grating arrays," in *Smart Structures and Materials 1995: Smart Sensing, Processing, and Instrumentation*, vol. 2444, pp. 257–266, International Society for Optics and Photonics, 1995.

[4] S. D. Dyer, P. A. Williams, R. J. Espejo, J. D. Kofler, and S. M. Etzel, "Fundamental limits in fiber Bragg grating peak wavelength measurements," in *17th International Conference on Optical Fibre Sensors*, vol. 5855, pp. 88–93, International Society for Optics and Photonics, 2005.

[5] A. D. Kersey, M. A. Davis, H. J. Patrick, M. LeBlanc, K. Koo, C. Askins, M. Putnam,

and E. J. Friebele, "Fiber grating sensors," *Journal of Lightwave Technology*, vol. 15, no. 8, pp. 1442–1463, 1997.

[6] A. Lamberti, S. Vanlanduit, B. De Pauw, and F. Berghmans, "A novel fast phase correlation algorithm for peak wavelength detection of fiber Bragg grating sensors," *Optics Express*, vol. 22, no. 6, pp. 7099–7112, 2014.

[7] D. Tosi, "KLT-based algorithm for sub-picometer accurate FBG tracking with coarse wavelength sampling," *IEEE Photonics Technology Letters*, vol. 27, no. 20, pp. 2134–2137, 2015.

[8] Y. Okabe, T. Mizutani, S. Yashiro, and N. Takeda, "Detection of microscopic damages in composite laminates," *Composites Science and Technology*, vol. 62, no. 7, pp. 951–958, 2002.

[9] A. Rajabzadeh, R. Heusdens, R. C. Hendriks, and R. M. Groves, "Characterisation of transverse matrix cracks in composite materials using fibre Bragg grating sensors," *Journal of Lightwave Technology*, 2019.

[10] S. Takeda, Y. Okabe, and N. Takeda, "Monitoring of delamination growth in CFRP laminates using chirped FBG sensors," *Journal of Intelligent Material Systems and Structures*, vol. 19, no. 4, pp. 437–444, 2008.

[11] A. Rajabzadeh, R. Heusdens, R. C. Hendriks, and R. M. Groves, "Calculation of the mean strain of smooth non-uniform strain fields using conventional FBG sensors," *Journal of Lightwave Technology*, vol. 36, no. 17, pp. 3716–3725, 2018.

[12] A. Rajabzadeh, R. C. Hendriks, R. Heusdens, and R. M. Groves, "Analysis of FBG reflection spectra under anti-symmetrical strain distributions using the approximated transfer matrix model," in *Optical Sensing and Detection V*, vol. 10680, p. 106800O, International Society for Optics and Photonics, 2018.

[13] M. Yamada and K. Sakuda, "Analysis of almost-periodic distributed feedback slab waveguides via a fundamental matrix approach," *Applied Optics*, vol. 26, no. 16, pp. 3474–3478, 1987.

[14] T. Erdogan, "Fiber grating spectra," *Journal of Lightwave Technology*, vol. 15, no. 8, pp. 1277–1294, 1997.

[15] R. Kashyap, *Fiber Bragg gratings*. Academic Press, 2009.

[16] D. Tosi, "Review and analysis of peak tracking techniques for fiber Bragg grating sensors," *Sensors*, vol. 17, no. 10, p. 2368, 2017.

5

A Method for Determining the Length of FBG Sensors Accurately

It would have been so pointless to kill himself that,
even if he had wanted to, the pointlessness
would have made him unable.

Franz Kafka, The Trial

In this chapter a method will be proposed for estimating the length of single mode fibre Bragg grating type sensors with high accuracy. This method is based on calculating the maximum oscillation frequency of the side-lobes of the FBG reflection spectrum. It will be shown that this frequency is independent of the stress field to which the sensor is subjected, and is dependent on the length of the sensor. This method can be used to characterise the gauge length of already installed FBG sensors so that they can provide useful data for engineering models of structural integrity. All the analyses are based on the approximated transfer matrix model, which is a newly developed numerical method for analysis of the FBG reflection spectrum under various stress fields.

5.1. Introduction

Fibre Bragg grating (FBG) sensors are produced by creating a predetermined modulation in the refractive index of the optical fibre's core, for lengths typically between a few millimetres to a few centimetres. This length of refractive index modulation (grating) is the active length of the FBG sensor, which partially reflects certain wavelengths of the input light in

This chapter is published as "A Method for Determining the Length of FBG Sensors Accurately", by A. Rajabzadeh, R. Heusdens, R. C. Hendriks, and R. M. Groves, in IEEE Photonics Technology Letters, vol. 31, no. 2, 197-200, 2019.

the optical fibre. The main application of FBG sensors is in point strain or temperature sensing, and in vibration and pressure sensing [1]. Since FBG sensors are generally only locally sensitive, it is crucial to know the active length of the sensors. Due to the small diameter of the optical fibre (usually in the order of $125\,\mu m$ or less), it is not possible to inspect the position of the sensor and its length without special equipment. Usually, the approximate position of the sensor is marked on the optical fibre by the producing company. However, sometimes the information regarding the exact active gauge length of the sensor is not available, is not accurate enough, or is not reported in the datasheet of the sensor, and once the sensor is embedded in a structure, it is usually impossible to visually inspect the sensor element. In this chapter, a method is proposed to determine the active length of the sensor accurately, and it will be shown that the results are not affected by subjecting the sensors to different stress fields, making the method suitable for on-site and remote length determination applications.

It is already known from the literature that for an unstressed uniform FBG, the oscillation frequency of the side-lobes of the reflection spectrum linearly depends on the length of the FBG [2]. However, to our knowledge, there have not been any studies on analysing the sensitivity of the aforementioned oscillation frequency to parameters other than the FBG length, and also retrieving the length of non-uniformly grated or partially apodized FBG sensors under stress (uniform or non-uniform). The proposed method in this chapter is based on the approximated transfer matrix model presented in 3, which is a model for the analysis of FBG reflection spectra under non-uniform (and uniform) stress fields. A direct result of this model was to show that it is possible to approximate the side-lobes of the FBG reflection spectra with a closed-form representation. From this closed-form expression, it can be seen that the highest oscillation frequency of the side-lobes (which is generally the dominant frequency) linearly depends on the length of the sensor, and the effective refractive index of the fundamental core mode. In this chapter, this phenomenon will be exploited to estimate the length of the sensor, and show the robustness of this approach under non-uniform and transverse stress fields.

5.2. CLOSED FORM APPROXIMATION OF THE SIDE-LOBES OF FBG REFLECTION SPECTRUM

In Chapter 3 we showed that for any type of FBG sensor, for wavelengths λ that are sufficiently far away from the Bragg wavelength λ_B, the reflection spectrum can be approximated by

$$R(\lambda) \approx \left| \sum_{i=1}^{M-1} (\xi_i - \xi_{i+1})\, e^{-j\left((M-2i)\alpha + \sum_{k\leq i}\alpha_k - \sum_{k>i}\alpha_k\right)} + \left(\xi_M e^{jM(\alpha-\bar{\alpha})} - \xi_1 e^{-jM(\alpha-\bar{\alpha})} \right) \right|^2, \quad (5.1)$$

where $\bar{\alpha} = \sum_{i=1}^{M} \alpha_i / \mathrm{M}$, $\xi_i = \frac{\kappa_i \Delta z}{2j(\alpha-\alpha_i)}$, κ_i is the coupling coefficient between the i'th and the $(i-1)$'th segment, and α and α_i are defined in Section 3.3. The particular λ range in which the approximation in Eq. (5.1) holds, corresponds to the side-lobes of the reflection spectra.

As seen from Eq. (5.1), the maximum oscillation frequency of the side-lobes of the FBG reflection spectrum is $2M\alpha$, and all the other harmonics that appear in the side-lobes have lower oscillation frequencies. The $2M\alpha$ harmonic always has a fairly high amplitude,

especially in wavelength regions where the $(\xi_i - \xi_{i+1})$ terms in Eq. (5.1) are sufficiently damped. In this region, which is associated with side-lobes with lower amplitudes, the dominant harmonic in Eq. (5.1) will be $2M\alpha$, and Eq. (5.1) can be approximated as (see Section 3.4.1)

$$R(\lambda) \approx |\xi_1|^2 + |\xi_M|^2 - 2\mathrm{Re}[\xi_1 \xi_m^*] \cos(2M(\alpha - \bar{\alpha})). \tag{5.2}$$

In Eq. (5.2) all the lower frequency harmonics that result from imperfections in the production of the sensor, and from the non-uniform stress field to which the sensor is subjected, have been neglected. As mentioned before, it can be seen from Eq. (5.2) that the dominant oscillating term is $\cos(2\pi 2Mn_{\mathrm{eff}}\Delta z(\frac{1}{\lambda} - \frac{1}{\bar{\lambda}}))$. Therefore, considering the fact that $L = M\Delta z$, the maximum oscillation frequency is $f_{\max} = 2Ln_{\mathrm{eff}}$, which only depends on the length of the sensor L and the effective refractive index of the core. The proposed method of determining the length of FBG sensors is based on exploiting this phenomenon and retrieving the length of the sensor from this maximum oscillation frequency. However, it is first needed to analyse the sensitivity of "$f_{\max}$" to the effective refractive index of the core.

5.3. FBG LENGTH DETERMINATION

Commercial FBG sensors are usually inscribed in single mode optical fibres, whose effective refractive index are usually in the order of $n_{\mathrm{eff}} \approx 1.45$. In fact, the most common optical fibre for FBG inscription is the SMF28 with $n_{\mathrm{eff}} \approx 1.447$ [3]. An example of a fibre with a higher refractive index is the PR2008 fibre with $n_{\mathrm{eff}} \approx 1.453$ [3]. As it can be seen from these values, the difference between the initial effective refractive index of different types of single mode optical fibres are less than 0.2%. Furthermore, during the inscription of the gratings on an optical fibre, the changes of the refractive index of the fundamental core mode is less than $\Delta n_{\mathrm{DC}} \leq 2.5 \times 10^{-3}$, even under long exposure times and high input impulse energies [4]. This DC effective refractive index change is significantly larger for sensors that are produced by exposure to femto-second laser pulses. They are in the order of around $\Delta n_{\mathrm{DC}} \leq 6 \times 10^{-3}$ [5]. This means that the sensitivity of the dominant oscillation frequency in Eq. (5.2) to the variations of the refractive index of the core is less than 1%. Therefore, without having any knowledge about the type of the optical fibre in use, the exposure time or the pulse energy of the FBG production process, or even the method of production, the maximum error in length determination that is introduced by setting a conventional fixed value for n_{eff} is at most less than 1%. This will make the method reliable for blind measurements of the length of FBG sensors, without any prior knowledge about the origin of the sensor.

Another factor that needs to be considered here is the effect of transverse loads and birefringence effects. Birefringence can be caused by external perturbations such as transverse loads or bending of the fibre. In addition, birefringence can affect the FBG sensor during production. In either scenario, the result is that the propagating light along the length of the fibre experiences different refractive indices along the slow and fast polarisation axes. Under these conditions, the overall reflection spectrum of the disturbed FBG will be

$$R(\lambda) = R_x(\lambda) + R_y(\lambda), \tag{5.3}$$

where R_x is the reflection spectrum along the x-axis and R_y is the reflection spectrum along the y-axis. In both of these polarisation axes, the maximum oscillation frequency is still

equal to $2Ln_{\text{eff}}$. Therefore, the maximum frequency of the side-lobes of the summation term given in Eq. (5.3) will also be equal to $2Ln_{\text{eff}}$.

Based on the discussions above, it can be concluded that by inspection of the maximum frequency of the side-lobes of the FBG reflection spectra, it is possible to retrieve the length of the sensor, as this frequency linearly depends on the length of the sensor. This approach is rather insensitive to the external media to which the sensor is subjected and other physical properties of the sensor. The proposed method of retrieving the length of the FBG is simply to take the Fourier transform of the side-lobes of the FBG reflection spectrum, and to determine the maximum frequency at which the amplitude of the Fourier transform is above the noise level. In other words, by taking the Fourier transform of Eq. (5.2) and the cosine term within this equation, we expect to find high amplitude harmonics at $\delta(f \pm 2Ln_{\text{eff}})$ frequencies. Note that as mentioned before, in the side-lobes, this maximum oscillation frequency is the dominant term, and its amplitude is also relatively large compared to the lower oscillation frequencies. The identification of this dominant peak is based on its amplitude, which should be comparable to the lower frequency components and above a noise floor that can be determined based on the physical properties of the sensor and the interrogator.

5

5.4. RESULTS AND DISCUSSION

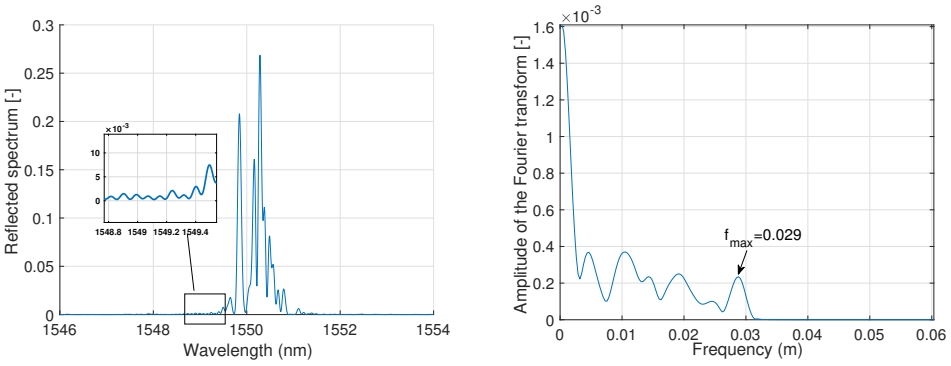

Figure 5.1: (a) A simulated FBG sensor with refractive index fluctuations under an extremely non-uniform strain field, with both transverse and axial components, and (b) Fourier transform of the side-lobes given in (a).

In this section we validate the proposed method for determining the length of FBG sensors using two experiments. In the first experiment, which is a computer simulation, an FBG sensor with a nominal length of 10 mm was designed, and a non-uniform stress was applied on it with both axial and transverse components. We also included imperfections to the designed sensor by adding fluctuations in the refractive index of the core. The resulting reflection spectrum is shown in Fig. 5.1a. Fig. 5.1b shows the amplitude of the Fourier transform of the side-lobes of this sensor (denoted by the zoomed-in rectangle in Fig. 5.1a). Note that the oscillation terms in Eq. (5.2) are described in "α" or "$1/\lambda$" domain, therefore, the unit on the x-axis of its Fourier transform will be in metres.

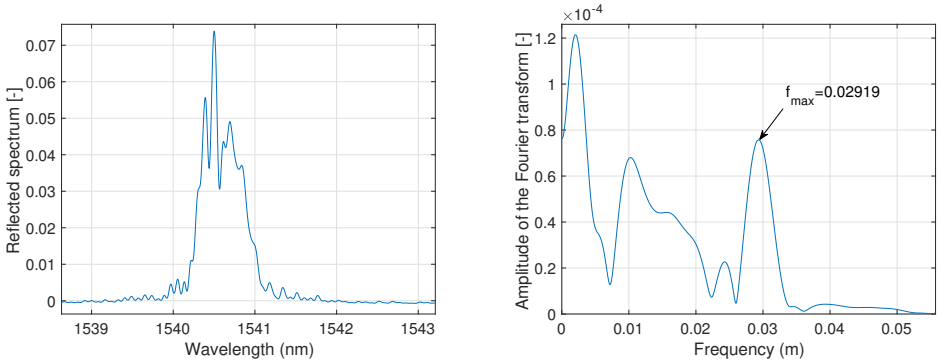

(a) (b)

Figure 5.2: (a) Reflection spectrum of an actual FBG sensor under an extremely non-uniform strain field, with both transverse and axial components, and (b) Fourier transform of the side-lobes given of the reflection spectrum.

It can be seen from the figure that the maximum dominant frequency in the Fourier transform is at $f_{\max} = 0.029\,\text{m}$, therefore, the length calculated based on this frequency and the given effective refractive index ($n_{\text{eff}} = 1.4469$) is $\tilde{L} = f_{\max}/(2n_{\text{eff}}) = 0.01002\,\text{m}$ or 10.02 mm. The error of calculation in this example is therefore around 0.2%.

In the second example, the method was tested on a real FBG sensor. Fig. 5.2a shows the reflection spectrum of a draw tower grating (DTG) sensor with a nominal length of 10 mm under an arbitrary non-uniform strain field, with components in both axial and transverse directions. The FBG sensor used in this experiment is partially apodized, with a side-lobe suppression ratio of 10 dB. The FBG sensor was interrogated with a PXIe 4844 interrogator from National Instruments with a spatial resolution of 4 pm and dynamic range of 40 dB. The amplitude of the Fourier transform and the maximum frequency are shown in Fig. 5.2b.

The same sensor underwent several other load scenarios, where the sensor was subject to various arbitrary transverse and axial loads. Those results are summarised in Table 5.1. As it is evident from this table, the location of the highest oscillating harmonic barely changes under different force loads. In these calculations, the presumed effective refractive index of the core was $n_{\text{eff}} = 1.447 + 2 \times 10^{-3} = 1.449$, which was based on the assumption that the optical fibre has similar properties to the SMF28 fibre, with a DC offset of 2×10^{-3} due to being exposed to UV light.

Based on the length estimation results, the standard deviation of the estimated length is around 0.01 mm. Furthermore, since there can always be fluctuations on the specified nominal length of the sensor in the datasheet, a more accurate reference was needed for the validation of the proposed method by locating the exact position of the sensor along the fibre length. The most accurate method that could offer a better accuracy than the specified nominal length was to put the optical fibre under the microscope, and to locate the gratings along the fibre length. However, due to the small refractive index modulation of the DTG sensors and the small diameter of their core, it was impossible to locate the gratings through the cladding and the coating layer. Therefore, first the Ormocer coating of the fibre was removed using a thermal stripper, and then the fibre was chemically etched off

Table 5.1: **FBG sensor under different stress fields, the resulting maximum oscillation frequency, and the resulting estimated sensor length.**

Stress field	Maximum oscillation frequency (m)	Estimated sensor length (mm)
Unstressed sensor	0.02922	10.0828
Load scenario #1	0.02919	10.0725
Load scenario #2	0.02925	10.0932
Load scenario #3	0.02919	10.0725
Load scenario #4	0.02916	10.0621
Load scenario #6	0.02922	10.0828

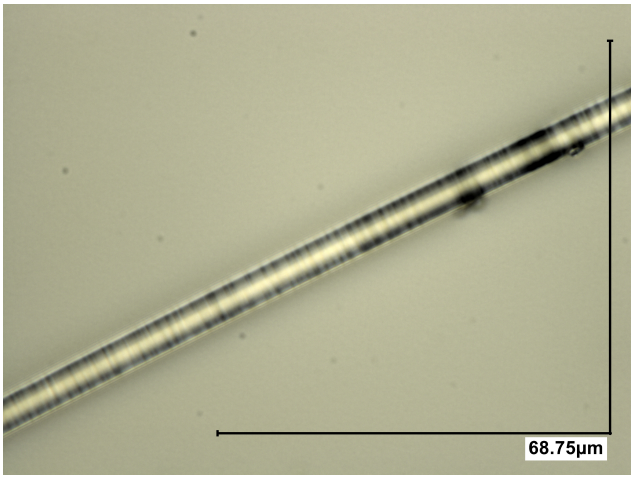

Figure 5.3: A small part of the gratings structure of the optical fibre's core under an optical microscope.

its cladding layer in order to be left with only the core of the fibre. For the etching process, a solution of 15 wt% of NH_4F and 16 wt% of H_2SO_4 [6] was used, and the sensor part of the optical fibre with an original diameter of 125 μm was submerged in the solution for a period of around 5 hours, during which time the diameter was reduced to around 10 μm. Afterwards, the etched fibre was put under an optical microscope with a magnification of around 2500 in order to locate the FBG length. Fig. 5.3 shows a small part of the grating under the microscope. Based on the microscopy results, the overall length of the sensor with significant variations in its refractive index was determined as 10.093 mm. Based on the reference values for the FBG length, in this particular example, our method offers a better accuracy for the FBG length, even compared to the datasheet of the sensor, with a maximum error of around 0.3 %.

It is noteworthy that the proposed method could potentially perform well for other types of short Bragg grating sensors too, as long as a high dynamic range interrogator is being used and the side-lobes have not been deliberately fully suppressed (such as Gaussian apodized sensors [1]). Nevertheless, the proposed method works perfectly well for partially

apodized FBG sensors, as well as non-apodized FBG sensors. Furthermore, it can be employed for length determination of chirped FBG sensors [1], phase shifted FBG structures, and for other types of aperiodic grating structures as well.

5.5. CONCLUSIONS

In this chapter, it was shown that the length of conventional FBG sensors can be estimated based on calculating the maximum oscillation frequency of the side-lobes of the FBG reflection spectrum. It was shown that this oscillation frequency is independent of the stress (or temperature) field to which the sensor is subjected, and that its sensitivity to the variations of the effective refractive index of the core is negligible, making the method reliable for FBG length determination without having a prior knowledge about the production method, optical fibres in use and etc. Furthermore, the results of the proposed method can be extended to other types of non-uniform gratings and partially apodized FBG sensors. Computer simulations and experimental measurements were used to validate the proposed method, and the results were in line with our expectations on the presented model.

REFERENCES

[1] A. D. Kersey, M. A. Davis, H. J. Patrick, M. LeBlanc, K. P. Koo, C. G. Askins, M. A. Putnam, and E. J. Friebele, "Fiber grating sensors," Journal of Lightwave Technology, vol. 15, pp.1442-1463, 1997.

[2] T. Erdogan, "Fiber grating spectra," Journal of Lightwave Technology, vol. 15, no. 8, pp. 1277-1294, 1997.

[3] F. Juelich, J. Roths, "Determination of the Effective Refractive Index of Various Single Mode Fibres for Fibre Bragg Grating Sensor Applications," Proc. OPTO 2009 & IRS^2, pp. 119–124, 2009.

[4] M. Bernier, S. Gagnon, R. Vallée, "Role of the 1D optical filamentation process in the writing of first order fiber Bragg gratings with femtosecond pulses at 800nm," Optical Materials Express, vol. 1, no. 5, pp. 832-844, 2011.

[5] E. Fertein, C. Przygodzki, H. Delbarre, A. Hidayat, M. Douay, P. Niay, "Refractive-index changes of standard telecommunication fiber through exposure to femtosecond laser pulses at 810 nm," Applied Optics, vol. 40, no. 21, pp. 3506-3508, 2001.

[6] S. Ko, J. Lee, J. Koo, B. S. Joo, M. Gu, and J. H. Lee, "Chemical wet etching of an optical fiber using a hydrogen fluoride-free solution for a saturable absorber based on the evanescent field interaction," Journal of Lightwave Technology, vol. 34, no. 16, pp. 3776-3784, 2016.

6

A Method for Determining the Position of FBG Sensors Accurately

Three o'clock is always too late or
too early for anything you want to do.

Jean-Paul Sartre, Nausea

Fibre Bragg grating sensors have gained a lot of attention in damage detection and strain measurement applications in the past few decades. These applications include matrix crack detection and delamination tip monitoring in composite structures, crack detection in concrete and civil engineering structures and etc. The damage localisation accuracy of such methods, directly depends on precise knowledge on the position of the FBG sensor. However, this information is not commonly provided by manufacturing companies with such accuracy. In this chapter, a novel approach will be presented to accurately determine the position of an FBG sensor with a low complexity setup. The proposed method offers an accuracy of below $10\,\mu m$, and can consequently increase the spatial resolution of damage detection methods.

6.1. Introduction

Fibre Bragg grating (FBG) sensors are typically used in point strain and temperature measurement applications [1, 2]. In recent years, the application of FBG sensors in damage detection of a variety of materials and structures has gained a lot of attention as well [3–5]. Due to the small diameter and low weight of these sensors, they can be embedded between

This chapter is published as "A Method for Determining the position of FBG Sensors Accurately", by A. Rajabzadeh, R. C. Hendriks, R. Heusdens, and R. M. Groves, in the proceedings of the Seventh European Workshop on Optical Fibre Sensors (EWOFS), 11199, 111990U, 2019

the layers of composite structures, and provide useful information about the structural integrity of the internal layers of the composite material [6].

In all the above mentioned applications, it is essential to know the precise position of the FBG sensor along the optical fibre, so that it provides useful data for engineering models of structural integrity. For instance, using the FBG sensors in the detection of barely visible matrix cracks in composites [3, 5], or monitoring the growth and progress of delaminated composite layers, the knowledge of the precise location of the cracks or the delamination tip [4] can be very useful in studying the fatigue and stress behaviour of composites. The accuracy of damage localisation and progression in these applications directly depends on having a precise knowledge of the exact position of the FBG sensor. However, when the FBG is received from the manufacturer, there is usually ambiguity in the exact position of the FBG, as the sensor markings only indicate the approximate position of the sensor. For some manufacturing methods (e.g. strip and recoat method), it is possible to achieve higher accuracies using more precise translation stages, but the production costs increase significantly.

In this chapter, a method will be presented for the localisation of the exact position of the FBG with a high accuracy. This method is non-invasive and can be utilised at very low complexity, its labour intensity is minimal, and it does not risk the health and the integrity of the optical fibre. The most common alternative to this approach is using a rolling pin over the FBG length, and observe the changes in the reflection spectrum, marking the starting point and ending point of observing changes in the reflection spectrum. However, this method is labour intensive, and its accuracy could be low, since for approximately the first 1 mm of the sensor length, the changes in the reflection spectrum are negligible, and might be confused with different noise sources. The proposed method is based on mechanically exciting two arbitrary points along the FBG length, and analysing the side-lobes of the FBG reflection spectrum under that momentary stress. For this purpose, the closed form representation of the reflection spectrum that is derived from the approximated transfer matrix method will be used [7].

6.2. PROBLEM FORMULATION

When an FBG sensor experiences a non-uniform strain field (or grating structures), its reflection spectrum can be calculated using numerical methods such as the transfer matrix model [2]. In such cases, it is assumed that the length L of the FBG sensor is divided into M piece-wise uniform segments, each undergoing a uniform strain field. In Section 3.4.1, we showed that under non-uniform strain fields, the reflection spectrum R of the FBG sensor can be approximated as

$$R(\alpha) \approx \left| \sum_{i=1}^{M} \kappa_i \Delta z \,\mathrm{sinc}(\alpha - \alpha_i) e^{-j\left((M-2i+1)\alpha + \sum_{k<i} \alpha_k - \sum_{k>i} \alpha_k\right)} \right|^2, \tag{6.1}$$

in which the κ_i's are the coupling coefficients between the forward and backward electric waves, and α and α_i are given by

$$\alpha = \frac{2\pi n_{\text{eff}} \Delta z}{\lambda} \quad \text{and} \quad \alpha_i = \frac{2\pi n_{\text{eff}} \Delta z}{\lambda_i}, \tag{6.2}$$

respectively. Here, λ is the wavelength region under interrogation, λ_i is the local Bragg wavelength of the i'th segment, and n_{eff} is the effective mode index of the core. In Chapter 5 we showed that there is a linear relationship between the active gauge length of the FBG (even under extremely non-uniform stress fields) and the maximum harmonic frequency of Eq. (6.1). This approach was used to accurately calculate the active gauge length of the FBG sensor. By rearranging the terms in Eq. (6.1), we showed that the complex reflection spectrum can be presented as [7]

$$r(\alpha) = \sum_{i=1}^{M-1} \overbrace{(\xi_i - \xi_{i+1})}^{\zeta_i} e^{-j\left((M-2i)\alpha + \sum_{k\le i}\alpha_k - \sum_{k>i}\alpha_k\right)} + \left(\xi_M e^{jM(\alpha-\bar{\alpha})} - \xi_1 e^{-jM(\alpha-\bar{\alpha})}\right), \tag{6.3}$$

where

$$\xi_i = \frac{\kappa_i \Delta z}{2j(\alpha - \alpha_i)}. \tag{6.4}$$

In this chapter, the focus will be on the $\zeta_i = \xi_i - \xi_{i+1}$ terms given in Eq. (6.3). As shown in Section 3.4.1, when there is a smooth stress field over the length of the FBG, the values of ζ_i will be negligible, and the first summation term in Eq. (6.3) can be neglected. On the other hand, if there is a drastic change in the stress or grating distribution at a certain segment of the FBG model, the values of ζ_i at that particular segment will not be negligible anymore. In this work, this principle will be exploited in order to determine the position of the FBG sensor. We put stress at arbitrary (controlled) points along the FBG length, which results in large ζ_i values at the excited segments. As seen from Eq. (6.3), large values of ζ_i result in powerful harmonics at the angular frequency $\omega = M - 2i$ in the complex reflection spectrum. The frequency of such an harmonic is thus directly related to the point of excitation. By finding the precise position of the excitations along the FBG length, the exact position of the sensor can be derived as well. Since in most applications only the amplitude of the reflection spectrum is available, we first need to expand Eq. (6.3). For that purpose, suppose there is only one mechanical excitation at segment t of the FBG model (which means large values for ζ_i at $i = t$), with which, as presented in Section 3.4.1, the following will be obtained

$$\begin{aligned} R(\alpha) = |r(\alpha)|^2 \approx \sum_{i=1}^{M-1} |\zeta_i|^2 + 2\,\text{Re}[\zeta_t \zeta_M^*]\cos\left((2M-2t)\alpha + \theta_t - M\bar{\alpha}\right) \\ -2\,\text{Re}[\zeta_t \zeta_1^*]\cos\left((2t)\alpha - \theta_i - M\bar{\alpha}\right) + R_r + R_s, \end{aligned} \tag{6.5}$$

where

$$R_s \approx |\xi_1|^2 + |\xi_M|^2 - 2\,\text{Re}[\xi_1 \xi_M^*]\cos(2M(\alpha - \bar{\alpha})) \tag{6.6}$$

refers to the reflection spectrum under a smooth strain field, and R_r is the summation of all remaining terms from the expansion (with lower amplitudes than the other terms in Eq. (6.5)). Note that the information regarding the length of the sensor is in R_s, as the oscillating term in R_s is $\cos(2\pi 2M\Delta z n_{\text{eff}}(1/\lambda - 1/\bar{\lambda}))$, which linearly depends on $L = M\Delta z$. In fact, this term has the highest oscillation frequency among all the harmonics presented

in Eq. (6.5), with a value of $f_{\max} = 2Ln_{\text{eff}}$, from which the exact length of the sensor can be retrieved [8].

As seen from Eq. (6.5), for a single excitation of the FBG at segment t, two new harmonics will emerge in the reflection spectrum with angular frequencies $\omega = 2M-2t$ and one at $\omega = 2t$. This means that with a single excitation, one cannot determine the exact location of the excitation, as there will be a reflection line of symmetry ambiguity in localising the excitation. In other words, exciting the sensor at segment t results in the same harmonics as exciting it at segment $M - t$.

In order to overcome this ambiguity, we propose exciting the FBG length at two (or more) locations, and at different time instances, wherein the distance between the excitations is fixed and known. Assume the first excitation is applied at an arbitrary segment, and by inspection of the Fourier transform of the reflection spectrum, we see that the newly generated harmonics have angular frequencies at $\omega = 2t$ and $\omega = 2M - 2t$. With this single excitation, it can deduced that the sensor was stressed either at segment t, or at segment $M - t$. Now, another excitation is applied over the sensor at a known distance of l segments from the first excitation. If the second set of new harmonics are at $\omega = 2(t + l)$ and $\omega = 2M - 2(t + l)$, it means that the first excitation was at the t'th segment. Otherwise, if new harmonics are seen at $\omega = 2(M - t + l)$ and $\omega = 2(t - l)$, it means that the first excitation was at the $(M - t)$'th segment. The ambiguity of the excitation point is thus resolved. Moreover, the exact length of the sensor can be retrieved using the method presented in Chapter 5, which determines the overall number of segments M in the FBG model. With the knowledge of the accurate length of the sensor, and the exact excitation segment, the precise start and end point of the sensor can be determined.

The accuracy of this method depends on the width of the excitation, and the narrower the width of the excitation (or the finer the FBG segmentation), the more accurate the localisation accuracy. As a practical example, using small diameter Tungsten wires, excitation points with a width of $10\,\mu m$ can be implemented, using which, a localisation accuracy of $10\,\mu m$ can be achieved. Moreover, by increasing the number of measurements, and averaging the results, the accuracy of the method can be further improved.

6.3. IMPLEMENTATION

There are several ways to induce the aforementioned local excitations along the FBG length. It can be purely mechanical, using piezo-electric actuators [9], or by locally heating the FBG sensor. In this chapter, the latter option was chosen, as it is more easily controllable (in terms of the setup itself, and the width of the excitation). The difference between the mechanical and the thermal excitation is that in the thermal option, the thermo-optic effect is much more dominant than the thermal expansion effect. In fact, the contribution of the thermal expansion to the overall local phase shift has been shown to be around 10% of that of the thermo-optic effects [10]. In such a case, the main effect of locally heating the FBG at segment t is that the effective mode index of the core at that particular segment increases, since $\Delta n_{\text{eff}_t} = a\Delta T$, where a is the thermo-optic coefficient. A qualitative assessment (which is sufficient for the current chapter) suggests that

$$\Delta n_{\text{eff}_t} \uparrow \Rightarrow \Delta\alpha_t \uparrow \Rightarrow \Delta\xi_t \uparrow \Rightarrow \Delta\zeta_t \uparrow . \tag{6.7}$$

It is noteworthy that by mechanically exciting segment t of the FBG, the same effect as Eq. (6.7) will be induced, except that the origin of the change will be from the local expansion of the FBG at segment t or $\Delta\lambda_t$. With that, the suggested setup for determining the precise position of an FBG sensor is shown in Fig. 6.1.

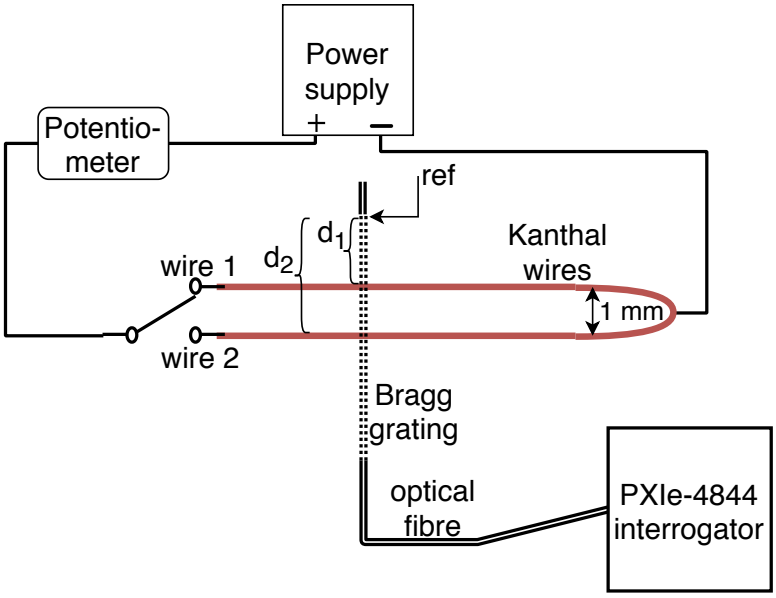

Figure 6.1: The setup used for determination of the position of the FBG sensor. The manual switch determines which of the two Kanthal wires, denoted by wire 1 and wire 2, will be connected to the power supply. "ref" denotes the starting point of the sensor, and d_1 and d_2 are the distances of wire 1 and wire 2 from the "ref" point, respectively.

In this setup, the Kanthal wires had a diameter of $300\,\mu m$, and we passed around 1 A of current through each of them to heat them up for short periods of time, resulting in temperature changes of around 250 °C. The FBG used in this chapter was a partially apodized DTG type sensor from FBGS company, with a Bragg wavelength of 1550 nm and a nominal length of 8 mm. The PXIe-4844 interrogation unit has a wavelength accuracy of 4 pm, and a dynamic range of 40 dB. The objective of this experiment is to determine lengths d_1 and d_2, shown in Fig. 6.1. Also note that by design $d_2 \approx d_1 + 1$ mm. Since the relative location of the two Kanthal wires are already known, the starting point of the sensor, depicted by "ref" in the figure, can be determined.

In order to analyse the reflection spectrum side-lobes given in Eq. (6.5), a Hann window was applied on the reflection spectrum, starting at the centre of mass of the reflection spectrum, given by

$$\lambda_{B_c} = \frac{\int_\lambda \lambda R(\lambda) \mathrm{d}\lambda}{\int_\lambda R(\lambda) \mathrm{d}\lambda}, \tag{6.8}$$

where λ is the wavelength region under investigation. The upper bound was chosen by setting a threshold on the amplitude of the reflection spectrum, and truncating the spectrum

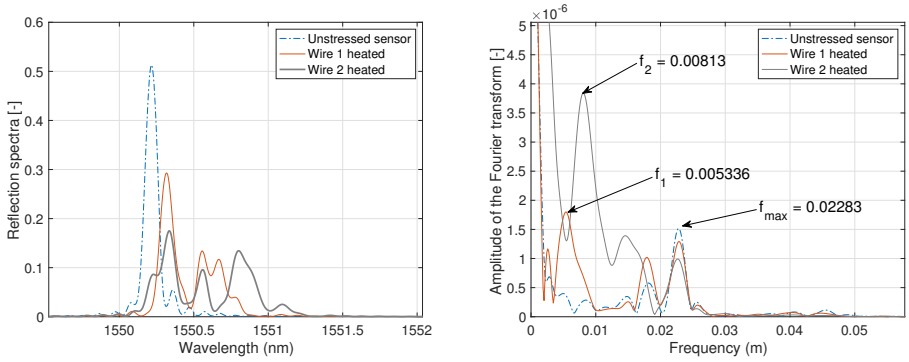

(a) (b)

Figure 6.2: (a): Reflection spectrum from a healthy FBG, along with the reflection spectra of the same sensor when wire 1 and wire 2 were heated. (b): The associated Fourier transform of the windowed side-lobes.

outside this interval. This threshold value can be determined by the physical setup of the interrogator and the sensor used, and it is based on the noise floor (in the wavelength domain) when the sensor is connected to the interrogator. In this chapter, we assumed a threshold equal to 2 times the maximum amplitude of the noise floor. Fig. 6.2a shows the reflection spectra of the sample DTG sensor in Fig. 6.1, in three different time instances associated with the unstressed sensor, and with heating of the two Kanthal wires. Applying the Hann window on the reflection spectrum, and taking the Fourier transform of the side-lobes results in the graphs of Fig. 6.2b. Note that in Fig. 6.2b, the 'x' axis is scaled by a factor of Δz, and thus, the retrieved distances will be in 'mm' rather than segment numbers.

It can be seen from Fig. 6.2b that the retrieved length of the sensor in this example is $L = f_{\max}/(2n_{\text{eff}}) = 7.8892$ mm [8]. In the first instance of locally heating the FBG via wire 1, the emerging harmonics are at $f_1 = 0.005336$ m and $f_1' = 0.0177$ m. Note the symmetry of the location of the new harmonics with respect to the central frequency in the Fourier domain at $f_c = f_{\max}/2 = 0.0114$ m. From this first measurement, it can be deduced that wire 1 is either at $d_1 = f_1/(2n_{\text{eff}}) = 1.8439$ mm or at $d_1' = f_1'/(2n_{\text{eff}}) = 6.1165$ mm distance from the reference point "ref". By inspection of the FBG reflection spectrum when locally heated via wire 2, the retrieved distance of wire 2 from the reference point is either $d_2 = f_2/(2n_{\text{eff}}) = 2.8094$ mm or $d_2' = f_2'/(2n_{\text{eff}}) = 5.0901$ mm. Based on these two measurements, and taking into account the fact that $d_2 \approx d_1 + 1$ mm, it can be concluded that $d_1 = 1.8439$ mm and $d_2 = 2.8094$ mm, and the precise location of the "ref" point (start point of the sensor) is determined to be at a distance of d_1 from wire 1.

6.4. CONCLUSIONS AND DISCUSSIONS

In this chapter, it was shown that using two sets of measurements in a controlled setup of locally exciting arbitrary points of an FBG sensor, the precise position of the FBG can be retrieved. Such accurate information is beneficial in damage detection type applications of FBG sensors, to provide information about the location of the damage (matrix cracks of delamination tip) with a high spatial resolution. The proposed method can also be used for

accurate marking of the sensor position on optical fibres during their production as well. Furthermore, by altering the setup to simultaneous excitations of the two Kanthal wires at different distances from each other, our method can work for fully apodized FBG sensors as well.

REFERENCES

[1] E. Udd, W. B. Spillman Jr, "Fiber Optic Sensors: An Introduction for Engineers and Scientists," John Wiley & Sons, 2011.

[2] T. Erdogan, "Fiber grating spectra," *Journal of Lightwave Technology*, vol. 15, no. 8, pp. 1277-1294, 1997.

[3] Y. Okabe, T. Mizutani, S. Yashiro, N. Takeda, "Detection of microscopic damages in composite laminates," *Composites Science and Technology*, vol. 62, no. 7, pp. 951-958, 2002.

[4] S. Takeda, Y. Okabe, N. Takeda, "Monitoring of delamination growth in CFRP laminates using chirped FBG sensors," *Journal of Intelligent Material Systems and Structures*, vol. 19, no. 4, pp. 437-444, 2008.

[5] A. Rajabzadeh, R. Heusdens, R. C. Hendriks, R. M. Groves, "Characterisation of Transverse Matrix Cracks in Composite Materials Using Fibre Bragg Grating Sensors," *Journal of Lightwave Technology*, vol. 37, no. 18, pp. 4720-4727, 2019.

[6] A. D. Kersey, M. A. Davis, H. J. Patrick, M. LeBlanc, K. P. Koo, C. G. Askins, M. A. Putnam, and E. J. Friebele, "Fiber grating sensors," *Journal of Lightwave Technology*, vol. 15, no. 8, pp. 1442-1463, 1997.

[7] A. Rajabzadeh, R. Heusdens, R. C. Hendriks, and R. M. Groves, "Calculation of the mean strain of smooth non-uniform strain fields using conventional FBG sensors," *Journal of Lightwave Technology*, vol. 36, no. 17, pp. 3716-3725, 2018.

[8] A. Rajabzadeh, R. Heusdens, R. C. Hendriks, R. Groves, "A Method for Determining the Length of FBG Sensors Accurately," *IEEE Photonics Technology Letters* vol. 31, no. 2, pp. 197-200, 2019.

[9] J. Palaci, P. Perez-Millan, G. E. Villanueva, J. L. Cruz, M. V. Andres, J. Marti, B. Vidal, "Tunable photonic microwave filter with single bandpass based on a phase-shifted fiber Bragg grating," *IEEE Photonics Technology Letters*, vol. 22, no. 19, pp. 1467-1469, 2010.

[10] Z. Zhang, C. Tian, M. R. Mokhtar, P. Petropoulos, D. J. Richardson, M. Ibsen, "Rapidly reconfigurable optical phase encoder-decoders based on fiber Bragg gratings," *IEEE Photonics Technology Letters*, vol. 18, no. 11, pp. 1216-1218, 2006.

7

Characterisation of Transverse Matrix Cracks in Composite Materials Using Fibre Bragg Grating Sensors

There was a door to which I found no key:
There was the veil through which I might not see.

Omar Khayyam

In this chapter a novel approach is proposed to characterise barely visible transverse matrix cracks in composite structures using fibre Bragg grating optical sensors. Matrix cracks are one of the most prevalent types of damage in composite structures, and detecting them in the internal layers of composites has remained a challenge. In this chapter, it will be shown that the formation of cracks in the internal layers of composite structures alters the side-lobes of the reflection spectra of FBG sensors by adding new harmonics to them. It is then argued that the spread and the location of these harmonics depends on both the mechanical properties of the composite material and the location of the crack along the length of the FBG sensor. Via computer simulations and experimental measurements these hypotheses were validated, and the results were in agreement with our model.

This chapter is published as "Characterisation of Transverse Matrix Cracks in Composite Materials Using Fibre Bragg Grating Sensors", by A. Rajabzadeh, R. Heusdens, R. C. Hendriks, and R. M. Groves, in IEEE/OSA Journal of Lightwave Technology, vol. 37, no. 18, pp. 4720-4727, 2019

7.1. Introduction

The small diameter of FBG sensors allows them to be embedded between the layers of composite laminates without severely changing the mechanical properties of the composite structure [1]. This makes FBG sensors interesting for structural health monitoring of composite materials. FBG sensors can provide insight into the internal layers of composites, including internal strain and temperature measurements [1], monitoring the behaviour of composites during the curing process [2], and for the detection of cracks and damages [3–5]. Although the main application of FBG sensors has been in the field of point strain and temperature measurements [6, 7], in the last few decades several studies have been carried out on the subject of damage detection in composites, including the most prevalent types of damages in composites such as delamination and matrix cracks.

The current study belongs to the latter category, with a focus on the characterisation of barely visible matrix cracks that occur along the length of embedded FBG sensors within the internal layers of composites. Within this framework, several studies have been conducted in the past few decades. Although most of these methods can potentially distinguish between a uniform and a non-uniform stress field over the composite panel, they lack the capability of differentiating a composite part that is affected by cracks from other sorts of non-uniform stress fields, transverse loads and birefringence effects. In [8], chirped FBG sensors were used for crack detection. It was argued that the formation of cracks along the length of such chirped FBG sensors will result in the emergence of dips and valleys in the reflection spectra. The case of transversal crack formation around holes in composite structures was investigated in [9]. Chambers et al. argued that the shift of the Bragg wavelength of FBG sensors (or equivalently a change in strain) is a measure good enough to detect impact damages and cracks [10]. In [5, 11] Okabe et al. argued that there is an empirical relation between the width of the FBG reflection spectra and the transverse crack density. Based on the modelling that will be presented in this chapter, it will shown that the argumentation on the empirical relation between the width of the FBG reflection spectra and the transverse crack density given in [5, 11] is indeed correct. However, it will shown that a widened FBG reflection spectrum can also be associated with non-uniform stress fields that are not related to transversal cracks. The width of the FBG reflection spectrum can thus not unambiguously be used to indicate the presence of transversal cracks.

In this chapter, the effect of transverse cracks on FBG reflection spectra will be investigated from a new perspective. A mathematical model for the analysis of FBG reflection spectra from sensors that are affected by transverse cracks will be presented, and it will be shown that the information regarding the formation of cracks lies within the side-lobes of these spectra. This hypotheses will be substantiated with both computer simulations and experimental measurements on composite coupons.

7.2. FBG reflection spectra Under Non-uniform Strain Fields

Expanding on the closed-form approximation of the side-lobes of the FBG reflection spectrum, presented in Section 3.4.1, the following will be obtained

$$R(\lambda) \overset{(a)}{\approx} \left| \sum_{i=1}^{M} \kappa_i \Delta z \,\mathrm{sinc}(\alpha - \alpha_i) e^{-j\left((M-2i+1)\alpha + \sum_{k<i}\alpha_k - \sum_{k>i}\alpha_k\right)} \right|^2 \tag{7.1}$$

$$\overset{(b)}{=} \left| \sum_{i=1}^{M-1} \overbrace{(\xi_i - \xi_{i+1})}^{\zeta_i} e^{-j\left((M-2i)\alpha + \sum_{k\leq i}\alpha_k - \sum_{k>i}\alpha_k\right)} + \left(\xi_M e^{jM(\alpha-\bar{\alpha})} - \xi_1 e^{-jM(\alpha-\bar{\alpha})}\right) \right|^2, \tag{7.2}$$

where (a) is obtained by neglecting the products of the sinc functions with the low amplitudes in the F_{11} and F_{21} elements (see [12]), and (b) follows by re-arranging the terms in (7.1). Further,

$$\xi_i = \frac{\kappa_i \Delta z}{2j(\alpha - \alpha_i)}. \tag{7.3}$$

The approximation in Eq. (7.1) is most accurate in the side-lobes of the reflection spectrum (Chapter 3). To analyse the effect of different kinds of strain fields on the reflection spectrum, the focus will be on the ζ_i terms given in Eq. (7.2) as $\zeta_i = \xi_i - \xi_{i+1}$.

From Eq. (7.2) it can be seen that the reflection spectrum is a function of the local Bragg frequencies (α_i), that are a function of the strain field over the length of the sensor, via the following relation [12]

$$\alpha_i = \frac{\rho}{\lambda_i} = \frac{\rho}{\bar{\lambda}_B + \Delta\lambda_i} \approx \bar{\alpha} - \frac{\rho}{\bar{\lambda}_B^2}\Delta\lambda_i = \bar{\alpha} - k_s \frac{\rho}{\bar{\lambda}_B^2} s_i, \tag{7.4}$$

where $\rho = 2\pi n_{\text{eff}} \Delta z$, and $\bar{\lambda}_B^2$ is the mean of all Bragg wavelengths along the length of the sensor, and the s_i's are the local strain values of each segment of the FBG model. Indeed, Eq. (7.4) suggests that a linear shift in the local Bragg wavelengths (or a shift in strain along the FBG length) results in a linear shift in the local Bragg frequencies, i.e., the α_i's.

When the strain field along the length of the FBG sensor is smooth (no discontinuity along the length of the FBG sensor), the ζ_i parameters will be small and the first $M-1$ terms in Eq. (7.2) can be neglected, so that the side-lobes of the reflection spectrum can be approximated by

$$R(\lambda) \approx (\kappa L)^2 \,\mathrm{sinc}^2\left(M(\alpha - \bar{\alpha})\right) + (\xi_M - \xi_1)^2, \tag{7.5}$$

where $\bar{\alpha} = \sum(\alpha_i)/M$, and $L = M\Delta z$ is the sensor length. In other words, the side-lobes of the reflection spectra will only have one dominant oscillating frequency. On the other hand, if the strain field is not smooth and has sharp variations along the FBG length, the ζ_i variables will not be negligible anymore and additional harmonics will appear.

In the next section, the effect of transverse cracks on the strain field along the sensor length will be analysed, the highly non-uniform strain distribution they impose on the FBG sensor, and the consequent large ζ_i values at the crack locations. In Section (7.4) the effect of such large ζ_i values on the frequency content of the side-lobes of the FBG reflection spectra will be investigated.

7.3. Strain Field Under Transverse Cracks

In this section, we will present a model that explains the stress behaviour of composite materials under transverse matrix cracks in their internal layers. Consider an FBG sensor embedded between the layers of a healthy unidirectional carbon fibre reinforced plastic (CFRP) composite structure. Due to the brittle nature of the matrix material, under fatigue or impact damages, matrix cracks could form in the internal layers of composite. Based on McCartney's theory [13], for a composite material with given mechanical properties, the strain distribution along the length of an embedded optical fibre can be analytically calculated. A schematic diagram of a composite structure and its dimensions is shown in Fig. 7.1a and an FBG sensor with a length of 10 mm embedded between two layers with orthogonal unidirectional layer direction is shown in Fig. 7.1b.

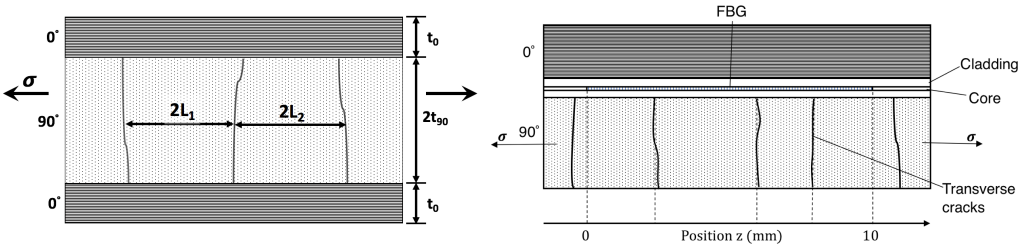

Figure 7.1: (a): A schematic of the cross section of the unidirectional composite structure affected by transverse cracks in its internal layers (b): The position of the FBG sensor between the layers of the composite structure.

7

Based on McCartney's theory, in the presence of transversal cracks in the middle layer of the composite, the stress field in the 0° layer along the length of the FBG can be calculated as [14]

$$\sigma^0_{zz} = \sigma \frac{E_0}{E^0_z}\Big(1 + \frac{t_{90}E_{90}}{t_0E_0}\frac{\cosh(\eta a z/l)}{cosh(\eta a)}\Big), \tag{7.6}$$

where σ is the axial stress applied to the composite structure, E_0 and E_{90} are the Young's moduli of the 0° (in the optical fibre direction) and the 90° plies respectively. The parameters t_0 and t_{90} are the thicknesses of the 0° and 90° plies, denoted in Fig. 7.1a, l is half the distance between the two consecutive cracks, and $a = \frac{l}{t_{90}}$ is the aspect ratio of the transverse cracking. The parameter η is the load transfer parameter given by

$$\eta^2 = 3(1 + \frac{1}{v})\frac{GE^0_z}{E_0E_{90}}, \tag{7.7}$$

in which $v = \frac{t_0}{t_{90}}$ is the ply thickness ratio, G is the shear parameter (refer to [14]), and E^0_z is the longitudinal Young's modulus of the undamaged laminate, given by

$$E^0_z = \frac{vE_0 + E_{90}}{1+v}.$$

The strain field along the z direction is then calculated as

$$s^0_{zz} = \frac{\sigma^0_{zz}}{E_0}.$$

In the above equations the effect of thermal expansion, which is the result of the difference between the manufacturing temperature and operating temperature, is neglected for two reasons. The first is that its effects are comparatively small on the strain distribution, and the second is that in the current application the variations of the strain field are of importance, and thermal expansion effects (and also the residual thermal stress from the curing process) only add an offset to the calculated strain field. It is noteworthy that McCartney's theory is derived with the assumption that the transversal cracks are equally spaced. In reality that is generally not the case, but the effect of this non-uniformity in the distribution of cracks on the strain distribution is negligible [5]. In this study, we will focus on transverse crack formation in two different types of composites, namely carbon fibre and glass fibre composites. In Section 7.5 we will discuss the layup and the materials in more detail. Nevertheless, it is important to emphasise that the shape of the strain peaks along the length of the sensor, their amplitude, and their width depends on the axial stress, the physical dimensions and the mechanical properties of the composite structure. Fig. 7.2 shows the axial strain distribution along the length of an FBG sensor that is embedded between the layers of a carbon fibre composite, with two transverse cracks along its length, calculated with McCartney's theory and using the properties given in Table 7.1 (table is presented in the next section).

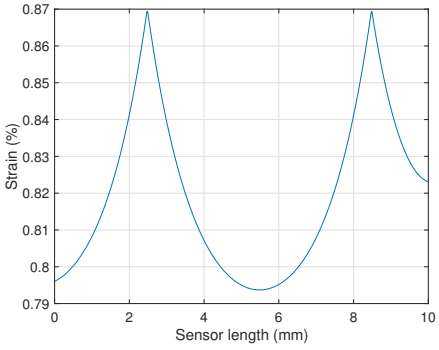

Figure 7.2: The strain distribution along the FBG length embedded between the layers of a carbon fibre composite structure, calculated using McCartney's theory at $\sigma = 550\,\text{MPa}$.

7.4. FBG Reflection Spectra Under Transverse Cracks

In Section 7.2 it was mentioned that when we have sharp strain changes along the length of the FBG sensor, the first terms in Eq. (7.2) are not negligible anymore. A particular example of such strain fields is when the sensor is in contact with transverse cracks in composite structures (similar to Fig. 7.2). Suppose there are N arbitrarily distributed cracks along the FBG length located at segments t_p, $p = 1, 2, ..., N$. In this case, the largest changes of the

strain field are expected at the boundaries of each segment t_p. Consequently, the largest values of the ζ_i parameters will be at the boundaries of segment t_p as well. Therefore, Eq. (7.2) can be rewritten as

$$R_c(\lambda) \approx \left| \sum_{i \in \mathscr{I}_c} \zeta_i e^{-j\left((M-2i)\alpha + \sum_{k\le i}\alpha_k - \sum_{k>i}\alpha_k\right)} + \sum_{i\in\mathscr{I}} \zeta_i e^{-j\left((M-2i)\alpha + \sum_{k\le i}\alpha_k - \sum_{k>i}\alpha_k\right)} + \xi_M e^{jM(\alpha-\tilde{\alpha})} - \xi_1 e^{-jM(\alpha-\tilde{\alpha})} \right|^2, \tag{7.8}$$

where $\mathscr{I} = \{t_1 - 1, t_1, t_2 - 1, t_2, ..., t_N - 1, t_N\}$, and $\mathscr{I}_c = \Omega \setminus \mathscr{I}$ is the complement of the set $\mathscr{I}$ in $\Omega = \{1, 2, ..., M\}$. Note that in the case of having both the magnitude and phase spectrum, one can take the Fourier transform of the side-lobes of the reflection spectrum where each of the non-negligible exponential terms in Eq. (7.8) will be translated into a unique peak in the Fourier domain. In that case, an exact localisation of the transverse cracks along the FBG length can be obtained. However, since practically the most convenient methods of FBG interrogation only have access to the magnitude of this spectrum, the focus will be on the amplitude of the reflection spectrum in this study.

In Eq. (7.8), the largest contribution of the ζ_i terms to the amplitude is due to the second summation (corresponding with $i = t_p - 1, t_p$). With that in mind, Eq. (7.8) can be approximated as

$$R_c(\lambda) \approx \sum_{i=1}^{M-1} |\zeta_i|^2 + \sum_{i,k\in\mathscr{I}}\sum \zeta_i \zeta_k^* e^{j\left((2i-2k)\alpha + \theta_k - \theta_i\right)} + \sum_{i\in\mathscr{I}} 2\mathrm{Re}[\zeta_i \zeta_M^*] \cos\left((2M-2i)\alpha + \theta_i - M\tilde{\alpha}\right) - \sum_{i\in\mathscr{I}} 2\mathrm{Re}[\zeta_i \zeta_1^*] \cos\left((2i)\alpha - \theta_i - M\tilde{\alpha}\right) + R_r + R_s, \tag{7.9}$$

where $\theta_i = \sum_{k\le i}\alpha_k - \sum_{k>i}\alpha_k$, R_s is the reflection spectrum for smooth strain fields given in Eq. (7.5), and R_r is the summation of the remaining terms with lower amplitudes than the ones mentioned in Eq. (7.9), which are the cross terms resulting from the first summation term in Eq. (7.8). As seen from Eq. (7.9), the formation of each transverse crack at location t along the length of the FBG model results in the emergence of new harmonics at the angular frequencies $\omega = 2M - 2t$ and $\omega = 2t$. Additionally, for every two cracks along the FBG length at locations i and k, there will be a non-negligible cross term with oscillation frequency of $\omega = 2(i - k)$. Furthermore, it can be seen from Eq. (7.9) that for each crack at segment t_p, each summation term consists of pairs of harmonics corresponding with $i = \{t_p - 1, t_p\}$ (associated with large strain changes before and after the crack). Consequently, the emerging harmonics due to these consecutive segments are only separated by a frequency distance of $\omega = 2$. Due to the decaying nature of the ζ_i terms in the α domain, the harmonics associated with each of these segment pairs overlap in the Fourier domain.

In order to analyse these new emerging harmonics, the Fourier transform of the side-lobes of the FBG reflection spectrum can be taken when the FBG sensor is in contact with transverse cracks. However, using a rectangular window will result in spectral leakage in the Fourier domain. In order to resolve this problem, and to also avoid the ambiguity of defining a proper range for the side-lobes, we propose replacing the rectangular window with a Hann window [15]. In this chapter, the lower bound of the window is chosen to be

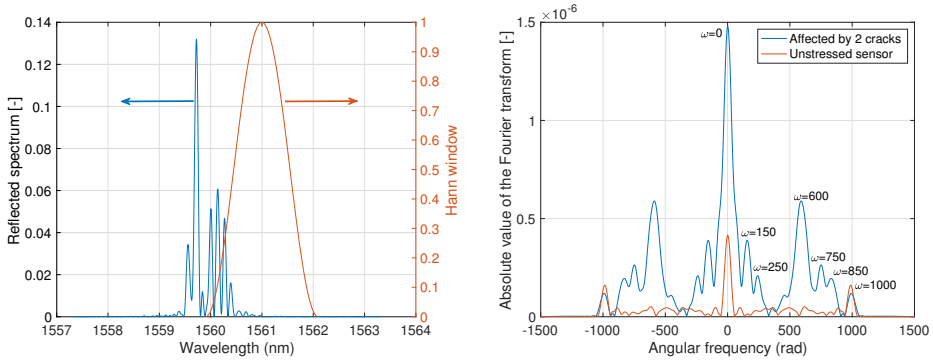

(a) (b)

Figure 7.3: (a): Reflection spectrum of a sensor near two cracks and the scaled Hann window. (b): Fourier transform of the windowed side-lobes for both stressed and unstressed sensors.

at the centre of mass of the reflection spectrum, given by

$$\lambda_{B_c} = \frac{\int_\lambda \lambda R(\lambda) \mathrm{d}\lambda}{\int_\lambda R(\lambda) \mathrm{d}\lambda}, \tag{7.10}$$

where λ is the wavelength region that covers the reflection spectrum. The upper bound of the window is case dependent and is set by the user. It should cover the wavelength region where the side-lobes' amplitudes are above the noise level. After applying this window (w), the Fourier transform of Eq. (7.9) will be calculated, resulting in

$$\mathscr{F}\{R_c\} \approx \mathscr{F}\{R_r w\} + \mathscr{F}\{R_s w\} + \sum_{i=1}^{M} \mathscr{F}\{|\zeta_i|^2 w\} \tag{7.11a}$$

$$+4 \sum_{i,k \in \mathscr{I}, i<k} \Psi_{i,k}(\omega \mp (2i-2k)) e^{\pm(\theta_k - \theta_i)} \tag{7.11b}$$

$$+4 \sum_{i \in \mathscr{I}} \Psi_{i,M}(\omega \mp (2M-2i)) e^{\pm(\theta_i - M\tilde{\alpha})} \tag{7.11c}$$

$$-4 \sum_{i \in \mathscr{I}} \Psi_{i,1}(\omega \mp 2i) e^{\pm(-\theta_i - M\tilde{\alpha})}, \tag{7.11d}$$

where $\Psi_{i,j}(\omega \mp (2i-2j)) = \mathscr{F}\{\mathrm{Re}[\zeta_i \zeta_j^*] w\} * \delta(\omega \mp (2i-2j))$, and $*$ denotes the convolution operator. Based on equations Eq. (7.11a) through Eq. (7.11d), a single peak in the strain distribution results in 4 new peaks in the Fourier domain in Eq. (7.11c) and Eq. (7.11d) (plus 6 other peaks that overlap with already existing harmonics), and two cross terms that emerge for each pair of peaks in the strain distribution in Eq. (7.11b). Out of these harmonics, the harmonics at $\omega = \{0, \pm 2M\}$ (included in the $\mathscr{F}\{R_s\}$ term) are always present and are independent of the strain field to which the sensor is subjected. Note that there are several other harmonics within the $\mathscr{F}\{R_r\}$ term in Eq. (7.11a) as well. However, since in the transverse crack scenario, the amplitude of all the ζ_i for $\forall\, i \neq \{t_p - 1, t_p\}$ terms are smaller

than ζ_{t_p-1} and ζ_{t_p}, the corresponding $\mathcal{F}\{\psi_i w\}$ terms will also have smaller amplitudes and will not form new peaks.

As mentioned before in this section, for N transverse cracks along the FBG length, there will be $2(\binom{N}{2}+2N)$ new harmonics in the Fourier domain with relatively large amplitudes. In the case that the number of transverse cracks along the FBG length increases, it is likely that due to the limited resolution, several of the new peaks in the Fourier domain appear to be overlapping. This makes the localisation of the cracks challenging for the cases where more than one or two cracks along the length of the sensor are formed, without any prior knowledge about the strain field. However, for early stages of crack formation (having one or two cracks along FBG length), this information can be used to precisely localise the cracks as well (except for a reflection line of symmetry ambiguity). Furthermore, by choosing FBG sensors with shorter lengths, the spatial resolution can be improved.

In order to visualise the analyses, the focus will be on transverse crack formation in two different types of composites, namely carbon fibre and glass fibre composites. The mechanical and physical properties of the materials that were used in this study are listed in Table 7.1.

Table 7.1: Mechanical properties of the composite structure (using the data in the datasheet of the Hexply 8552 and [16]). The FBG sensor is embedded in the 0° layer, in the proximity of the 90° layer and the cracks.

Material		Carbon fibre	Glass fibre
Elastic moduli (GPa)	E_0	148	36.5
	E_{90}	9.57	12.6
Shear modulus (GPa)	G_{xz}	5.6	3.9
Dimensions (mm)	t_0	0.732	0.34
	t_{90}	1.46	0.51
Axial stress (MPa)	σ	550	250

Consider the strain field given in Fig. 7.2 in a carbon fibre composite material, where the transverse cracks are located at $z = 2.5\,\text{mm}$ and at $z = 8.5\,\text{mm}$ from the start of a simulated FBG sensor with a total length of 10 mm and a nominal Bragg wavelength of 1550 nm. The calculated reflection spectrum in response to the FBG sensor being subjected to such a strain field is shown in Fig. 7.3. The FBG model was assumed to have $M = 500$ segments, therefore, the location of the crack will lie within the $t_1 = 125$'th and $t_2 = 425$'th segments. In all the computer simulations in this study, an additive zero mean Gaussian noise was considered on the ac amplitude of the refractive index of the core (SNR = 18dB), and also on the grating period of the FBG structure. This additive noise could lead to the emergence of new arbitrary peaks in the Fourier domain between $\omega = 0\,\text{rad}$ and $\omega = 1000\,\text{rad}$ angular frequencies, but for an unstressed sensor, they have much lower amplitudes than those resulting from transverse cracks. From equations Eq. (7.11b) through Eq. (7.11d) it is expected to see new peaks emerging at angular frequencies $\omega = \{0, \pm 150, \pm 250, \pm 600, \pm 750, \pm 850, \pm 1000\}\,\text{rad}$.

As seen from Fig. 7.3, new peaks have emerged in the Fourier transform of the sidelobes of the reflection spectra at the predetermined frequencies, which are more noticeable in the stressed sensor signal when compared with the healthy unstressed sensor signal (Fig. 7.3b).

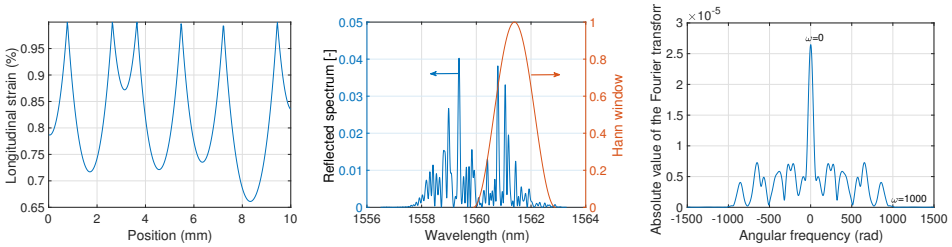

(a) (b) (c)

Figure 7.4: (a): Strain distribution along the length of the sensor when subjected to 6 transverse cracks, at σ = 250MPa (b): Reflection spectrum of a sensor near six cracks and the scaled Hann window. (b): Fourier transform of the windowed side-lobes of the reflection spectrum.

In a second computer simulation, a glass fibre composite material was considered, of which the physical properties are given in Table 7.1. In this example the composite structure was assumed to have 6 cracks along the length of the FBG sensor. The resulting reflection spectrum, and the Fourier transform of its side-lobes, are given in Fig. 7.4. Based on the discussions, for 6 transverse cracks, it is expected to have 54 new peaks in the Fourier domain. However, due to the overlap of several of these peaks, there are only 14 peaks visible in the figure, which mostly correspond with cross terms that are defined in Eq. (7.11b) (due to their relatively higher amplitudes).

7.5. EXPERIMENTAL RESULTS AND DISCUSSION

In this section, our hypotheses will be validated using experimental measurements. For this purpose, embedded FBG sensors were used within the layers of two different types of unidirectional (UD) composites. In the first example, AS4-UD carbon/Hexply 8552 prepreg sheets from Hexcel corporation were used, with the layup of $[0_4, 90_{16}, 0_4]$, and an FBG sensor with a length of $L = 10\,\text{mm}$ embedded between the 4th and 5th layer of the composite (at the interface of the 0° and 90° layers). The precise position of the FBG sensor was determined by using the methods presented in Chapters 5 and 6.

The curing process specified in the datasheet of the material was followed. The FBG sensor was a DTG type sensor from the company FBGS, with a nominal Bragg wavelength of $\lambda_n = 1570\,\text{nm}$. The DTG sensors had an Ormocer coating, which according to the producing company, allows a 1:1 strain transfer to the sensor. The mechanical and physical properties of the material are given in Table 7.1. After the production, the specimens were cut into coupons of 2.5 by 15 centimetres, with the FBG at the centre of the coupon. The specimens were then subjected to a quasi-static test using a 100 kN MTS machine, where the tensile stress was increased from $\sigma = 50\,\text{MPa}$ to $\sigma = 400\,\text{MPa}$ in steps of $\Delta\sigma = 10\,\text{MPa}$.

The FBG reflection spectra were recorded using a PXIe-4844 FBG interrogator from National Instruments, which has a dynamic range of 40 dB and a wavelength resolution of 4 pm. Also, in order to localise the cracks, a camera was placed facing the side of the specimens (therefore directly viewing the crack formation in the 90° layers of the composite, as seen in Fig. 7.5a). As expected from our model and the literature, before the formation of the cracks the FBG reflection spectrum held its general shape without much difference

during the tensile test. It is noteworthy that since the curing of the carbon fibre panel was performed in an autoclave with pressures as high as 8 bar, there was already a residual transverse load on the FBG sensor. Therefore, even a sensor in an unloaded coupon was already affected by birefringence effects and had a widened reflection spectrum (widened by more than 2 times), and hence the asymmetrical shape of the sensor at the start of the experiment. Right after the formation of the first crack, the reflected spectrum changed shape and new harmonics were created.

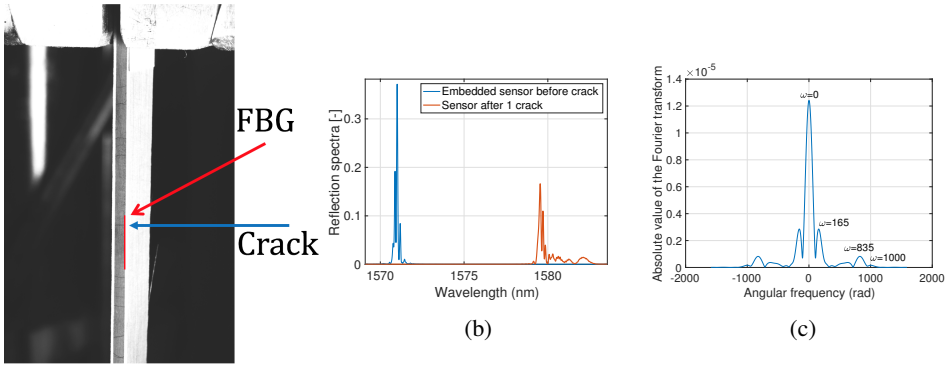

Figure 7.5: (a): Carbon fibre specimen under a quasi-static tensile test, (b): Reflection spectra of the FBG before any cracks (blue) and after the formation of a crack (red), and (c): Fourier transform of the windowed side-lobes of the reflection spectrum.

7

Fig. 7.5 shows the specimen under tensile testing, the FBG reflection spectrum before and after crack formation, and the emerged new harmonics in the Fourier transform of the side-lobes of the reflection spectrum. As seen from this figure, at this particular time during the test (at $\sigma = 330\,\text{MPa}$), one single crack was formed at location $z = 1.65\,\text{mm}$ from the start of the sensor, which results in the emergence of two additional peaks at $\omega = \{165, 835\}$ rad in the Fourier domain. The resulting new harmonics due to this crack are shown in Fig. 7.5c, and it can be seen that they are located at the expected locations with respect to the location of the crack.

In the second experiment, UD glass fibre materials from Saertex GmbH were used, with a density of $228\,\text{g/m}^2$, a layup of $[0_2, 90_6, 0_2]$ and an overall thickness of 1.65 mm. The FBG sensors were embedded between the 2nd and the 3rd layers of the composite (again at the interface of the 0° and 90° layers). For this material, the fusion method was used to produce the composites, from Epikote 04908 resin and curing agent from Hexion Ltd. The material was initially cured at room temperature for 24 hours, and then for 6 hours in the oven at $80°C$ and at a pressure of 1000 mbar. After the curing process, the specimens were cut into 3 by 25 centimetre coupons, with the FBG sensor at the centre of the coupon. For this example we also used a camera to record the crack formation, but since glass is translucent, the camera was facing the surface of the material, and the formation of the cracks in the internal layers of the composite were seen from the surface. The GFRP specimens were

subjected to a similar test as the CFRP specimens, but starting at $\sigma = 10\,\text{MPa}$ to $\sigma = 150\,\text{MPa}$ in steps of $\Delta\sigma = 5\,\text{MPa}$, as the GFRP specimens were less stiff than the CFRP specimens used in this study.

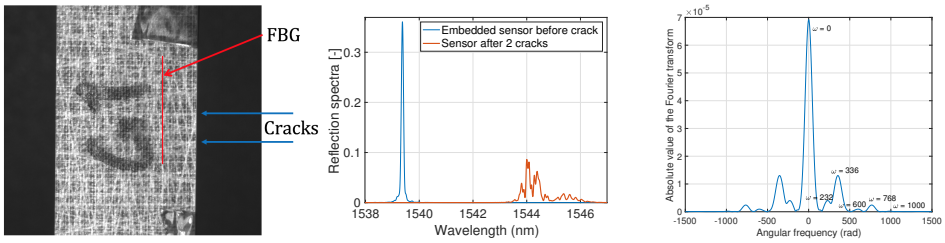

(a) (b) (c)

Figure 7.6: (a): Glass fibre specimen under a quasi-static tensile test, (b): Reflection spectra of the FBG before any cracks (blue) and after the formation of two cracks (red), and (c): Fourier transform of the windowed side-lobes of the reflection spectrum.

Fig. 7.6 shows the specimen under tensile test at $\sigma = 50\,\text{MPa}$, where two transverse cracks have already formed at locations $z = 6\,\text{mm}$ and $z = 7.68\,\text{mm}$ from the start of the sensor. The localisation of the cracks from the recorded images was performed by visually comparing consecutive images at different force loads. The FBG reflection spectra before and after crack formation, and the emerged new harmonics in the Fourier transform of the side-lobes of the reflection spectrum are also shown in this figure. Also note that since the sensor did not undergo high transverse pressures during its production, the FBG reflection spectrum looks more pristine and is less affected by birefringence effects. Given the locations $z = 6$ mm and $z = 7.68$ mm, we expect the emergence of additional peaks at $\omega = \{600, 768, 400, 232, 336\}$rad in the Fourier domain, which correspond well with the resulting peaks from the experiment. Note that in both experiments, since the number of cracks were limited to just 1 or 2, the cracks could also be localised. But having more than 2 cracks and having no access to the phase of the reflection spectrum will make their localisation much more difficult.

As it is evident from these experiments, our model could perfectly explain the emergence of the new peaks in the Fourier transform of the side-lobes of the reflection spectrum, and the peaky nature of the strain field due to the transverse cracks has a clear effect on these new harmonics. It can be also seen that birefringence effects and other noise sources did not affect the results. Note that the sensors used in these experiments were partially apodized, and hence, the lower amplitude of the $\omega = 1000$ peaks compared with the simulated examples.

As a last example, we tried to create a widened FBG reflection spectrum under a smooth non-uniform strain field, without having any cracks along the FBG length. A three point bending test (loading pin on the sensor location) was applied on one of the glass fibre specimens with an embedded FBG. Due to the non-uniformity of this strain field, the resulting reflection spectrum (shown in Fig. 7.7) became wider (the FWHM of an unstressed sensor was 84 pm, and it was widened by three times under the test), however, as seen from Fig. 7.7b, no meaningful new harmonics have been added to the Fourier transform of the

side-lobes of the reflection spectrum.

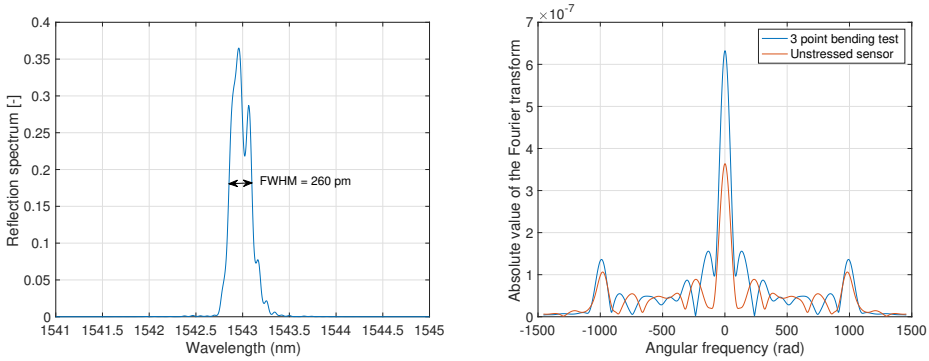

(a) (b)

Figure 7.7: (a): Reflection spectrum of an FBG under a three point bending test, (b): Fourier transform of the windowed side-lobes of the reflection spectra from the stressed and unstressed sensor.

In summary, it was argued that if there is a sudden change of strain distribution along the FBG length, it will have a direct effect on the reflection spectrum side-lobes. In this chapter, this phenomenon was analysed in the formation of transverse cracks in uni-directional composite materials, but it can be extended to any other structure or material as well, including metals or concrete. The conditions that need to be met in order to perceive this effect are firstly, a direct contact of the sensor with the sharply varying strain field, and secondly, a high enough strain peak amplitude. The latter condition depends on the type of sensor in use, and also, the host material under investigation. For instance, in the glass fibre composite specimens with the given dimensions used in this study, and using DTG type sensors, computer simulations suggest that a strain peak of around 400 $\mu\epsilon$ will result in distinguishable new harmonics in the Fourier transform of the FBG reflection spectrum side-lobes, whereas for the carbon fibre specimens, this value was around 300 $\mu\epsilon$, which is due to the stiffer nature of the carbon fibre samples. With that in mind, it should be noted that in the laboratory experiments, the first cracks were forming under strain peak values of more than 1000 $\mu\epsilon$, which is already far more than the theoretical sensitivity threshold of the FBG sensors.

7.6. CONCLUSIONS

In this chapter a clear relationship between the transverse cracks along the length of FBG sensors, and the emergence of new harmonics in the Fourier transform of the side-lobes of the FBG reflection spectra was demonstrated. It was argued that the mere widening of the FBG reflection spectra is not a reliable measure for detection of cracks, as it might also occur in response to other types of non-uniform strain fields, and we suggested to focus on the information in the side-lobes of the reflection spectra as a more reliable indication of cracks along the sensor length. Our model was validated with both computer simulations and experimental measurements, and the results were in good agreement with our model. Future works in this subject could include analysis of the crack formation in different layup

configurations of composite materials, and their effects on the FBG reflection spectra. Also, extending the current model to the other types of damages in composite structures could also be beneficial to the community.

REFERENCES

[1] Y.-J. Rao, "Recent progress in applications of in-fibre Bragg grating sensors," *Optics and Lasers in Engineering*, vol. 31, no. 4, pp. 297–324, 1999.

[2] D. Kinet, P. Mégret, K. W. Goossen, L. Qiu, D. Heider, and C. Caucheteur, "Fiber Bragg grating sensors toward structural health monitoring in composite materials: Challenges and solutions," *Sensors*, vol. 14, no. 4, pp. 7394–7419, 2014.

[3] S.-i. Takeda, Y. Aoki, and Y. Nagao, "Damage monitoring of CFRP stiffened panels under compressive load using FBG sensors," *Composite Structures*, vol. 94, no. 3, pp. 813–819, 2012.

[4] N. Takeda, Y. Okabe, and T. Mizutani, "Damage detection in composites using optical fibre sensors," *Proceedings of the Institution of Mechanical Engineers, Part G: Journal of Aerospace Engineering*, vol. 221, no. 4, pp. 497–508, 2007.

[5] Y. Okabe, T. Mizutani, S. Yashiro, and N. Takeda, "Detection of microscopic damages in composite laminates," *Composites Science and Technology*, vol. 62, no. 7, pp. 951–958, 2002.

[6] A. D. Kersey, M. A. Davis, H. J. Patrick, M. LeBlanc, K. Koo, C. Askins, M. Putnam, and E. J. Friebele, "Fiber grating sensors," *Journal of Lightwave Technology*, vol. 15, no. 8, pp. 1442–1463, 1997.

[7] T. Erdogan, "Fiber grating spectra," *Journal of Lightwave Technology*, vol. 15, no. 8, pp. 1277–1294, 1997.

[8] Y. Okabe, R. Tsuji, and N. Takeda, "Application of chirped fiber Bragg grating sensors for identification of crack locations in composites," *Composites Part A: Applied Science and Manufacturing*, vol. 35, no. 1, pp. 59–65, 2004.

[9] T. Okabe and S. Yashiro, "Damage detection in holed composite laminates using an embedded FBG sensor," *Composites Part A: Applied Science and Manufacturing*, vol. 43, no. 3, pp. 388–397, 2012.

[10] A. R. Chambers, M. C. Mowlem, and L. Dokos, "Evaluating impact damage in CFRP using fibre optic sensors," *Composites Science and Technology*, vol. 67, no. 6, pp. 1235–1242, 2007.

[11] Y. Okabe, S. Yashiro, T. Kosaka, and N. Takeda, "Detection of transverse cracks in CFRP composites using embedded fiber Bragg grating sensors," *Smart Materials and Structures*, vol. 9, no. 6, p. 832, 2000.

[12] A. Rajabzadeh, R. Heusdens, R. C. Hendriks, and R. M. Groves, "Calculation of the mean strain of smooth non-uniform strain fields using conventional FBG sensors," *Journal of Lightwave Technology*, vol. 36, no. 17, pp. 3716–3725, 2018.

[13] L. McCartney, "Theory of stress transfer in a 0-90-0 cross-ply laminate containing a parallel array of transverse cracks," *Journal of the Mechanics and Physics of Solids*, vol. 40, no. 1, pp. 27–68, 1992.

[14] J.-M. Berthelot, "Transverse cracking and delamination in cross-ply glass-fiber and carbon-fiber reinforced plastic laminates: static and fatigue loading," *Applied Mechanics Reviews*, vol. 56, no. 1, pp. 111–147, 2003.

[15] A. V. Oppenheim, *Discrete-time signal processing*. Pearson Education India, 1999.

[16] T. M. Hermann, J. E. Locke, and K. K. Wetzel, "Fabrication, testing, and analysis of anisotropic carbon/glass hybrid composites volume 1: Technical report," tech. rep., Citeseer, 2006.

8

Accurate Delamination Tip Monitoring of Laminated Composites in Mode-I Fatigue Tests Using FBG Sensors

She had never imagined that curiosity was one of the many masks of love.

Gabriel Garcia Marquez, Love in the Time of Cholera

One of the most common and crucial types of damages in composite structures is the delamination of composite laminates. Therefore, there has been a lot of research on the behaviour of delaminated composite materials under fatigue and tensile tests, where uncertainty in determining the crack tip position can adversely affect the accuracy of the experimental results. Due to the formation of the delaminated areas in the internal layers of composites, localising the delamination tip and determining its growth rate with the state-of-the-art structural health monitoring methods can be time consuming, and/or provide a limited spatial resolution. Moreover, the commonly used delamination growth monitoring method based on camera images of the sides of the composite specimens does not account for the non-uniform delamination tip growth across the delamination plane, and only provides information about the (visible) outer edge of the delamination plane. Further, using camera

*This chapter is submitted to the Journal of Experimental Mechanics as "Accurate Delamination Tip Monitoring of Laminated Composites in Mode-I Fatigue Tests Using FBG Sensors", by A. Rajabzadeh, R. C. Hendriks, R. Heusdens, and R. M. Groves, 2020

images for delamination tip monitoring limits the designed setup of the fatigue test, as the delamination tip must always face the camera. In this chapter, we will present a novel approach using fibre Bragg grating sensors, for accurate, distributed and dynamic localisation of the delamination tip in composite materials with sub-millimetre accuracy.

8.1. INTRODUCTION

Laminated composites are used extensively in recent aerospace applications. Their versatility and flexible design, have enabled researchers and engineers to tailor the physical and mechanical properties of the overall composite product based on their needs [1]. However, despite their high strength and stiffness, laminated composite structures are susceptible to fatigue and impact damages, and the progression of the damage under different loads hugely depends on the layup, fibre orientation, and the composition of the laminated composite structure. For these reasons, there is a lot of demand for reliable and accurate structural health monitoring techniques for behavioural analysis of laminated composite materials when affected by such defects [1]. Among the different damage types in laminated composites, delamination of the layers is among the most prevalent ones [2]. However, due to the complicated mechanical response of these materials under different layups, and the non-uniform strain fields from delamination cracks, a reliable and high-speed experimental analysis of the progression of such damages has remained a challenge.

Currently, methods such as ultrasonic scanning [3, 4], Terahertz sensing [5], acoustic emission [6], thermography [7], and shearography [8], are among the most commonly used tools to gather information about the damage state in composites, and in particular, on the detection of delamination. However, these methods can be time consuming, rely heavily on the expertise of the operator, limit the type of reinforcement fibres used for the composite, or have a poor spatial resolution. There have also been alternative studies in which fibre optic sensors or fibre Bragg grating sensors were used for delamination size and growth direction monitoring. In [9] it was shown that there is a relationship between the delamination length and the changes measured in the spectrum of chirped Bragg gratings. In [10], FBG sensors were used to monitor the low velocity impact induced delamination in composites. A similar comparison was made between the bandwidth and the intensity level of FBG reflection spectra, and the delamination length in woven composites in [11]. In [12], Farmand et al. used an integrated multiplexed system of short FBG sensors (each with a length of 1 mm and 3 mm spacing between each two consecutive sensors) to monitor the progression of the delamination crack quasi-distributedly. However, in studies of this kind, the spatial resolution is usually poor, and an accurate determination of the crack tip is not offered. Along the same lines, in [13] Sorensen et al. proposed a method using long FBG sensors (in the range of 22 to 35 mm long sensors) and optical low coherence reflectometry (OLCR) to calculate the complex FBG reflection spectrum, and then iteratively reconstruct the strain distribution along the FBG length under delamination defects, using which, the crack tip was calculated. Using the same OLCR interrogation approach, Sans et al. also presented a method for identification of the crack tip in mixed-mode delamination defects [14]. Although the accuracy and the spatial resolution of these approaches are high, they are time-consuming (both the interrogation and the data processing), and multiplexing several sensors and interrogating multiple delamination paths is cumbersome and requires several parallel interrogation systems.

Another approach that is often taken in monitoring the delamination tip growth, is to use camera images from the side of the composite specimen [13, 15, 16]. This method provides useful information about the current state of the delamination tip in real time, and with high accuracy, however, it only monitors the delamination tip from the side of the specimen. As shown in [17] and also later in this chapter, the delamination growth plane in composites can be non-uniform across the specimen. Therefore, camera images overlook the non-uniform damage growth across the delamination plane. Furthermore, using camera images for delamination monitoring limits the test setup, as the delamination tip must always face the camera.

In this chapter, we propose a novel approach, in which we use commercial uniform fibre Bragg grating (FBG) sensors to accurately, reliably, and dynamically monitor the delamination plane growth in composite materials in mode-I fatigue and tensile tests. Based on finite element modelling and previous studies [9, 14], we make in this study the underlying assumption that there is a sudden strain change at the delamination tip in composites. Based Chapters 3 and 7, we know that a sudden strain change along the FBG length translates into an addition of a new harmonic frequency in the FBG reflection spectrum. We will show that the peak frequency of this newly added harmonic, linearly depends on the location of the delamination tip along the FBG sensor. Monitoring the frequency of he newly added harmonic, we can accurately determine the delamination tip location in the internal layers of the composite material. Furthermore, due to the small diameter of FBG sensors, multiple optical fibres can be embedded between the composite layers parallel to each other, without severely altering the structural integrity of the composite [18], to provide us with a semi-distributed delamination tip monitoring across the entire delamination plane. We will validate the claims made in this chapter with computer simulations and experimental measurements.

8.2. DELAMINATION TIP MONITORING METHOD

In progressive delamination type damages that occur in the embedded FBG area, such as those found in mode-I fatigue and tensile tests, the delamination propagation is mostly confined within the delamination plane. Specifically, in mode-I delamination tests, the delamination tip along the FBG length will start at one end of the sensor, and progresses through its whole length. In this case, using the closed-form representation of the FBG reflection spectrum (embedded along the delamination plane), we will obtain

$$R(\alpha) \approx \sum_{i=1}^{M-1} |\zeta_i|^2 + 2\,\mathrm{Re}[\zeta_t \zeta_M^*] \cos\left((2M-2t)\alpha + \theta_t - M\bar{\alpha}\right) \\ -2\,\mathrm{Re}[\zeta_t \zeta_1^*] \cos\left(2t\alpha - \theta_i - M\bar{\alpha}\right) + R_r + R_s. \tag{8.1}$$

Eq. (8.1) shares the same set of parameters as Eq.(7.9) in the previous chapter. From Eq. (8.1) it can be seen that at the start of the delamination, i.e., for $t = 1$, the additional harmonic (due to the delamination) will overlap with the harmonic already present in the term R_s (which is present already under uniform stress) having the maximum frequency of $\omega = 2M$. As the delamination progresses, the frequency of the additional harmonic will monotonically decrease towards lower frequencies. As discussed in the previous section,

Algorithm 3 Delamination tip monitoring algorithm

1: Determine the side-lobes of the FBG reflection spectrum by setting a threshold on the amplitude.

2: Apply a Hann window [19] on the reflection spectrum side-lobes, and take the Fourier transform of the windowed signal.

3: Determine the angular frequency of the highest frequency component in the Fourier transform signal.

4: Track the angular frequency of this high frequency component as the delamination tip progresses.

assuming that the delamination tip has reached the t'th segment of the FBG, the associated high amplitude harmonic frequency will be at $\omega = 2M - 2t$. From this frequency, the location of the delamination tip can be continuously monitored. In summary, the delamination tip monitoring algorithm can be expressed as Algorithm 3. In step 1 of this algorithm, the window function boundaries were chosen based on the noise floor of the interrogator system with the FBG sensor was connected to it. The upper bound of the window was set at a wavelength at which the amplitude of the reflection spectrum passed a threshold of two times the maximum amplitude of the noise floor. The lower bound of the window was chosen with a fixed distance from the upper bound, as long as it does not cover the main lobe of the reflection spectrum. In the experiments of this chapter, the window length was assumed to be 2 nm. The experiments of this chapter showed that as long as the main lobe of the spectrum is not included in the window, the choice of the window boundaries has little effect on the accuracy of the delamination monitoring algorithm, but it can alter its precision up to a few tens of micrometers. As an example, Fig. 8.3 shows the relationship between the angular frequency of the new harmonics, and the position of the delamination tip along the FBG length. The choice of the window function (changing the upper bound threshold and a fixed 2 nm window length) in this example could change the offset of the linear regression in Fig. 8.3d by as much as 0.12 mm, but did not have a noticeable effect on its slope.

In the following sections we will also investigate the effect on the performance of our delamination tip monitoring algorithm of embedding the sensor in other layers of the composite that are not in the delamination plane. This effect will be first discussed in the next section, with finite element analysis of the composite specimens under mode-I tensile tests.

8.3. FINITE ELEMENT ANALYSIS

In this section, we will use finite element analysis (FEA) to model the behaviour of a unidirectional glass fibre composite material under mode-I delamination. The mechanical characteristics of the glass fibres used in the FEA are the same as the materials used in the experimental measurements, with longitudinal and transverse moduli of E_0 = 36.5 GPa, E_{90} = 12.6 GPa, respectively, and an in-plane shear modulus of G = 3.9 GPa [20]. These properties belong to glass fibres from Saertex GmbH, with a density of 228 g/m^2, a layup

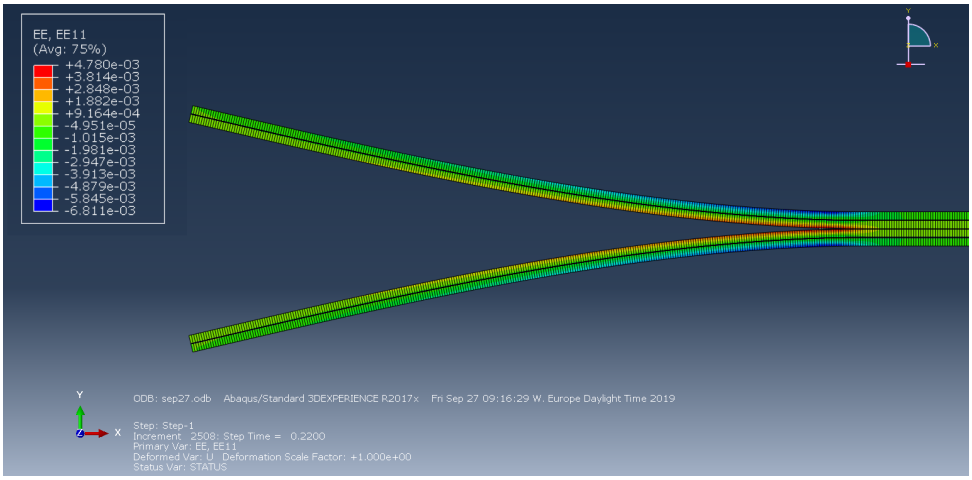

Figure 8.1: 2D finite element model of a mode-I delamination test in a glass fibre composite material. The colour bar shows the longitudinal strain values.

of $[90_4, 0_8, 90_4]$, and an overall thickness of 2.7 mm. The dimensions of the specimens are 20×5 cm, and the delamination is assumed to start from the side of the specimen between the 8th and the 9th layer. The initial opening had a length of 2 cm, and a cohesive model was assumed between each pair of two laminates with different fibre orientations. The simulations were performed in ABAQUS software, with a mesh size of 0.1 mm and a presumed 2D model. With that, we applied a symmetrical displacement of 5 mm on the specimen (see Fig. 8.1).

The axial strain was calculated along three different paths along different layers of the composite, along the x direction, which is parallel to the 0 degree laminates and the embedded optical fibre. The first path was in the delamination plane (called the delamination path throughout this chapter), the second path was at the interface of the 0 degree and the 90 degree layers (at a distance of around 0.7 mm from the delamination plane and called middle path in this chapter), and the final path was on the surface of the specimen (called top path throughout the chapter). The resulting axial strain distributions at a certain time and along all three paths are plotted in Fig. 8.2a, and their corresponding derivatives are plotted in Fig. 8.2b. In these figures, the location of the delamination tip is at a position where the derivative of the strain field along the delamination path reaches its peak, which is at a distance of 4.1 mm along the FBG length.

As is evident from these figures, the distances at which the derivative of the strain field is at its peak have small differences from each other along different paths. In the middle path, this peak is located at a distance of 0.3 mm from the delamination path, and in the top path, it is located at a distance of 0.6 mm from the delamination path. However, these simulations suggest that an FBG sensor along each of these paths would experience a large enough strain difference along its length to be used as a delamination monitoring sensor. This is obviously regardless of the fact the sensor is under tension (in the delamination plane) or under compression (in the middle or top planes).

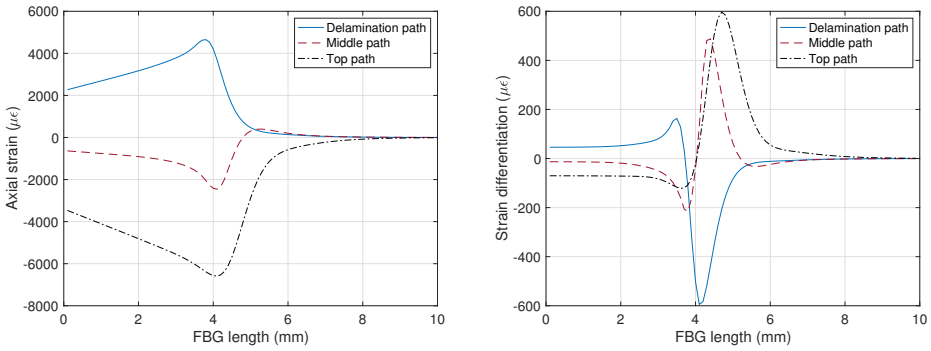

(a) (b)

Figure 8.2: (a): The strain distribution along the FBG sensor embedded or surface mounted on a composite affected by delamination. (b): The derivative of the strain field along the FBG length at different distances from the delamination plane.

It is noteworthy that in the results of this section, only the trend of the strain field at the delamination area is of interest. There are several factors that contribute to the amplitude of the strain distribution and the delamination growth rate (such as the elastic moduli and the thickness of the adhesive layer between the laminates), and a precise comparison between the finite element model results, and those from the laboratory experiments are beyond the scope of this chapter. However, the sharp strain shift at the delamination tip is a mutual trait in all such results, even within an order of magnitude of variation for the adhesive layer dependent parameters.

The hypotheses of this section will be tested in the experimental results section. In the next section, these strain fields will be used as input to the forward transfer matrix model, in order to test the performance of the delamination tip monitoring algorithm in computer simulations.

8.4. Experiments and Results

In this section, we will first use computer simulations to visualise the performance of our delamination tip monitoring algorithm. Afterwards the algorithm will be validated with laboratory experiments and FBG recordings under mode-I tensile tests.

8.4.1. Computer simulations

In this subsection, we use the axial strain fields that were generated from the finite element analysis in the previous section and input them to the transfer matrix model to generate the corresponding FBG reflection spectra. In the experiments of this section, we consider a uniform FBG sensor of length 10 mm, with a Bragg wavelength of 1550 nm, and the FBG model was assumed to consist of $M = 500$ piece-wise uniform segments. As the delamination damage progresses along the FBG sensor, the strain fields were calculated at different time instances using the finite element model. Fig. 8.3a shows a number of these strain fields that were calculated along the delamination plane and at different time

instances. It can be seen from this figure that as the delamination is progressing along the FBG length, the peak of the strain field is shifted along the FBG length.

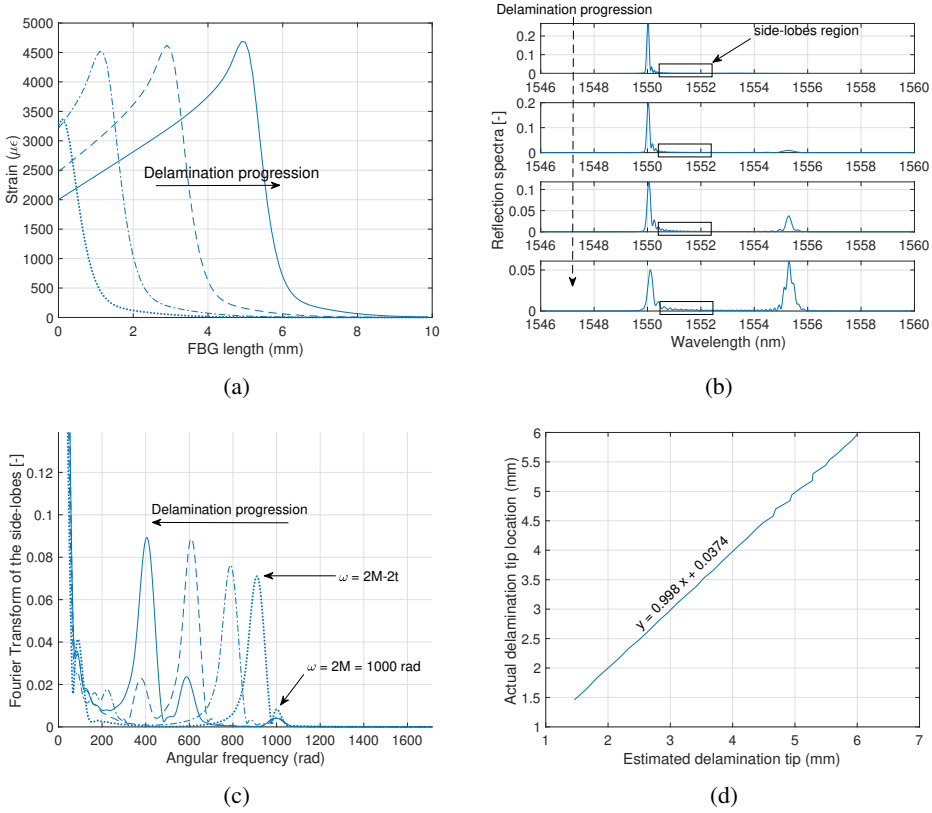

Figure 8.3: (a): The strain distribution along the FBG length (from the FEM), resulted from the progression of the delamination defect in the delamination plane. (b): FBG reflection spectra at different delamination stages along the sensor length. The window length for the side-lobes selection was assumed to be 2 nm. (c): The amplitude of the Fourier transform of the side-lobes. The progression of the delamination defect is linearly translated into the shift of the $\omega = 2M-2t$ frequency component to lower frequencies. (d): The linear dependence of the delamination tip position and the estimated delamination tip location retrieved from the FBG sensor.

Using the axial strain fields of Fig. 8.3a and the transfer matrix model [21], the corresponding FBG reflection spectra were calculated (Fig. 8.3b). Then, the Fourier transform of the side-lobes (shown in Fig. 8.3b) were calculated and depicted in Fig. 8.3c. Finally, the linear dependence of the maximum harmonic frequency ($\omega = 2M - 2t$) and the delamination tip location along the FBG length, was plotted and is shown in Fig. 8.3d. It can be seen from Fig. 8.3d that the linear regression line has a small offset of 0.0374 mm. This small offset, is due to the uncertainty in the choice of the side-lobes region and its length. However, once these values are set, the estimator can be calibrated with another reference method to remove this bias.

The algorithm was also run on virtual FBG reflection spectra that were embedded in the

middle layer (in the intersection of the 0 degree and 90 degree layers of the composite), and surface mounted on the top of the specimen. As expected from Fig. 8.2b and depicted in Fig. 8.4a, the estimated delamination tip location from the virtual FBG sensor in the middle path and in the top path of the composite have a small offset compared to the retrieved tip from the delamination plane. Hence, the offset values get larger the further the sensor is from the delamination plane. Also, note that since in the middle layer and on the top layer, the strain field is compressive, the window function was applied on the flip side of the reflection spectra (at lower wavelengths). The compression or tension effect on the sensor in these delamination defect setups can be determined by looking at the position of the main lobe of the spectrum. If the side-lobes progress towards lower wavelengths, it can be concluded that the load is compressive, and vice-versa for the tensive loads. A sample reflection spectrum of a virtual FBG sensor on the top layer is shown in Fig. 8.4b. As shown in Fig. 8.4a, the offset values associated with the linear regressions of the FBG outputs at the middle path and top path correspond well with the location of the derivative peaks of their associated strain fields (see Fig. 8.2b). For example, the offset value of the regression line from the FBG output at the top layer is 0.5878, which represents the relative derivative peak shift of the strain field at the top layer with respect to the delamination plane, which was around 0.6 mm (see Fig. 8.2b).

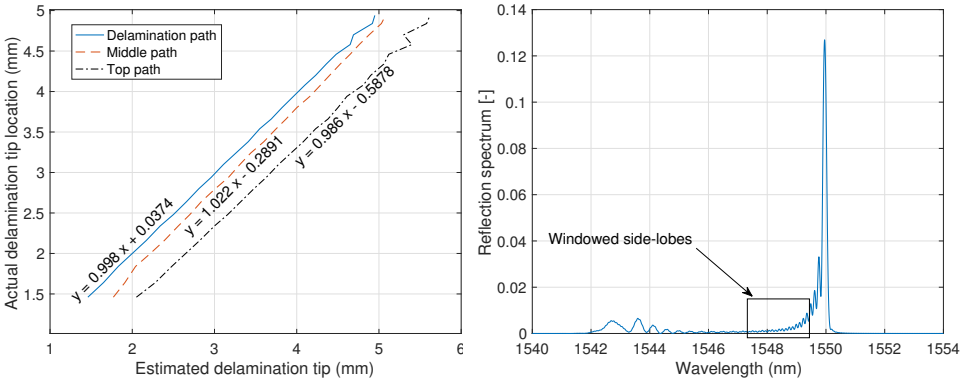

(a) (b)

Figure 8.4: (a): Different offset values for the linear regression along different composite planes. (b): The effect of the compressive strain field of the delamination defect on the FBG reflection spectrum on the top layer of the composite.

8.4.2. LABORATORY EXPERIMENTS

EXPERIMENT SETUP

In this part, we will analyse the FBG reflection spectra from laboratory experiments. The FBG sensors were from the company FBGS, with Bragg wavelengths at 1530, 1550 and 1570 nm. The fibres had an Ormocer coating, that according to the producing company allows a 1:1 strain transfer to the sensor. In particular, based on the finite element modelling results presented in [22], for the cases where the difference between the Young's modulus

of the host material and the optical fibre is not significant, and also the cases where the thickness of the laminates are thick in comparison with the optical fibres, the strain transfer increases and becomes more stable. This is also the case with the experiments of this study.

The length of the sensors is 10 mm, with reflectivity levels of around 40 percent. The FBG sensors were interrogated using a PXIe-4844 tunable laser Fabry-Perot based interrogator from National Instruments, with a wavelength resolution of 4 pm, and a dynamic range of 40 dB. The outputs were recorded using LabVIEW software from National Instruments, and the recorded signals were then processed in MATLAB R2019a.

For the composite materials, we chose uni-directional glass fibres, with a configuration and mechanical properties similar to that of section 8.3. The optical fibres, containing the FBG sensors were embedded between the composite layers, one in the delamination plane and one in the middle plane (between the 0 degree and the 90 degree layers). The initial delamination was induced at the side of the composite panel, between the 8th and the 9th layer, by putting a 5 cm wide sheet of Kapton tape between them. The layup was then cured at room temperature in a vacuum bag for 24 hours. The composite panel was then cut into specimens of size 20×5 cm.

After adhering handles on the specimens, they were subjected to a mode-I quasi-static tensile test with a 10 kN material tensile test machine from Zwick. A side-view of the specimen halfway through the test is shown in Fig. 8.5a, and a top view of the specimen is shown in Fig. 8.5b. A microscopic image of the delaminated area, and its non-uniform propagation across the width of the specimen is shown in Fig. 8.6.

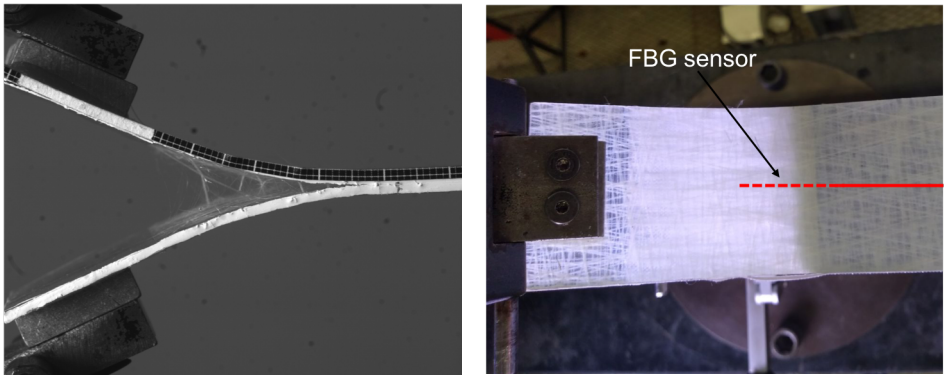

(a) (b)

Figure 8.5: (a): The side-view of the specimen at a time instance during the mode-I tensile test. (b): The top view of the same specimen at the same time instance, and the position of the FBG sensor between the laminates.

In the introduction section, we argued that the delamination front progressing through the delamination plane was expected to be non-uniform across the width of the specimen. This means that for the FBG sensor that is embedded at the centre of the specimen (see Fig. 8.6), the retrieved tip of the delamination will be different than what can be seen from the side-view. This non-uniformity is also evident in Fig. 8.6, where the delamination defect has progressed more in the sides than the central parts. In the next subsection, it will be seen that this non-uniformity will result in a discrepancy between the delamination tip location

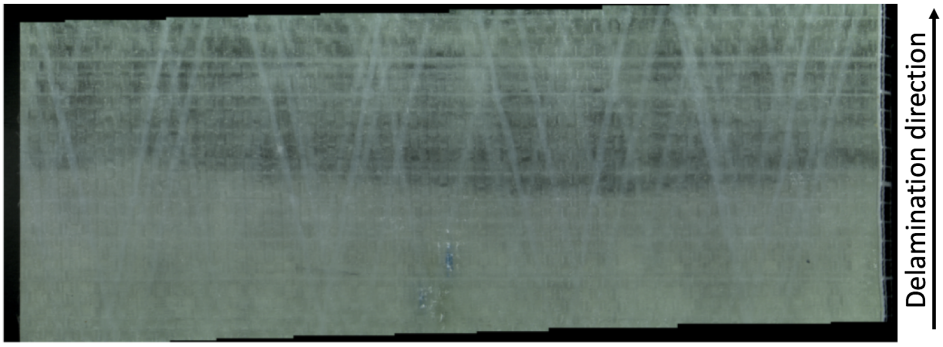

Figure 8.6: Microscopic image of the delamination area across the specimen width. The opaque area has already delaminated, and the translucent part is still bonded.

retrieved from the FBG sensor, and that of the camera images from the side of the specimen.

EXPERIMENTAL RESULTS

Similar to the computer simulation experiments, we will monitor the delamination of the composite structure with FBG sensors along three different layers. The first sensor was embedded during the production of the composite in the delamination plane, the second sensor was embedded at the intersection of the 0 degree layers and the 90 degree layers of the composite (called the middle layer), and the third sensor was surface mounted on top of the specimens before the tests (called the top layer). Fig. 8.7a shows the reflection spectra of an FBG sensor in the delamination plane, as the delamination defect is progressing along its length. Fig. 8.7b depicts the amplitude of the Fourier transform of the side-lobes of the reflection spectra shown in Fig. 8.7a.

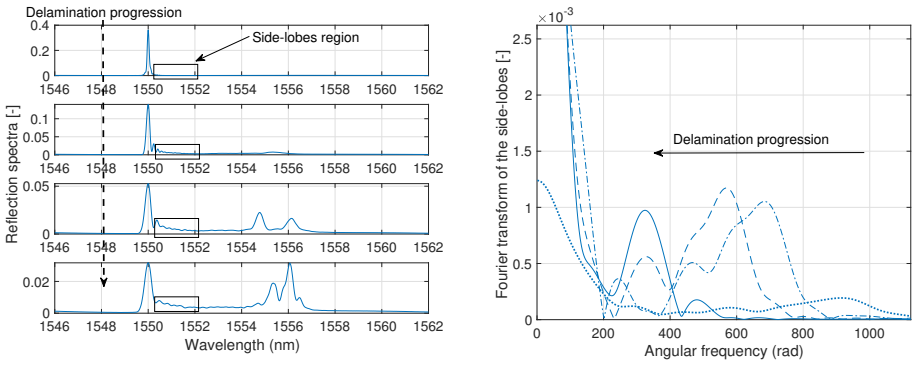

(a) (b)

Figure 8.7: (a): The reflection spectra for a real FBG sensor at different time instances during a mode-I tensile test. (b): Fourier transform of the side-lobes of the FBG reflection spectra, and the shift of the highest frequency component towards lower frequencies as the delamination defect is progressing along the sensor length.

Fig. 8.8a shows the shift of the maximum harmonic frequency of the side-lobes of FBG reflection spectra, from the top layer of the composite. Finally, the progression of the delamination defect in different layers of the composite, along with the retrieved delamination length from camera images are depicted in Fig. 8.8b.

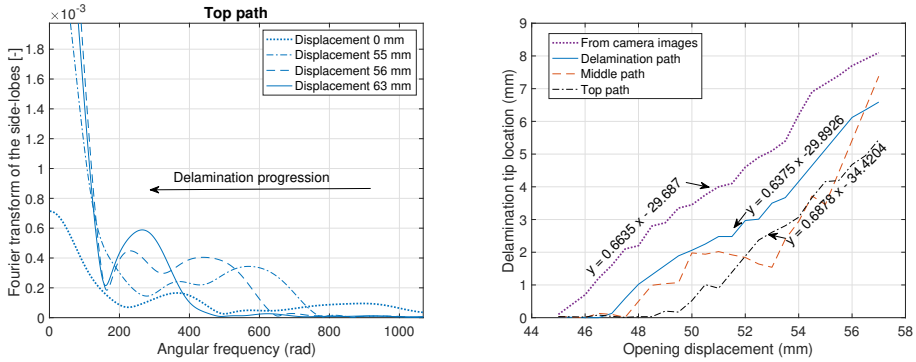

(a) (b)

Figure 8.8: (a): Fourier transform of the side-lobes of the FBG reflection spectra, surface mounted on the top layer of the specimen. (b): The progression of the delamination defect along the FBG length, as retrieved from the camera images, as well as FBG sensors at different layers of the composite. The linear regression fit to each line (except for the middle path) is also shown on this figure.

From Fig. 8.8b it is evident that there is a clear difference between the delamination length observed from the side of the specimen (retrieved from camera images), and that of the centre of the specimen retrieved from the FBG sensor. This difference reaches around 1.5 mm at some points, however, the trend of the delamination looks almost identical. The same holds for the retrieved delamination length from the top layer of the composite, except for the expected difference in the delamination tip estimation (around 1.5 mm in this example), as a result of out of plane measurement of the defect (discussed in Section 8.3). In fact, as seen from the linear regression results shown in Fig. 8.8b, the difference between the slope of the regression line from camera images, and those of the FBG sensors in the delamination path and on the top path, are less than 4 %.

Another point worth mentioning is the poor correlation of the delamination length retrieved from the FBG in the middle path, compared to the other paths. Our hypothesis is that this unreliability is the result of embedding the sensor between the 0 degree and the 90 degree layers of the composite, which results in significant unwanted transverse loads on the sensor, which in turn results in non-axial components in the strain field and birefringence effects on the reflection spectrum. This birefringence is not represented in our approximation of the reflection spectrum given in Eq. (8.1), and results in harmonic frequencies that might interfere with the outcome of our algorithm. Another factor that affects the results from the middle path, is the possible formation of barely visible cracks in the 90 degree layer of the composite, which are transverse to the length of the sensor. As discussed in Chapter 7, the formation of these micro-cracks along the length of the FBG results in several new harmonic frequencies in the Fourier transform of the side-lobes, whose frequencies will be scattered in the whole range of $\omega = 0$ rad to $\omega = 2M$ rad depending

on the location of the cracks along the FBG length. These new unwanted harmonics will also interfere with the results of our delamination tip estimation algorithm and can lead to unreliable measurements.

Furthermore, in the experiments of this study, it was assumed that the position of the FBG sensor along the FBG length is known with a sub-millimetre accuracy. This knowledge is important, as the precision of the delamination tip estimation algorithm directly depends on how accurate the FBG position is known. The position of the current commercial FBG sensors are marked by the manufacturing company on the optical fibre. However, the actual position of the sensor within these markings can deviate by more than 1 mm, which directly affects the precision of our delamination tip estimation algorithm. To solve this problem, the methods proposed in Chapters 5 and 6 can be used to determine the accurate length and position of the FBG sensor along the optical fibre with a micro-metre accuracy. That being said, in some applications such as studying the fatigue behaviour of composites, where the growth rate of the delamination is desired [23], such precise information about the sensor position is not needed, and the regression offset value in retrieving the precise crack tip does not affect the results either.

8.5. CONCLUSIONS

In this chapter, we presented the proof of concept for using FBG sensors as accurate delamination detection and delamination tip monitoring sensors in unidirectional laminated composite materials. We showed that the delamination defect along the FBG length will result in harmonic frequencies in the Fourier transform of its reflection spectrum, whose frequencies depend on the tip of the delamination. We also showed that as the delamination tip progresses along the length of an embedded FBG sensor, the frequency of these high amplitude harmonics will be shifted towards lower frequencies. The shift of the harmonic frequency was shown to linearly depend on the shift of the delamination tip as the defect was progressing along the sensor. Monitoring this frequency component, we could estimate the delamination tip with sub-millimetre accuracy, and provide useful information about the internal layers of the composite. We argued that the location of the delamination tip observed from the side of the specimen can greatly differ from its central parts, and using camera images alone might not be sufficient for providing full field information about the delamination plane. In particular, in the experiments of this chapter, for a 5 mm wide specimen, there was a difference of around 1.5 mm between the delamination tip retrieved from the side of the specimen and the delamination tip from the embedded FBG sensor in the centre of the specimen.

It can be concluded from this study that using multiple sensors in the delamination plane can provide us with a high resolution and quasi-distributed measurement of the delamination tip progression in composites, and the low computational complexity of our algorithm means that the signal processing can be performed in real-time.

REFERENCES

[1] V. Giurgiutiu, *Structural health monitoring of aerospace composites*. Academic Press, 2015.

[2] W. Staszewski, G. Tomlinson, C. Boller, and G. Tomlinson, *Health monitoring of aerospace structures*. Wiley Online Library, 2004.

[3] D. Nardi, M. Abouhamzeh, R. Leonard, and J. Sinke, "Detection and evaluation of pre-preg gaps and overlaps in glare laminates," *Applied Composite Materials*, vol. 25, no. 6, pp. 1491–1507, 2018.

[4] I. Pelivanov, Ł. Ambroziński, A. Khomenko, E. G. Koricho, G. L. Cloud, M. Haq, and M. O'Donnell, "High resolution imaging of impacted CFRP composites with a fiber-optic laser-ultrasound scanner," *Photoacoustics*, vol. 4, no. 2, pp. 55–64, 2016.

[5] J. Dong, A. Locquet, and D. Citrin, "Enhanced terahertz imaging of small forced delamination in woven glass fibre-reinforced composites with wavelet de-noising," *Journal of Infrared, Millimeter, and Terahertz Waves*, vol. 37, no. 3, pp. 289–301, 2016.

[6] A. Sobhani, M. Saeedifar, M. A. Najafabadi, M. Fotouhi, and D. Zarouchas, "The study of buckling and post-buckling behavior of laminated composites consisting multiple delaminations using acoustic emission," *Thin-Walled Structures*, vol. 127, pp. 145–156, 2018.

[7] R. Yang and Y. He, "Optically and non-optically excited thermography for composites: A review," *Infrared Physics & Technology*, vol. 75, pp. 26–50, 2016.

[8] A. Anisimov, B. Müller, J. Sinke, and R. Groves, "Analysis of thermal strains and stresses in heated fibre metal laminates," *Strain*, vol. 54, no. 2, p. e12260, 2018.

[9] S. Takeda, Y. Okabe, and N. Takeda, "Monitoring of delamination growth in CFRP laminates using chirped FBG sensors," *Journal of Intelligent Material Systems and Structures*, vol. 19, no. 4, pp. 437–444, 2008.

[10] S. Takeda, S. Minakuchi, Y. Okabe, and N. Takeda, "Delamination monitoring of laminated composites subjected to low-velocity impact using small-diameter FBG sensors," *Composites Part A: Applied Science and Manufacturing*, vol. 36, no. 7, pp. 903–908, 2005.

[11] H.-y. Ling, K.-t. Lau, L. Cheng, and W. Jin, "Utilization of embedded optical fibre sensors for delamination characterization in composite laminates using a static strain method," *Smart Materials and Structures*, vol. 14, no. 6, p. 1377, 2005.

[12] E. Farmand-Ashtiani, J. Cugnoni, and J. Botsis, "Monitoring and characterization of the interfacial fracture in sandwich composites with embedded multiplexed optical sensors," *Composite Structures*, vol. 96, pp. 476–483, 2013.

[13] L. Sorensen, J. Botsis, T. Gmür, and J. Cugnoni, "Delamination detection and characterisation of bridging tractions using long FBG optical sensors," *Composites Part A: Applied Science and Manufacturing*, vol. 38, no. 10, pp. 2087–2096, 2007.

[14] D. Sans, S. Stutz, J. Renart, J. Mayugo, and J. Botsis, "Crack tip identification with long FBG sensors in mixed-mode delamination," *Composite Structures*, vol. 94, no. 9, pp. 2879–2887, 2012.

[15] D. Höwer, B. A. Lerch, B. A. Bednarcyk, E. J. Pineda, S. Reese, and J.-W. Simon, "Cohesive zone modeling for mode I facesheet to core delamination of sandwich panels accounting for fiber bridging," *Composite Structures*, vol. 183, pp. 568–581, 2018.

[16] O. Al-Khudairi, H. Hadavinia, A. Waggott, E. Lewis, and C. Little, "Characterising mode I/mode II fatigue delamination growth in unidirectional fibre reinforced polymer laminates," *Materials & Design (1980-2015)*, vol. 66, pp. 93–102, 2015.

[17] P. Liu, R. M. Groves, and R. Benedictus, "3D monitoring of delamination growth in a wind turbine blade composite using optical coherence tomography," *NDT & E International*, vol. 64, pp. 52–58, 2014.

[18] D. Lee, J. Lee, and S. Yun, "The mechanical characteristics of smart composite structures with embedded optical fiber sensors," *Composite Structures*, vol. 32, no. 1-4, pp. 39–50, 1995.

[19] A. V. Oppenheim, *Discrete-time signal processing*. Pearson Education India, 1999.

[20] T. M. Hermann, J. E. Locke, and K. K. Wetzel, "Fabrication, testing, and analysis of anisotropic carbon/glass hybrid composites volume 1: Technical report," tech. rep., Citeseer, 2006.

[21] T. Erdogan, "Fiber grating spectra," *Journal of Lightwave Technology*, vol. 15, no. 8, pp. 1277–1294, 1997.

[22] G. Luyckx, E. Voet, W. De Waele, and J. Degrieck, "Multi-axial strain transfer from laminated CFRP composites to embedded Bragg sensor: I. parametric study," *Smart Materials and Structures*, vol. 19, no. 10, p. 105017, 2010.

[23] S. Rubiera, A. Argüelles, J. Viña, and C. Rocandio, "Study of the phenomenon of fatigue delamination in a carbon-epoxy composite under mixed mode I/II fracture employing an asymmetric specimen," *International Journal of Fatigue*, vol. 114, pp. 74–80, 2018.

9

CONCLUSION AND FUTURE WORK

As stupid and vicious as men are, this is a lovely day.

Kurt Vonnegut, Cat's Cradle

In this chapter a summary of the contributions in this thesis will be presented. Further, possible directions for future research and open problems in the field of structural health monitoring with FBG sensors, and possible approaches to solve these problems, will be discussed later in this chapter.

9.1. CONCLUSIONS

Measuring deformation and acquiring information about the damage state in the internal layers of composite materials is a challenging task. Conventional structural health monitoring techniques either do not provide high enough spatial resolution and are not suitable for accurate crack detection or accurate damage growth monitoring [1], or are not capable of inspecting the internal composite layers [2]. One the other hand, fibre Bragg grating (FBG) sensors are capable of being integrated within the layers of composites without severely altering their properties, and they offer several advantages such as high sensitivity to strain, capability of multiplexing, and their negligible sensitivity to electromagnetic interferences [3]. Considering these properties, this thesis was dedicated to develop new applications for FBG sensors for structural health monitoring of composite materials, and to improve the accuracy of the existing strain estimation and damage detection techniques in them. The contributions of this thesis are summarised in the following subsections where the research questions posed in the introduction chapter are answered as well. The diagram of Fig. 9.1 summarises the contributions of this thesis.

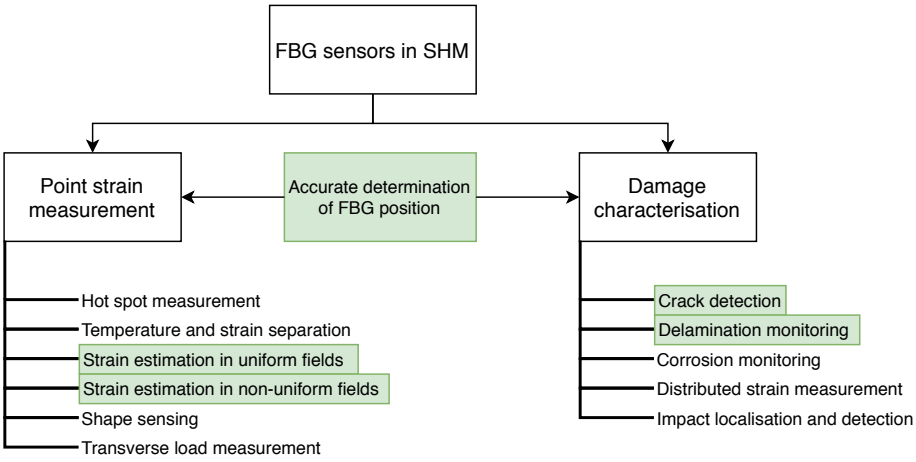

Figure 9.1: A summary of the contributions of this thesis. The added block of accurate FBG position determination enhances the precision of the other applications, both in point strain measurement and in damage characterisation.

9.1.1. AVERAGE STRAIN ESTIMATION

The first application investigated in this thesis was accurate point strain (or temperature) measurement using commercial FBG sensors. It was shown that the traditional peak tracking based strain estimation methods do not work well under non-uniform strain fields and can result in errors of several hundred micro-strains. Using a mathematical model presented in Chapter 3, two methods were proposed (Chapters 3 and 4) to calculate the average strain under such non-uniform axial strain fields without any prior knowledge about the scenario. Further, the performance of these methods was investigated under different types of FBG sensors and interrogation systems. Such accurate average strain estimation method is most interesting for long FBG sensors of more than one centimetre length, where it is more common to experience non-uniform strain fields along the sensor length. These algorithms were tested and validated using computer simulations and experimental measurements from FBG sensors mounted on aerospace structures undergoing different smoothly and sharply varying axial strain distributions. Therefore, the explicit answer to the first research question posed in Chapter 1 as

Q1: With only the magnitude of the FBG reflection spectra, is it possible to provide a meaningful measure of non-uniform strain fields?

is:

A1: If non-apodized FBG sensors are used, using the methods presented in Chapters 3 and 4, the average of any arbitrary axial non-uniform strain field along the sensor length can be accurately determined. In particular, the centre of mass of the FBG reflection spectrum was shown to analytically correspond to the average of the non-uniform axial strain field applied over the non-apodized FBG sensor length. In the case of using a partially apodized FBG sensor, or having a sensor that is affected

by non-axial strain components, the side-lobes cross-correlation maximisation algorithm of Chapter 3 can be used to compensate for the possible strain estimation errors resulted from the centroid method.

9.1.2. IMPROVING THE SPATIAL RESOLUTION OF FBG SENSORS

In Chapters 5 and 6, it was mentioned that for commercial FBG sensors their exact position in the optical fibre is not always provided with a high precision. This uncertainty on the exact length and the position of the sensor can be more than a millimetre and it directly affects the precision of damage detection algorithms as presented in this thesis. Chapters 5 and 6 were dedicated to resolving this problem, in which we proposed algorithms to determine the exact length of the FBG sensor as well as its precise position along the optical fibre. Incorporating this knowledge into the structural health monitoring scheme of an experimental setup with FBG sensors leads to an accurate and precise evaluation of the damage progression and formation in composite materials. Such insight can help making better and more meaningful comparisons between engineering models and experimental measurements. With that, the answer to the second research question of Chapter 1 posed as

Q2: Can we extract knowledge on the precise position of the FBG sensor?

is:

A2: Following a simple procedure presented in Chapters 5 and 6, and by analysing the reflection spectrum of a FBG sensor, it is possible to accurately determine its exact position along the optical fibre. The accurate length of the FBG sensor (independent of its type or the strain field it is subjected to) can be determined by simply retrieving the maximum oscillation frequency of the FBG reflection spectrum side-lobes, as this frequency was shown to be linearly dependent on the sensor length. To determine the exact position of the sensor a hardware setup was proposed in which two random points along the sensor length were thermally excited. Analysing the FBG reflection spectrum and retrieving the frequency of the added harmonics to its side-lobes, the exact starting and ending point of the sensor was calculated.

While it is certainly more convenient to carry out the procedures of Chapters 5 and 6 in the production site and to deliver the sensor with accurate markings to the user, the low complexity of the presented setups and the simple algorithms that follow the measurements can be implemented by the end user as well. In applications that such precise knowledge of the sensor location is necessary, such as in damage growth monitoring in composites, the presented methods in these chapters provide an alternative solution to acquire that information.

9.1.3. DAMAGE IDENTIFICATION AND CHARACTERISATION

Fibre optic sensors can provide information about damages in the internal layers of laminated composite materials. In Chapter 2, several studies focusing on damage detection and characterisation in composites were discussed and it was mentioned that the state-of-the-art fibre-optic based methods are either time-consuming and difficult to multiplex or have a poor spatial resolution. In this thesis, using the mathematical model presented in

Chapter 3 and incorporating the precise location of the sensor retrieved using the methods of Chapters 5 and 6, detection and identification of two major damage types in laminated composites were investigated, namely, matrix cracks and delamination. In Chapter 7 a method was proposed to identify the formation of these internal micro-cracks along the length of the FBG sensor. Chapter 8 was focused on accurate determination of the crack tip in mode-I delamination tests with sub-millimetre accuracy, and the performance of both these algorithms was tested and validated using computer simulations and experimental measurements from FBG sensors embedded between composite layers. Consequently, the final two research questions posed in Chapter 1 can be answered as follows.

Q3.1: Having access to only the magnitude of the FBG reflection spectra, is it possible to quantifiably characterise matrix cracks in composites?

Q3.2: Is it possible to monitor the delamination growth direction and extent in composites, accurately and dynamically?

A3.1: With the presented approximated transfer matrix model, and the algorithm proposed in Chapter 7, it is possible to reliably characterise transverse matrix cracks along the FBG length. In order to do so, the reflection spectra from embedded FBG sensors between composite materials that were affected by transverse cracks along their length were recorded. It was shown that the sharp strain shifts resulting from cracks along the FBG length result in the addition of new harmonic frequencies to the reflection spectra side-lobes. The frequency of these added harmonics linearly depends on the locations of the crack along the sensor length. Therefore, by analysing the FBG reflection spectrum, the formation of such cracks along the sensor length can be characterised.

A3.2: With the proposed method of Chapter 8 it is possible to monitor the delamination growth in mode-I tensile and fatigue tests with micrometer accuracy. The delamination crack tip will create a sharp strain shift along the embedded FBG length. This leads to a powerful harmonic frequency in the side-lobes of the sensor's reflection spectrum whose frequency linearly depends on the location of the crack tip. By tracking this frequency, the crack tip position and its growth rate can be monitored accurately. The low computational complexity of this method makes it suitable for dynamic measurements and the study of delamination propagation in composites under fatigue.

It should be noted that the area of sensitivity in such static damage detection applications is limited to the length of the sensor, and if the non-uniform strain field resulted from the damage does not reach the length of the FBG sensor it will not be detected. On the other hand, the length of these FBG sensors are limited to a few centimetres and embedding hundreds of these sensors within the composite material is not practical. This makes the application of these sensors for large scale damage identification in composites impractical and irrelevant. However, the unrivalled high spatial resolution and accuracy of the damage identification and detection algorithms proposed in this thesis and their low computational complexity makes them suitable for studying the dynamic behaviour of composite materials under different tensile and fatigue loads and mixed-mode damages.

9.2. FUTURE WORKS

This thesis presented new possibilities and applications in using FBG sensors in the field of structural health monitoring of engineering structures, and in particular, aerospace composite materials. In the course of this project several algorithms were developed for more accurate estimation of the damage state or strain values in aerospace materials and all these methods passed the proof of concept phase. However, the reliability and the sensitivity of these methods need to be studied under broader experimental conditions.

The first topic that can certainly be investigated in more detail is including non-axial strain components in the FBG model and devising damage detection algorithms that are more robust against transverse loads. Based on the discussions in Chapter 7, it is expected that a sensor that is not yet affected by transverse cracks along its length, will only have powerful harmonic frequencies at $\omega = 0$ and $\omega = \pm 2M$ in the Fourier transform of the side-lobes of its reflection spectrum, where M is the number of segments in the FBG model [4]. Therefore, having additional peaks in the Fourier domain before the formation of cracks could be misinterpreted as damage and can lead to false alarms in the outcome of these algorithms. Overall, the damage characterisation algorithms presented in Chapter 7 and 8 are to some extent robust against the typical residual transverse loads over the FBG length, but more intense loads could result in false alarms in their outputs. As an example, in an experiment with embedded FBG sensors in pre-impregnated composites, the composite specimens underwent the curing process in an autoclave at 7 bar pressure which created residual transverse loads on the FBG sensor. However, this process did not affect the outcomes of the crack detection algorithm presented in Chapter 7. This is shown in Fig. 9.2c, where the Fourier transform of the side-lobes of the reflection spectrum of Fig. 9.2a is shown. It can be seen that the residual transverse load has a small effect on the existing peaks in the Fourier domain. However, in the case of applying a uniform transverse load of 5 N on the FBG sensor (presented in Fig. 9.2b), the additional harmonics in the Fourier domain were powerful which is not desirable(see Fig. 9.2d).

Another example of possible directions for future research would be analysing the sensitivity of the presented crack detection method in Chapter 7 to different strain shift values in the strain distribution along the FBG length. In other words, determining the minimum amount of strain shift that can robustly be detected by our crack detection algorithm. Quantifying the sensitivity of our crack detection algorithm will have a direct effect on the sensitivity area of the FBG sensor itself. For instance, finite element modelling results suggest that when the crack location is not in direct contact with the sensor and the FBG is surface mounted or embedded on a different layer than the crack layer, the strain field experienced by the FBG will be smoother than that of the crack location. Whether a surface mounted FBG can still detect such anomalies in the structure, especially in thick composite materials, is a question that needs to be investigated. Along the same lines, the sensitivity of a surface mounted FBG sensor (around 2 millimetres away from the delamination plane) to delamination tip propagation in mode-I tensile tests was investigated in Chapter 8 and the results were promising.

Furthermore, there can be new designs for the grating distribution, or the apodisation pattern of the FBG sensor that can enhance its sensitivity to the formation of cracks. In Chapters 4 and 7, it was already mentioned that apodized FBG sensors did not perform as well as non-apodized FBG sensors. In particular, in Chapter 4 it was shown that apodized

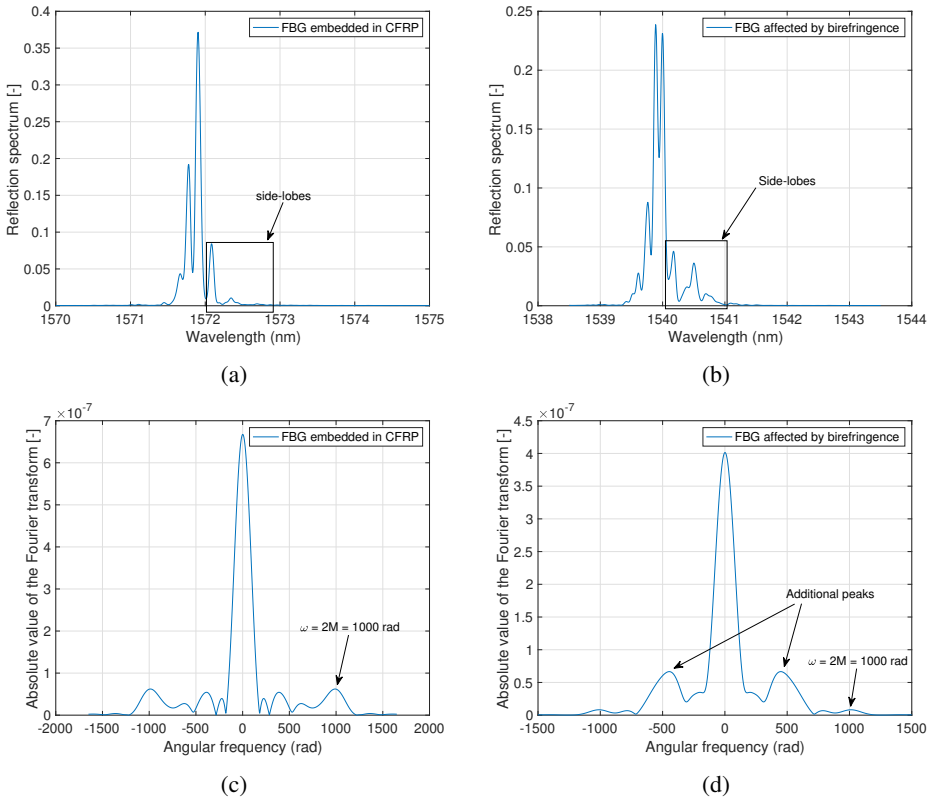

Figure 9.2: (a) Reflection spectrum of an FBG sensor embedded between carbon fibres and cured at 7 bars of pressure. (b) A bare FBG sensor under a uniform transverse load of 5 N along its length. (c) Fourier transform of the side-lobes of the reflection spectrum of Fig. 9.2a. (d) Fourier transform of the side-lobes of the reflection spectrum of Fig. 9.2b.

FBG sensors do not perform well for average strain estimation under non-uniform strain fields and can lead to considerable estimation errors. Moreover, considering FBG sensors of the same reflectivity levels, apodized FBG sensors are less sensitive to transverse cracks along their length. In Fig. 9.3 a comparison is made between the the reflection spectra of two FBG sensors (of the same reflectivity levels), one apodized and one non-apodized, affected by a transverse crack along their length (at similar positions). The lower sensitivity of the apodized FBG sensor is clear.

Another issue that can be inspected is optimising the window function applied on the FBG reflection spectrum in order to retrieve its side-lobes. In several of the chapters of this thesis, the first step of the presented algorithms was to retrieve the FBG reflection spectrum side-lobes. In these algorithms, a Hann window [5] of a fixed length of a few nano-metres was usually chosen. However, in some applications such as the delamination tip localisation method presented in Chapter 8, the choice of the size and the region of the side-lobes could result in biases (however small) in the output of the algorithm. An optimised design of this

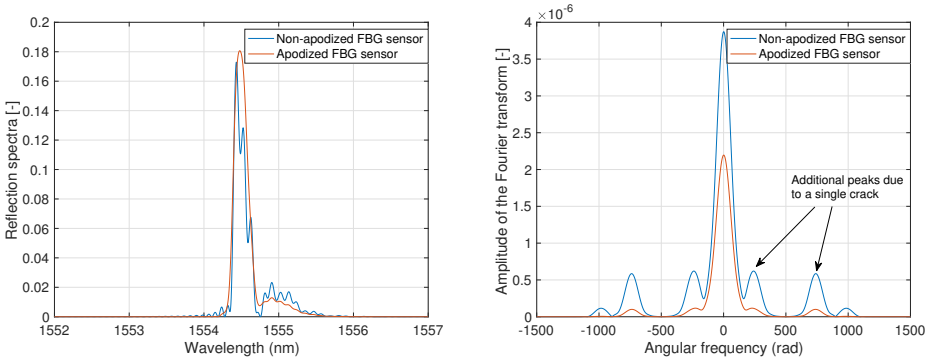

(a) (b)

Figure 9.3: (a) Reflection spectra of an apodized and a non-apodized FBG sensor affected by a transverse crack along their length at similar positions. (b) The Fourier transform of the side-lobes of the reflection spectra of Fig. 9.3a.

window function regarding its length, shape, and region of retrieval, can help overcoming these problems, and result in more reliable measurements.

The final issue that needs to be investigated is the embedding of the optical fibres in aerospace or civil engineering structures. Although this topic is beyond the scope of this thesis, it is a limiting factor for many fibre optic based structural health monitoring applications. In particular, embedded fibre optics between composite layers requires a manual but accurate lay up of the optical fibre in alignment with the reinforcement fibres of the composite, and the final product is delicate and fragile especially in the ingress and egress points of the optical fibre. A new design for the interface of the optical fibres and the host material, or a redesign of the optical sensing element material is needed to make these approaches more appealing for other researchers and engineers in the field of aerospace engineering or structural integrity.

9.3. CLOSING REMARKS

As final remarks, it should be mentioned that the methods developed in this thesis are not limited to aerospace engineering applications and can be well extended to any kind of engineering structure. In particular, the applications developed in this thesis regarding crack detection and damage progression can be easily modified and adapted to engineering structures such as carbon fibre and glass fibre laminated composites, concrete, and asphalt. This is an important extension of this work as owing to the durability of fibre optic sensors under harsh environmental conditions, and their remote sensing capabilities, they are becoming more and more attractive for civil engineering applications, and also more accessible [6–8].

REFERENCES

[1] T. Whitlow, E. Jones, and C. Przybyla, “In-situ damage monitoring of a SiC/SiC ceramic matrix composite using acoustic emission and digital image correlation,” *Com-*

posite Structures, vol. 158, pp. 245–251, 2016.

[2] M. Flores, D. Mollenhauer, V. Runatunga, T. Beberniss, D. Rapking, and M. Pankow, "High-speed 3D digital image correlation of low-velocity impacts on composite plates," *Composites Part B: Engineering*, vol. 131, pp. 153–164, 2017.

[3] A. D. Kersey, M. A. Davis, H. J. Patrick, M. LeBlanc, K. Koo, C. Askins, M. Putnam, and E. J. Friebele, "Fiber grating sensors," *Journal of Lightwave Technology*, vol. 15, no. 8, pp. 1442–1463, 1997.

[4] A. Rajabzadeh, R. Heusdens, R. C. Hendriks, and R. M. Groves, "Characterisation of transverse matrix cracks in composite materials using fibre Bragg grating sensors," *Journal of Lightwave Technology*, 2019.

[5] A. V. Oppenheim, *Discrete-time signal processing*. Pearson Education India, 1999.

[6] P. Kara De Maeijer, G. Luyckx, C. Vuye, E. Voet, S. Vanlanduit, J. Braspenninckx, N. Stevens, J. De Wolf, *et al.*, "Fiber optics sensors in asphalt pavement: State-of-the-art review," *Infrastructures*, vol. 4, no. 2, p. 36, 2019.

[7] X.-X. Li, W.-X. Ren, and K.-M. Bi, "Fbg force-testing ring for bridge cable force monitoring and temperature compensation," *Sensors and Actuators A: Physical*, vol. 223, pp. 105–113, 2015.

[8] J. Sierra-Pérez, M. A. Torres-Arredondo, and A. Güemes, "Damage and nonlinearities detection in wind turbine blades based on strain field pattern recognition. FBGs, OBR and strain gauges comparison," *Composite Structures*, vol. 135, pp. 156–166, 2016.

ACKNOWLEDGEMENTS

The past four years were a wonderful journey for both personal and professional development, and this thesis is only a byproduct of that. This development would not have been possible if it was not for the help and support of my colleagues, friends and family, and I would like to express my deepest gratitude to them. First, I would like to thank my advisors, Dr. Roger M. Groves, Dr. Richard C. Hendriks and Prof. Dr. Richard Heusdens. Your professional work ethics, your critical thinking, and your mentorship had a major influence on my work and on my worldview. You gave me the freedom to choose the direction of this project and supported me in my work, while at the same time pointing out my weaknesses and giving valuable remarks on the content of my work. It was a pleasurable experience to work in such a joint project, and I thank you for giving me the opportunity to be a part of it. Also, I would like to thank Prof. Alle-Jan van der Veen, the head of the CAS group, for always being there for everyone and for his supportive attitude, and also, Irma and Minaksie at CAS, and Gemma at SI&C for their support outside research.

Secondly, I would like to thank my colleagues and friends at the CAS group, the SI&C group and the AeroNDT laboratory. Working in a joint project between two different departments required me to gain a lot of knowledge about many different topics that were unfamiliar to me. Acquiring such knowledge would not have been possible without our discussions and your input in the group seminars. In particular, I would like to thank my officemates at CAS: Alberto, Andreas, Elvin, Jamal, Jiani, Jie, Pim, Tom, and Wangyang at the CAS group. I am happy I was part of such a lively office, and I enjoyed our discussions and activities together. Same goes to my officemates at SI&C: Agnes, Bram, Fabricio, Julian, Maria, Megan, Tian and Xi, for contributing to an office that was always filled with positive energy. Special thanks to Ilias Tapeinos for the fantastic collaboration that we had on his composite cryogenic tank experiment at DLR in Germany. It was a fun project, and a good opportunity to get some experience with fibre optic sensing at cryogenic temperatures. Further, thanks to the technician team of the DASML, in particular Berthil, Gertjan, Misja, Johan, Victor and Fred, for their support during the laboratory experiments and the mechanical tests. Also, I would like to thank all my current colleagues at Optics11 for contributing to such a healthy and fun working environment, and Aloys in particular for his help with the Dutch section of this thesis. I enjoy the adventures we go through and I look forward to our growth together.

Starting a new life abroad was an exciting adventure, but part of this experience is missing one's home country, culture, and the people. We were lucky to be surrounded by a fine group of Iranians, and to establish friendships that made this transition smooth. Mohsen, our coffee breaks and our talks were always refreshing, Mehrdad and Elahe, we arrived together in Delft and you were by our side in all the major events of our life here. Also, many thanks to Saleh, Samira, Mohsen, Negin, Nasim, Milad, Bahar, Sina, Jamal, Nima, Ghazaleh, Farnaz, Mahyar, Golshan, Ali and Hanie, for the wonderful memories we made together. Seyran and Nader, thanks for bringing our Pishan to us from Iran. Also,

thank you Hamed for designing the cover of this thesis and your patience during the process. And finally, many thanks to Mohsen Taheri, my dear friend of more than 20 years, for his support and presence during all the hardships and the good times.

I would like to thank my parents, Alireza and Mahnaz, and my sister and brother in law, Ayda and Morteza. I would not have been where I am now if it wasn't for your support and your sacrifices. Mom and dad, I am forever grateful for the hardships you went through and the difficult choices you had to make to bring us here. Lastly, I like to thank my wife Bahareh for always being by my side. You are my love and my best friend, and I am so lucky to share my life with you. I had the luxury of also being your colleague during our PhDs, and our tea and lunch breaks were the best recess a student can ask for! Thanks for your patience, your support, and the amazing memories we created together.

Aydin R. Zadeh
Delft, March 2020

A

APPENDICES

A.1. PROOF OF LEMMA 1

1. By definition, we have

$$\bar{\alpha} = \frac{1}{M}\sum_{i=1}^{M}\alpha_i = 2\pi n_{\text{eff}}\Delta z\,\frac{1}{M}\sum_{i=1}^{M}\frac{1}{\lambda_{B_i}} = 2\pi n_{\text{eff}}\Delta z\,\frac{1}{M}\sum_{i=1}^{M}\frac{1}{\bar{\lambda}_B+\Delta_i}.$$

Taylor series expansion of the terms in the summation yields

$$\frac{1}{\bar{\lambda}_B+\Delta_i} = \frac{1}{\bar{\lambda}_B\left(1+\frac{\Delta_i}{\bar{\lambda}_B}\right)} = \frac{1}{\bar{\lambda}_B}\left(1-\frac{\Delta_i}{\bar{\lambda}_B}+\mathcal{O}\left(\left(\frac{\Delta_i}{\bar{\lambda}_B}\right)^2\right)\right),$$

so that

$$\bar{\alpha} = \frac{2\pi n_{\text{eff}}\Delta z}{\bar{\lambda}_B}+\mathcal{O}\left(\frac{\overline{\Delta^2}}{\bar{\lambda}_B^3}\right),$$

since

$$\frac{1}{M}\sum_{i=1}^{M}\Delta_i = \frac{1}{M}\sum_{i=1}^{M}(\lambda_{B_i}-\bar{\lambda}_B) = 0.$$

2. Let $k\in\{1,M\}$. We have

$$\frac{\xi_i-\xi_{i+1}}{\xi_k} = \frac{(\alpha-\alpha_i)^{-1}-(\alpha-\alpha_{i+1})^{-1}}{(\alpha-\alpha_k)^{-1}},$$

for $i=1,\ldots,M-1$. Since

$$(\alpha-\alpha_i)^{-1} = \frac{\lambda\lambda_i}{\lambda_i-\lambda},$$

we conclude that

$$\frac{\xi_i-\xi_{i+1}}{\xi_k} = \frac{(\lambda_k-\lambda)\lambda}{\lambda_k(\lambda_i-\lambda)(\lambda_{i+1}-\lambda)}(\lambda_{i+1}-\lambda_i).$$

Let $\Delta_{\max} = \max_i |\Delta_i|$ and let $|\lambda - \bar{\lambda}_B| = \Delta\lambda > \lambda_{\text{th}}$ so that $\Delta\lambda - \Delta_{\max} < |\lambda_i - \lambda| < \Delta\lambda + \Delta_{\max}$ for $i = 1, \ldots, M$. With this, we have

$$\left| \frac{\xi_i - \xi_{i+1}}{\xi_k} \right| \leq \frac{\Delta\lambda + \Delta_{\max}}{(\Delta\lambda - \Delta_{\max})^2} \frac{\bar{\lambda}_B + \Delta\lambda}{\bar{\lambda}_B - \Delta_{\max}} |\lambda_{i+1} - \lambda_i|,$$

so that $|\xi_i - \xi_{i+1}| \ll |\xi_k|$ if

$$|\lambda_{i+1} - \lambda_i| \ll \frac{(\Delta\lambda - \Delta_{\max})^2}{\Delta\lambda + \Delta_{\max}} \frac{\bar{\lambda}_B - \Delta_{\max}}{\bar{\lambda}_B + \Delta\lambda} < \Delta\lambda.$$

Since λ_{th} is the infimum of $\Delta\lambda$, the condition $|\lambda_{i+1} - \lambda_i| \ll \lambda_{\text{th}}$ is a sufficient condition for $|\xi_i - \xi_{i+1}| \ll |\xi_k|$. This completes the proof.

A.2. PROOF OF LEMMA 2

Rewriting (4.12) leads to

$$I=\int_{-\infty}^{+\infty}\frac{(x-\theta_1+\theta_1-\theta_c)\sin(x-\theta_1)\sin(x-\theta_2)\cos(nx-\theta_3)}{(x-\theta_1)(x-\theta_2)}\mathrm{d}x,\ x\neq\theta_1,\theta_2. \tag{A.1}$$

In the above equation, for $x=\theta_1$ and $x=\theta_2$ we have $\sin(x-\theta_1)/(x-\theta_1)=1$ and $\sin(x-\theta_2)/(x-\theta_2)=1$, respectively. Multiplying the first term in the nominator with the rest of the terms leads to

$$\begin{aligned}I=&\int_{-\infty}^{+\infty}\frac{\sin(x-\theta_1)\sin(x-\theta_2)\cos(nx-\theta_3)}{(x-\theta_2)}\\&+\frac{(\theta_1-\theta_c)\sin(x-\theta_1)\sin(x-\theta_2)\cos(nx-\theta_3)}{(x-\theta_1)(x-\theta_2)}\mathrm{d}x.\end{aligned} \tag{A.2}$$

Considering the fact that

$$\frac{1}{(x-\theta_1)(x-\theta_2)}=\frac{1}{\theta_1-\theta_2}\Big(\frac{1}{x-\theta_1}-\frac{1}{x-\theta_2}\Big), \tag{A.3}$$

I can be further simplified to

$$I=I_2+\frac{\theta_1-\theta_c}{\theta_1-\theta_2}I_1-\frac{\theta_1-\theta_c}{\theta_1-\theta_2}I_2, \tag{A.4}$$

where

$$\begin{aligned}I_k=&\int_{-\infty}^{+\infty}\frac{1}{x-\theta_k}\Big\{\cos(\theta_1-\theta_2)\cos(nx-\theta_3)\\&-\frac{1}{2}\Big(\cos((n-2)x+\theta_1+\theta_2-\theta_3)+\cos((n+2)x-\theta_1-\theta_2-\theta_3)\Big)\Big\}\mathrm{d}x, k=\{1,2\}.\end{aligned} \tag{A.5}$$

In the above equation, the I_k's are obtained by using the product to sum trigonometric identities. Now we can apply the integration over the I_k terms, where the integration is applied over each individual term in I_k. Here, we only present the integration procedure for the first term of I_k, as the rest of the integration procedure is performed in the exactly the same manner.

$$\begin{aligned}&\int_{-\infty}^{+\infty}\frac{1}{x-\theta_k}\big(\cos(\theta_1-\theta_2)\cos(nx-\theta_3)\big)\mathrm{d}x\\&=n(\cos(\theta_1-\theta_2))\int_{-\infty}^{+\infty}\frac{\cos(nx-n\theta_k+n\theta_k-\theta_3)}{n(x-\theta_k)}\mathrm{d}x\\&=n(\cos(\theta_1-\theta_2))\Big\{\int_{-\infty}^{+\infty}\frac{\cos(nx-n\theta_k)(\cos(n\theta_k-\theta_3))}{n(x-\theta_k)}\mathrm{d}x\\&-\int_{-\infty}^{+\infty}\frac{\sin(nx-n\theta_k)(\sin(n\theta_k-\theta_3))}{n(x-\theta_k)}\mathrm{d}x\Big\}=\pi\cos(\theta_1-\theta_2)\sin(\theta_3-n\theta_k).\end{aligned} \tag{A.6}$$

The last result is due to the fact that $\int_{-\infty}^{\infty}\frac{\cos(nx)}{nx}\mathrm{d}x=0$ and $\int_{-\infty}^{\infty}\frac{\sin(nx)}{nx}\mathrm{d}x=\frac{\pi}{n}$. Following the same procedure, and considering the boundaries of the integrals, the I_k terms can be

calculated as

$$
\begin{aligned}
I_1 &= \frac{\pi}{2}(\sin(\theta_3+\theta_2-(n+1)\theta_1)-2\cos(\theta_2-\theta_1)\sin(\theta_3-n\theta_1)\\
&+\sin(\theta_3-\theta_2-(n-1)\theta_1))=0\,,\\
I_2 &= \frac{\pi}{2}(\sin(\theta_3-(n+1)\theta_2+\theta_1)-2\cos(\theta_2-\theta_1)\sin(\theta_3-n\theta_2)\\
&+\sin(\theta_3-(n-1)\theta_2-\theta_1))=0\,.
\end{aligned}
\tag{A.7}
$$

The above results are achieved by using product to sum trigonometric identities (on the second term of I_1 and I_2), and therefore, $I=0$.

BIOGRAPHY

Aydin Rajabzadeh was born in Tehran, Iran, on March 27th 1989. He obtained his B.Sc. in electrical engineering in 2011, and his M.Sc. in biomedical engineering in 2015, both from University of Tehran. From 2010 till 2015, he was working as electronics engineer at the aerospace research institute of Iran, developing biological sensing units and signal acquisition and transmission modules. These modules were used in the first sub-orbital space mission in Iran, where a live subject was successfully launched into space and recovered (the Pishgam explorer launched in 2013). He then worked as a telecommunication engineer at RighTel Communications from 2015 till early 2016. He started as a PhD student in Technische Universiteit Delft in February 2016, working in a joint project between the Circuits and Systems group of the EEMCS faculty, and the Aerospace NDT Laboratory of the Aerospace Engineering faculty. In his project, he focused on developing new structural health monitoring solutions for fibre-optic based sensors, with applications in strain estimation and damage detection in aerospace composite materials. He was the recipient of the best student paper award at the SPIE Photonics Europe conference in Strasbourg in 2018. In his free time, Aydin likes to read books about history and philosophy and occasional novels, bake bread and experiment with different recipes, and he likes to travel. He is currently working as a fibre sensing development engineer in Optics11 in Amsterdam.